On Complex Spin Textures, Majorana Modes, and Machida-Shibata States - Exploring Nano-Scale Systems with Tight-Binding Models

Dissertation

zur Erlangung des Doktorgrades
an der Fakultät für Mathematik, Informatik und Naturwissenschaften
im Fachbereich Physik
der Universität Hamburg

vorgelegt von

Jannis Neuhaus-Steinmetz

Hamburg

2025

Gutachter/innen der Dissertation:

Prof. Dr. R. Wiesendanger

PD Dr. E. Y. Vedmedenko

Zusammensetzung der Prüfungskommission:

Prof. Dr. D. Pfannkuche

Prof. Dr. R. Wiesendanger

PD Dr. E. Y. Vedmedenko

Prof. Dr. M. Potthoff

Prof. Dr. L. Mathey

Vorsitzende/r der Prüfungskommission:

Prof. Dr. D. Pfannkuche

Datum der Disputation:

23.09.2025

Vorsitzender des Fach-Promotionsausschusses PHYSIK:

Prof. Dr. Wolfgang J. Parak

Leiter des Fachbereichs PHYSIK:

Prof. Dr. Markus Drescher

Dekan der Fakultät MIN:

Prof. Dr.-Ing. Norbert Ritter

Abstract

The search for Majorana zero modes has been a major undertaking in the field of solid state physics in recent years, as they have potentially promising applications in fault-tolerant quantum computing. On the theory side, tight-binding models combining magnetism, Rashba spin-orbit coupling, and superconductivity have been on the forefront of this quest. They feature all ingredients necessary for experimental realization of Majorana zero modes.

In this thesis, we take such a model, adapt and apply it to vastly different problems and geometries, while leaving its core intact. We explore its magnetic ground state in one and two dimensions, showing a surprisingly rich magnetic phase space. By self-consistently calculating the magnetic ground states before identifying electronic topological phases, we demonstrate in one dimension that, for a significant portion of the phase space, spin-spirals and topologically non-trivial states naturally coexist. We develop a computationally highly efficient approach to find the magnetic ground states of tight-binding models with a fitted classical spin model that is not inherently limited by assumptions, like RKKY being limited to weak magnetic couplings, and also grants additional insight into the driving magnetic forces of the system. With this method, we completely characterize the magnetic parameter space of our two-dimensional tight-binding model, showing that also 2D systems feature a rich magnetic phase diagram with many exotic magnetic phases despite the simplicity of the model at first glance. As the amount of data points is quite large and the magnetic phases are too complex to be classified by a simple algorithm, we employ an artificial neural network to classify the magnetic phases, thereby demonstrating that artificial neural networks can be a useful tool for the classification of magnetic ground states.

Additionally, we provide theoretical support for the first experimental measurement of simultaneous zero-bias-peaks at both ends of an atomic chain, which marks a milestone in the search for Majoranas. In the experiment, an atomic

Mn chain was constructed on Nb(110) in the $[1\bar{1}0]$-direction to build hybridizing Yu-Shiba-Rusinov states in a bottom-up approach. To model this, we adapt our tight-binding model to three dimensions. Replicating the experimental geometry, we are able to predict the chain length at which the found zero-modes are expected to evolve into isolated Majorana zero modes and demonstrate the crucial role of the strength of Rashba spin-orbit coupling.
Finally, we provide a geometrically correct model for experiments on quantum dots caged by a box of Ag adatoms on a Ag island on superconducting Nb. With these experiments, the existence of energetically sharp non-magnetic in-gap states has been shown for the first time. This confirms theoretical predictions of Machida and Shibata on spin-degenerate Andreev bound states from 1972.

Zusammenfassung

Die Suche nach Majorana-Nullmoden ist seit Jahren eine der großen Unternehmungen der Festkörperphysik, da sie potenziell vielversprechende Anwendungen in fehlertoleranten Quantencomputern besitzen. Auf der Theorieseite kommen Tight-Binding-Modelle mit Magnetismus, Rashba-Spin-Bahn-Kopplung und s-Wellen-Supraleitung vielfach zum Einsatz, da sie alle Zutaten beinhalten, die für die experimentelle Realisierung von Majorana-Nullmoden notwendig sind.

In dieser Arbeit betrachten wir ein solches Modell und adaptieren es für die Anwendung auf eine Vielzahl von Problemen und Geometrien, während wir seinen Kern unverändert lassen. Wir untersuchen die magnetischen Grundzustände dieses Modells in ein und zwei Dimensionen und entdecken einen überraschend vielseitigen magnetischen Phasenraum. In einer Dimension zeigen wir durch magnetisch selbstkonsistente Rechnungen, dass in einem großen Anteil des Parameterraums Spinspiralen und elektrisch nicht-triviale Zustände natürlich koexistieren. Wir entwickeln eine rechnerisch hocheffiziente Methode zur Ermittlung der magnetischen Grundzustände von Tight-Binding-Modellen durch angenäherte klassische Spin-Modelle, die nicht inherent durch Annahmen limitiert sind. Beispielsweise ist das Tight-Binding-Modell im Gegensatz zu der verbreiteten RKKY-Methode nicht auf schwache magnetische Austauschterme limitiert. Darüber hinaus bietet unsere Methode durch das genäherte klassische Modell zusätzliche Einsichten in die magnetischen Kräfte innerhalb des Systems. Mit dieser Methode charakterisieren wir die magnetischen Grundzustände im vollständigen Parameterraum unseres 2D-Modells und entdecken auch hier einen Reichtum an exotischen magnetischen Phasen trotz der scheinbaren Simplizität des zugrundeliegenden Tight-Binding-Modells. Aufgrund der großen Menge an Datenpunkten und der Komplexität der magnetischen Phasen, nutzen wir ein künstliches neuronales Netzwerk zur Unterstützung bei der Klassifizierung der magnetischen Phasen. Damit demonstrieren wir die

Nützlichkeit von künstlichen neuronalen Netzwerken als Werkzeug zur Sortierung von magnetischen Grundzuständen.
Darüber hinaus liefern wir unterstützende Rechnungen zu der ersten experimentellen Messung simultaner Nullmoden an beiden Enden einer atomaren Kette, einen Meilenstein auf der Suche nach Majoranas. In dem Experiment wurde eine atomare Mn-Kette auf Nb(110) in der $[1\bar{1}0]$-Richtung konstruiert, um hybridisierende Yu-Shiba-Rusinov-Zustände hervorzurufen. Um dies zu modellieren, erweitern wir unser Modell auf drei Dimensionen. Mit unserem Modell sind wir in der Lage vorherzusagen, ab welcher Kettenlänge sich die Nullmoden zu gut isolierten Majorana-Nullmoden entwickeln, und zeigen darüber hinaus, wie essentiell die Rashba-Spin-Bahn-Kopplung dabei ist.
Abschließend präsentieren wir ein geometrisch korrektes Modell von Experimenten zu Zuständen innerhalb einer Ag-Box auf einer Ag-Insel auf supraleitendem Nb. Durch diese Experimente wurden erstmalig energetisch scharfe, nicht-magnetische Zustände innerhalb einer supraleitenden Lücke gezeigt, wodurch die theoretischen Vorhersagen von Machida und Shibata von 1972 zu spin-entarteten Andreev-Bound-States bestätigt wurden.

Contents

Disclaimer on Previous Publications

As most of the results of my thesis are already published in scientific articles, large parts of this thesis closely follow my previous peer-reviewed publications. Therefore, parts of this thesis are identical to parts of the following articles:

Jannis Neuhaus-Steinmetz, Elena Y. Vedmedenko, Thore Posske, and Roland Wiesendanger

Complex magnetic ground states and topological electronic phases of atomic spin chains on superconductors [1]

Phys. Rev. B **105**, 165415 – Published 13 April, 2022

Jannis Neuhaus-Steinmetz, Tim Matthies, Elena Y. Vedmedenko, Thore Posske, and Roland Wiesendanger

Large diversity of magnetic phases in two-dimensional magnets with spin-orbit coupling and superconductivity [2]

Phys. Rev. B **110**, 155427 – Published 15 October, 2024

Lucas Schneider, Philip Beck, Jannis Neuhaus-Steinmetz, Levente Rózsa, Thore Posske, Jens Wiebe, and Roland Wiesendanger

Precursors of Majorana modes and their length-dependent energy oscillations probed at both ends of atomic Shiba chains [3]

Nature Nanotechnology **17**, pages 384-389 - Published 07 March 2022

Lucas Schneider, Khai Thât-Tôn, Ioannis Ioannidis, Jannis Neuhaus-Steinmetz, Thore Posske, Roland Wiesendanger, and Jens Wiebe

Proximity superconductivity in atom-by-atom crafted quantum dots [4]

Nature **621**, pages 60–65 - Published 16 August 2023

Acronyms

AFM: Anti-Ferromagnet
ANN: Artificial Neural Network
ARPES: Angular Resolved Photoemission Spectroscopy
BdG: Bogoliubov-de Gennes
DFT: Discrete Fourier Transform
DMI: Dzyaloshinskii–Moriya Interaction
DOS: Density of States
FM: Ferromagnet
LDOS: Local Density of States
MCS: Monte-Carlo Step
MM: Majorana Mode
MSS: Machida-Shibata states
PMM: Precursors of Majorana Modes
QD: Quantum Dot
RKKY: Ruderman–Kittel–Kasuya–Yosida
RSO: Rashba Spin-Orbit
SC: Superconductor / Superconducting
STM: Scanning-Tunneling-Microscopy
STS: Scanning-Tunneling-Spectroscopy
TB: Tight-Binding
t-SNE: t-distributed Stochastic Neighbor Embedding
YSR states: Yu-Shiba-Rusinov states

Chapter 1

Introduction

Majorana zero modes occurring in topological superconductors have potential applications in fault-tolerant quantum computing, since they are largely immune to local perturbations because of their topological protection [5–7]. Theoretical models that contain s-wave superconductivity, magnetism and Rashba spin-orbit coupling find wide use, as those are considered to be the main ingredients to make the experimental realization of Majorana zero modes possible [8–10]. In this thesis, we focus on a minimalist tight-binding model that contains all three of these. While the core of the model remains unchanged, we apply it to vastly different geometries and a variety of questions. Going from pure one-dimensional models over two-dimensional systems to three dimensional replications of experimental setups, we demonstrate the versatility of the model.

One-dimensional systems in proximity to s-wave superconductors have recently been extensively investigated as candidates for topological superconductivity [5, 11, 12]. This includes experiments and calculations on semiconducting nanowires in magnetic fields [9, 10, 13–15], self-organized atomic chains [16], and atomically constructed magnetic chains on superconducting substrates [17–20], e.g., Fe on Re [17, 18] and Mn on Nb [19]. These systems are furthermore promising platforms for odd-frequency and triplet superconductivity [21–23]. A central model for analyzing the electronic and magnetic properties of the above-mentioned systems is the spinful one-band model with proximity-induced s-wave superconductivity, including local magnetic Zeeman fields and Rashba spin-orbit coupling [8, 9, 24–28]. This model describes 1D systems that can exhibit topological superconductivity and host Majorana zero modes at their ends. Despite its simplicity, there is an ongoing discussion about the magnetic

ground state of such systems in dependence on its parameters. Klinovaja et al. [24] and Vazifeh et al. [25] found via an effective spin model that the system self-organizes into a topological state in the limit of weak magnetic interactions. Hu et al. [27] assumed harmonic spin spirals and identified the energetically most favorable ones among them. In contrast to this approach, Minami et al. [28] performed Monte-Carlo simulations with an effective spin model at vanishingly small temperature and additionally found ground state spin configurations in non-superconducting systems that are not represented by harmonic spirals, but either by collinear or by non-coplanar configurations. Furthermore, there are models including electron-electron interactions and continuum electron models to predict the magnetic phases in one-dimensional superconductors with magnetic impurities and Rashba spin-orbit coupling, which point towards a stable, self-organized spiral magnetic phase giving rise to one-dimensional topological superconductivity [29–32].

In Chapter 4, we present Monte-Carlo calculations of the magnetic ground state of one-dimensional magnetic chains with proximity-induced s-wave superconductivity. On each atomic site, our model contains quasi-classical spins whose interactions are mediated by itinerant electrons, which is an approximation for atoms with large total spin (e.g, 7/2). We show that non-spiral non-collinear phases exist, and analyze how they are affected by superconductivity and how they affect the topological electronic phases of the system in return. For weak and vanishing superconductivity, we identify magnetic phases of complex order as well as complex collinear phases in addition to previously known harmonic spirals and collinear phases. Our calculations are first performed in a tight-binding model, where we consider the magnetization as a free parameter and do not limit it by any assumption about the magnetic ground state. Secondly, we introduce a computationally efficient method for approximately determining the magnetic ground states of large tight-binding systems, which we use to gain an understanding of the driving forces behind the complex magnetic states. To this end, we fit the parameters of a classical Heisenberg spin model to our tight-binding model, showing that four-spin interactions become relevant to reproduce the magnetic phases. Our new approximative method is categorically faster with agreeable deviations, which inspires us to move to

larger systems and investigate the magnetism of two-dimensional interfaces.

There is a plethora of magnetic phases in the physics of interfaces. Alongside ferromagnetic and anti-ferromagnetic spin orientations in the ground state, recently non-collinear phases including spirals, multi-q states [33–35], canted AFMs [36], bubbles, and topological magnetism including skyrmions [37] and merons [38], as well as further exotic phases like altermagnets [39] have been theoretically and experimentally discovered. Magnetic phases form a cornerstone of today's and future storage technology [40–42] and are fundamentally interesting because of exotic classical and quantum quasiparticle excitations that could be hosted in frustrated or correlated magnets [43, 44]. For modeling purposes and for detecting yet novel magnetic phases, the question arises which conceptionally simple models host a large number of magnetic phases that can be tuned by experimentally accessible parameters. Particularly interesting in this regard are systems that combine magnetism and superconductivity, where the competition between both effects creates a rich phenomenology. While numerous studies of one-dimensional magnetic systems in proximity to s-wave superconductors exist, motivated by the interest in Majorana physics [1, 3, 45, 46], the data on phase diagrams of their two-dimensional counterparts have been very limited up to now [47, 48]. Ground state studies on quantum and classical magnetic moments coupled to itinerant electrons found evidence of chiral order [49], topological electronic order [50, 51], and multi-spin interactions [52] in frustrated triangular lattices without superconductivity. Motivated by the results on superconducting 1D systems and the new method presented in Chapter 4, we therefore consider a two-dimensional square lattice tight-binding model with local magnetic moments, Rashba spin-orbit coupling, and superconductivity. Our model is effectively describing localized classical magnetic moments that are coupled by the itinerant electrons of a surface state, not specifically bound to a parameter regime. The knowledge of possible ground states in those complex structures is required for several reasons. First, exotic topological states have been found in 2D itinerant magnets in proximity to a superconductor (SC) [47, 48]. Second, interesting multi-spin interactions can be present in such systems [33, 53] that might lead to unexpected magnetic and

electronic phases. Due to big datasets in the study of magnetic systems, machine learning has been applied extensively in this field, which we make use of as well. In particular, corresponding techniques have been employed to predict the parameters of the magnetic Hamiltonian [54], to retrieve the topological charge from dynamic chiral magnetic structures [55], and to construct phase diagrams for skyrmionic systems [56, 57]. Additionally, unsupervised learning has found a variety of applications in the field of microscopic magnetism [58–60] and the identification of topological phases [61, 62].

In Chapter 5, we analyze the ground states of magnetic moments coupled by a spinful tight-binding model with proximity-induced s-wave superconductivity, local magnetic Zeeman moments and Rashba spin-orbit coupling (RSO). The resulting approximately 20,000 magnetic configurations are too diverse to be reliably classified by a simple algorithm. We therefore use contrastive learning [63, 64], a recent unsupervised machine learning technique, which can be adapted to the physical symmetries. While contrastive learning was used to classify phases in the Ising, Compass, and Su-Schrieffer-Heeger models [65] using the scheme of Ref. [63], we used Contrastive Clustering [66] to obtain the phases directly from the network. Our results show that this technique is highly effective for the classification of complex phase spaces of magnetic systems on SC.

In this thesis, we also present theoretical calculations that have been done to support experimental findings, which is the focus of the Chapters 6 and 7. There are many theoretical proposals to combine superconductivity, magnetism and Rashba spin-orbit coupling in effective 1D systems in proximity to an s-wave superconductor to create experimentally realizable platforms that host Majorana zero modes [8–10, 30, 67–69]. Examples for experimental systems containing these features are semiconducting nanowires with proximity-induced superconductivity in an external magnetic field [13, 14], and magnetic adatom chains with ferromagnetic [16, 45, 70, 71] or spin-spiral orientation [17, 18] on superconducting substrates. Majorana zero modes (MMs) are immune to perturbations that are local compared to the system size, due to their topological protection stemming from the non-trivial bulk band structure. Many atomic

chains studied before only consist of tens of atoms, though [16–18]. At these lengths, MMs on the ends of the chain may still interact, which results in the zero-bias-peaks splitting away from zero energy in an oscillatory manner. This is considered one of the key signatures of precursors of MMs (PMMs) in short chains [72–74]. Previous experiments, using Coulomb blockade spectroscopy on InAs nanowires coupled to Al, found an oscillatory energy splitting as a function of the magnetic field, that was reduced in long wires, but could not continuously vary the length of the wire [72]. In InSb nanowires coupled to NbTiN, zero-bias-peaks have been observed, but could only be detected on one end, while the signature on the other end was different [75]. Zero-bias peaks at the ends of atomic spin chains have also been observed in various experiments [16, 45, 70, 71], but they all came with a few caveats. They were not detected on both ends of a defect-free chain simultaneously, and only some chains contained zero-bias-peaks, while other chains in the same systems did not show any zero-bias-peaks. Additionally, the chain length could also not be varied continuously in these experiments.

In Chapter 6, we present the measurements and calculations of energy oscillations of PMMs in Mn chains on Nb(110) along the chain, including both ends, as a function of chain length, which is continuously varied atom by atom. The experiments done with STM and STS techniques have been performed by Lucas Schneider and Philip Beck. From the extensive experimental dataset, we are able to adjust all the parameters of a three-dimensional tight-binding model. Through this model, we deepen our understanding of the experimental system and are able to predict a critical chain length, above which the PMMs evolve to isolated topologically well protected Majorana zero modes. Additionally, we discuss the effect of the dimensionality on the localization, and how much the critical chain length is affected by the precise value of the Rashba coupling constant.

Many interesting states of matter are created from inducing superconductivity by proximity in otherwise non-superconducting materials [76, 77]. In these heterostructures, superconductivity needs to be scattered into the surface states [30, 78, 79], but the surface states are typically well decoupled from

the bulk bands. This is why it is often unclear whether enough superconducting pairing is acquired if there are more than a few nanometers between the surface and the superconducting substrate [78–80]. To study this effect, the problem is downscaled as much as possible by investigating only a single resonance mode of the surface state, which is laterally confined in a quantum corral, forming a so-called quantum dot (QD). This can occur in naturally formed nano-scale islands [81, 82] or in tunable artificially constructed adatom arrays [83, 84], where the walls are built atom by atom using an STM tip. Typically, surface states are well decoupled from the bulk states, but scattering at step edges and adatoms is known to introduce a measurable coupling between bulk and surface state [85, 86]. Coupled QDs with tunable interactions are used as a platform to simulate quantum materials [87, 88], but ways to induce superconductivity in their eigenmodes have not been studied before.

In Chapter 7, we present experimental and theoretical results on artificial QDs that have been designed by constructing a box of Ag adatoms on a Ag(111) island on superconducting Nb(110), using atom manipulation to continuously vary the size of the box. The experiments were performed by Lucas Schneider and Khai Thât-Tôn, using STM and STS techniques. Showing non-magnetic in-gap surface states, the measurements provide experimental proof for a 50 years old theoretical prediction for spin-degenerate Andreev bound states made by Machida and Shibata [89]. In contrast to the more widely studied semiconductor or molecular QDs [90], the metallic QDs investigated here feature electron screening orders of magnitudes larger, thereby suppressing electron-electron interactions. This allows us to describe the system with a three-dimensional tight-binding model, in which we replicate the experimental results, using the actual geometry of the experiment.

Before we discuss our scientific results, we begin with an introduction to the theoretical concepts that this thesis is built upon in Chapter 2. Then, we continue with the models and methods used in this thesis in Chapter 3. Thereafter, we present our results in the Chapters 4, 5, 6, and 7. We summarize our results and present an outlook on future research in Chapter 8.

Chapter 2

Theory

In this chapter, we introduce the fundamental theories and physical principles that this thesis builds upon. We begin by introducing the Bloch theorem in Sec. 2.1, the tight-binding model in Sec. 2.2, and the classical Heisenberg model for spins in Sec. 2.3. Then, we introduce a few physical phenomena important for this thesis, namely skyrmions in Sec. 2.4, superconductors in Sec. 2.5, and Rashba spin-orbit coupling in Sec. 2.6. Thereafter, we discuss the concept of topology and how to apply it to physics in Sec. 2.7. Following up on that, we introduce Majorana zero modes and the Kitaev chain in Sec. 2.8.1. Lastly, we discuss how to adapt the Kitaev chain to a model with experimentally achievable conditions in Sec. 2.8.2.

2.1 Bloch Theorem

The Bloch theorem [91] is one of the most fundamental theorems of solid state physics. Essentially, it is the idea that a large lattice system can be described in terms of small periodic unit cells.

Consider a lattice potential $U(\vec{r})$ with

$$U(\vec{r}) = U(\vec{r} + \vec{R}) \tag{2.1}$$

for all Bravais lattice vectors $\vec{R}$. Lowercase $\vec{r}$ can denote any point in space. We keep this notation throughout the theory section of this thesis. When we neglect electron-electron interaction, a single-particle Hamiltonian is sufficient to describe the system. Therefore, the wavefunctions of the many electron

system can be described by the product state of single-electron wavefunctions. Consider the stationary Schrödinger equation

$$H\Psi(\vec{r}) = E\Psi(\vec{r}), \tag{2.2}$$

with the Hamiltonian

$$H = \left(\frac{-\hbar^2 \nabla^2}{2m} + U(\vec{r}) \right), \tag{2.3}$$

where $U(\vec{r})$ is the lattice periodic potential introduced in Eq. (2.1). We also consider a translation operator $T_{\vec{R}}$ that acts on a function $f(\vec{r})$ as

$$T_{\vec{R}} f(\vec{r}) = f(\vec{r} + \vec{R}). \tag{2.4}$$

Two translation operators combine

$$T_{\vec{R}} T_{\vec{R}'} = T_{\vec{R}+\vec{R}'} \quad \text{and} \quad T_{\vec{R}} T_{-\vec{R}} = T_0 = \mathbb{1}, \tag{2.5}$$

and translation operators commute with themselves

$$[T_{\vec{R}}, T_{\vec{R}'}] = 0. \tag{2.6}$$

If the system is translationally symmetric under Bravais lattice vectors $\vec{R}$, then and only then the Hamiltonian commutes with the translation operator

$$[H, T_{\vec{R}}] = 0. \tag{2.7}$$

Thus, we can choose simultaneous eigenvectors

$$H\Psi(\vec{r}) = E\Psi(\vec{r}) \quad \text{and} \quad T_{\vec{R}}\Psi(\vec{r}) = c(\vec{R})\Psi(\vec{r}). \tag{2.8}$$

From Eq. (2.5), it follows that

$$c(\vec{R} + \vec{R}') = c(\vec{R})c(\vec{R}') \quad \text{and} \quad c(\vec{R})c(-\vec{R}) = 1. \tag{2.9}$$

As the wavefunctions $\Psi(\vec{r})$ are normalized, $c(\vec{R})$ must be normalized, too.

$$1 = \int d^D\vec{r}\,|\Psi(\vec{r}+\vec{R})|^2 = \int d^D\vec{r}|T_{\vec{R}}\Psi(\vec{r})|^2 = \int d^D\vec{r}|c(\vec{R})|^2|\Psi(\vec{r})|^2 = |c(\vec{R})|^2 \tag{2.10}$$

for D dimensions. From Eq. (2.9) and (2.10) we can conclude that we can write $c(\vec{R})$ as

$$c(\vec{R}) = e^{\mathrm{i}\vec{k}\vec{R}} \tag{2.11}$$

with some wavevector $\vec{k}$.
We can now formulate the Bloch Theorem: Given that the translation vector $\vec{R}$ leaves the overall system invariant, the eigenfunctions of H have the form

$$\Psi(\vec{r}) = \frac{1}{\sqrt{N}} e^{\mathrm{i}\vec{k}\vec{r}} u_{\vec{k}}(\vec{r}) \tag{2.12}$$

with the normalization $\frac{1}{\sqrt{N}}$ and the lattice-periodic Bloch factor

$$u_{\vec{k}}(\vec{r}) = u_{\vec{k}}(\vec{r}+\vec{R}). \tag{2.13}$$

With the Bloch theorem, we can describe the whole system by infinitely repeating a single unit cell.

Band Structures

Assume a general stationary Schrödinger equation

$$\begin{aligned} E(\vec{k})\Psi_{\vec{k}}(\vec{r}) &= H\Psi_{\vec{k}}(\vec{r}) \\ &= \left(\frac{-\hbar^2\nabla^2}{2m} + U(\vec{r})\right)\Psi_{\vec{k}}(\vec{r}) \\ &= \left(\frac{-\hbar^2\nabla^2}{2m} + U(\vec{r})\right)\frac{1}{\sqrt{N}}e^{\mathrm{i}\vec{k}\vec{r}}u_{\vec{k}}(\vec{r}) \\ &= \frac{1}{\sqrt{N}}e^{\mathrm{i}\vec{k}\vec{r}}\left(\frac{-\hbar^2}{2m}(\nabla+\mathrm{i}\vec{k})^2 + U(\vec{r})\right)u_{\vec{k}}(\vec{r}) \\ &= \frac{1}{\sqrt{N}}e^{\mathrm{i}\vec{k}\vec{r}}\tilde{h}(\vec{k})u_{\vec{k}}(\vec{r}), \end{aligned} \tag{2.14}$$

with

$$\tilde{h}(\vec{k}) := \left(\frac{-\hbar^2}{2m} (\nabla + \mathrm{i}\vec{k})^2 + U(\vec{r}) \right). \tag{2.15}$$

For fixed $\vec{k}$, this gives us a new differential equation

$$\tilde{h}(\vec{k}) u_{\vec{k}}(\vec{r}) = E(\vec{k}) u_{\vec{k}}(\vec{r}). \tag{2.16}$$

The solutions $u_{n,\vec{k}}(\vec{r})$ indexed by n and their respective eigenvalues $E_n(\vec{k})$ are lattice periodic. For the reciprocal vector $\vec{k}$ only N discrete values are allowed, where N is the size of the system. For large systems, the values of $\vec{k}$ are so fine that they can be assumed to be continuous. From the periodicity of the wavefunctions and their eigenvalues, it follows that $\vec{k}$ can be restricted to the first Brillouin zone in reciprocal space. The eigenvalues $E_n(\vec{k})$ as continuous functions of $\vec{k}$ form so-called *energy bands* through the first Brillouin zone. The set of these bands is called the *band structure* and the Fermi energy E_F denotes the energy up to which these bands are occupied. A common convention is to set the Fermi energy as the zero energy level of the system, $E_\mathrm{F} = 0$.

2.2 Tight-Binding Model

The tight-binding model, originally introduced by Slater and Koster in 1954 [92], is a model for electron behavior in solid state systems, that is based on the idea that a solid state system can be described by atomic orbitals and the interactions between them.
First, we introduce Wannier functions $\omega_n(\vec{r}, \vec{R})$ [93], which are superpositions of Bloch functions $\Psi_{n,\vec{k}}(\vec{r})$

$$\omega_n(\vec{r}, \vec{R}) := \frac{1}{\sqrt{N}} \sum_{\vec{k} \in 1.\mathrm{BZ}} e^{-\mathrm{i}\vec{k}\vec{R}} \Psi_{n,\vec{k}}(\vec{r}) = \sum_{\vec{k} \in 1.\mathrm{BZ}} e^{\mathrm{i}\vec{k}\cdot(\vec{r}-\vec{R})} u_{n,\vec{k}}(\vec{r}). \tag{2.17}$$

The Wannier functions form an orthonormal basis and can be closely localized around the atomic sites $\vec{R}$ by tuning the phase of the Bloch states. The

Hamiltonian in a basis of Wannier functions reads

$$H_\omega = \sum_{n,\vec{R},\vec{R}'} |n,\vec{R}'\rangle \langle n,\vec{R}'| H |n,\vec{R}\rangle \langle n,\vec{R}| \quad \text{with} \quad \omega_n(\vec{r},\vec{R}) = |n,\vec{R}\rangle , \tag{2.18}$$

where the sum over $\vec{R}$ indicates summation over all atomic site positions. We now make the approximation that $\langle \vec{R}'| H |\vec{R}\rangle$ is negligible for distances greater than the nearest neighbors. Additionally, we define $\langle \vec{R}'| H |\vec{R}\rangle =: t_{\vec{R}\vec{R}'}$ for $\vec{R} \neq \vec{R}'$ and $\langle \vec{R}| H |\vec{R}\rangle = \mu_{\vec{R}}$. With this, we can write the tight-binding Hamiltonian

$$H_{\text{tb}} = \sum_{n,\vec{R}} |n,\vec{R}\rangle \, \mu_{\vec{R}} \, \langle n,\vec{R}| + \sum_{n,\vec{R},\vec{\delta}} |n,\vec{R}\rangle \, t_{\vec{R},\vec{R}+\vec{\delta}} \, \langle n,\vec{R}+\vec{\delta}| \tag{2.19}$$

with the vector $\vec{\delta}$ pointing to nearest neighbors. The hopping t describes the energy associated with the tunneling of an electron between two lattice sites. The chemical potential μ is the energy required to bring an electron into a lattice site. Generally, longer distance hoppings can be included in a tight-binding model but we restrict ourselves to nearest neighbor hopping here, since the models used in this thesis do not consider hopping over longer distances.

So far, we derived the tight-binding model. Let us now focus on why it is useful. In the tight-binding model, electrons are assumed to occupy discrete lattice sites or orbitals located at the sites. We can write the complete wavefunction as a weighted sum of the wavefunctions $|a\rangle$ that, respectively, describe an electron to be in orbital a

$$|\Psi\rangle = \sum_a \psi_a |a\rangle \tag{2.20}$$

with the wavefunction coefficients ψ_a. This allows us to write the Hamiltonian as

$$H = \sum_{ab} H_{ab} |a\rangle \langle b| , \tag{2.21}$$

where H_{ab} are the components of a matrix that describes how the electrons in orbitals a and b are coupled. This approach turns the stationary Schrödinger

equation into a matrix eigenvalue problem from linear algebra. We can construct a system by only considering how each orbital should be coupled to each other orbital and how much energy is required to place an electron in each orbital. Then, the Schrödinger equation can be solved, finding its eigenvalues and eigenvectors, with known algebraic methods by diagonalizing a matrix with the components H_{ab} .

2.2.1 Tight-Binding Model in Second Quantization

Throughout this thesis, we will mostly use the language of second quantization. Because of this, here, we derive the tight-binding model again, but in second quantization. This section loosely follows Ref. [94]. In second quantization the Hamiltonian is written in terms of creation operators $c_i^\dagger$ and annihilation operators c_i, which create and annihilate an electron in state i.
In first quantization, a generic Hamiltonian can be written

$$H = \sum_i T(\vec{x}_i) + \frac{1}{2}\sum_{i\neq j} V(\vec{x}_i, \vec{x}_j), \tag{2.22}$$

where $T \equiv T(\vec{x}_i)$ is the kinetic energy of the i-th particle at position $\vec{x}_i$ and $V \equiv V(\vec{x}_i, \vec{x}_j)$ is the potential energy of the interaction between the i-th and j-th particle at positions $\vec{x}_i$ and $\vec{x}_j$. We can rewrite the Hamiltonian in second quantization

$$H = \sum_{ij} c_i^\dagger \langle i| T |j\rangle c_j + \frac{1}{2}\sum_{ijkl} c_i^\dagger c_j^\dagger \langle ij| V |kl\rangle c_k c_l, \tag{2.23}$$

where the states i and j form a complete basis of the Hilbert space. We now make the approximation of neglecting electron-electron interactions, which simplifies the Hamiltonian to

$$H = \sum_{ij} t_{ij} c_i^\dagger c_j \quad \text{with the hopping term} \quad t_{ij} = \langle i| T |j\rangle . \tag{2.24}$$

With the additional approximation that any hopping longer than nearest neighbor hopping can be neglected

$$t_{ij} = \begin{cases} \mu_i & \text{for } i = j \\ t_{ij} & \text{for nearest neighbors} \\ 0 & \text{else,} \end{cases} \tag{2.25}$$

we write the tight-binding Hamiltonian in second quantization as

$$H_{\text{tb}} = \sum_i \mu_i c_i^\dagger c_i + \sum_{\langle i,j \rangle} t_{ij} c_i^\dagger c_j, \tag{2.26}$$

where $\langle i, j \rangle$ denotes that the sum is running over all combinations of nearest neighbors.

2.2.2 Common Notations and Useful Tricks

To conclude this section, we discuss some common notations and calculation tricks used in this thesis. The tight-binding Hamiltonians shown so far focused on systems with only one orbital per site, but we can also construct tight-binding Hamiltonians for systems with multiple orbitals per site. For this, we use creation and annihilation operators $c_{i,a}^\dagger$, $c_{i,a}$ with an additional index a, that create/annihilate particles in orbital a at site i. In this notation, it is often useful to define a basis such as $\vec{c}_i = (c_{i,1}, c_{i,2,}, ...)^T$. It should be noted here that some annihilation operators in the basis can also be replaced by creation operators to consider holes. For example, the basis most commonly used throughout this thesis is $\vec{c}_i = (c_{i,\uparrow}, c_{i,\downarrow}, c_{i,\downarrow}, -c_{i,\uparrow})$. Using such a basis, we can write a generic tight-binding Hamiltonian as

$$H = \sum_n^N \vec{c}_n^\dagger \tilde{h}_{\text{onsite}} \vec{c}_n + \sum_n^{N-1} \left[\vec{c}_n^\dagger \tilde{h}_{\text{hop}} \vec{c}_{n+1} + \text{h.c.} \right], \tag{2.27}$$

where $\tilde{h}_{\text{onsite}}$ is a matrix that denotes the potential energy of an electron on a given site and $\tilde{h}_{\text{hop}}$ couples orbitals of different sites. In one dimension, when the Hamiltonian is written in this notation, we can construct the k-dependent

Hamiltonian of the corresponding bulk system by writing

$$H(k) = \vec{c}_k^{\,\dagger} \left(\tilde{h}_{\text{onsite}} + \tilde{h}_{\text{hop}} e^{-\mathrm{i}k} + \tilde{h}_{\text{hop}}^{\dagger} e^{\mathrm{i}k} \right) \vec{c}_k \;\; =: \;\; \vec{c}_k^{\,\dagger} \tilde{h}(k) \vec{c}_k, \tag{2.28}$$

where the operators create/annihilate electrons with wavevector k. The bands can then be computed by calculating the k-dependent eigenvalues of the matrix $\tilde{h}(k)$.
The matrices $\tilde{h}_{\text{onsite}}$, $\tilde{h}_{\text{hop}}$ and $\tilde{h}(k)$ are also commonly written in terms of sums and Kronecker products of Pauli matrices.

2.3 Classical Spin Models

In 1928, Werner Heisenberg introduced the Heisenberg model to describe ferromagnetism [95]. Over three decades later, in 1964, Fischer introduced an approximation of the Heisenberg model for infinite spin, which uses three-dimensional vectors instead of operators to describe spins [96]. This approximation became known later as the classical Heisenberg model. Seven years later, in 1971, the first rigorous proof that this approximation is indeed correct in the limit of infinitely large spins, was provided by Millard and Leff [97]. In the classical Heisenberg model, spins $\vec{S}_i$ are written as three-dimensional real vectors living on each atomic site. The spins are coupled by an exchange interaction J.

$$H_{\text{Heisenberg}} = -\sum_{\langle i,j \rangle} J \vec{S}_i \cdot \vec{S}_j, \tag{2.29}$$

where $\langle i, j \rangle$ indicates that the summation runs over all pairs of nearest neighbors. The exchange interaction prefers parallel or antiparallel alignment of spins, depending on the sign of J.
This model can be expanded to include more complex interactions and also more neighbors. Throughout this thesis, we use $\langle i, j \rangle_n$ to indicate that the summation runs up to the n-th nearest neighbor. When only nearest neighbors are considered, we write $\langle i, j \rangle \equiv \langle i, j \rangle_1$. One such additional interaction is the Dzyaloshinskii–Moriya interaction (DMI), also known as anti-symmetric exchange [98]. It has the form $\vec{D}_{ij} \cdot (\vec{S}_i \times \vec{S}_j)$ and favors canted spins, where,

at interfaces, $\vec{D}_{ij}$ has the form $\vec{D}_{ij} = \vec{r}_{ij} \times \vec{\mathcal{D}}$ with a material dependent vector $\vec{\mathcal{D}}$ and the connecting positional vector $\vec{r}_{ij}$, resulting in $\vec{D}_{ij} = -\vec{D}_{ji}$. DMI typically occurs on surfaces due to symmetry breaking and is the driving force behind skyrmions [99]. With both interactions, exchange and DMI, up to the n-th neighbor the classical spin model becomes

$$H_{\text{classical}} = \sum_{\langle i,j \rangle_n} -J_n \vec{S}_i \cdot \vec{S}_j + \vec{D}_{ij} \cdot (\vec{S}_i \times \vec{S}_j). \tag{2.30}$$

We can generalize this model, allowing anisotropic exchange interactions, by writing all interaction terms into a 3×3-matrix $\bar{J}_n$

$$H_{\text{classical}} = \sum_{\langle i,j \rangle_n} \vec{S}_i^{\,T} \bar{J}_{ij} \vec{S}_j. \tag{2.31}$$

2.4 Skyrmions

Skyrmions are non-collinear, localized, particle-like spin textures that are topologically protected. The key interaction behind the formation of skyrmions is the Dzyaloshinskii-Moriya Interaction (DMI), which originates from spin-orbit coupling at surfaces. In 1962, T. H. R. Skyrme created a model in high-energy physics that describes baryons as topological solitons, thereby establishing the concept of a topological charge that is conserved regardless of the symmetries of the Hamiltonian [100]. In 1989, A. N. Bogdanov et al. first linked this concept to condensed matter physics [99]. They theoretically predicted that DMI can stabilize skyrmions in chiral magnetic materials. Later, Rößler et al. expanded on this by predicting stable skyrmion lattices as possible ground states in systems with DMI [101]. In 2009, the first experimental confirmation of a skyrmion lattice was provided by Mühlbauer et al. in MnSi [102], while individual skyrmions were first observed and locally manipulated in 2013 by Romming et al. [37]. Fig. 2.1 shows an example structure of a Néel type (a) and a Bloch type (b) skyrmion. In Néel type skyrmions, the spin rotation is always radial [34], while in Bloch type skyrmions, the spin rotation is perpendicular [102].

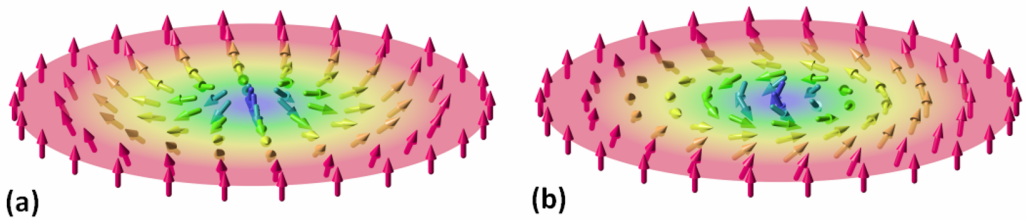

Figure 2.1: **Visualization of a skyrmion** of **(a)** Néel type and **(b)** Bloch type. This illustration was created by Karin Everschor-Sitte and Matthias Sitte, licensed under CC BY-SA 3.0 [103]. The figure has been rearranged.

Skyrmions can be identified by calculating their topological invariant, the skyrmion number [34]

$$N_{\mathrm{sk}} = \frac{1}{4\pi} \int \vec{M} \cdot \left(\frac{\partial \vec{M}}{\partial x} \times \frac{\partial \vec{M}}{\partial y} \right), \tag{2.32}$$

with the unit vector of the local magnetization $\vec{M}$. The skyrmion number is an integer-valued topological invariant that denotes the number of skyrmions in a system.
One of the most promising usages of skyrmions is the miniaturization of magnetic storage devices. Current storage devices need hundreds of thousands of atoms per bit, whereas nano-scale skyrmions only consists of a few hundred atoms. Due to their topological protection, skyrmions can be stable despite their small size, presenting a possible use as extremely small bits.

2.5 Superconductors

Superconductors are materials that exhibit zero electronic resistance when they are below a critical temperature T_{c}. Additionally, they expel magnetic flux lines when below this temperature. Superconductivity was first experimentally discovered in mercury in 1911 by Heike Kamerlingh Onnes, for which he received the Nobel Prize in 1913 [104]. The first microscopic explanation of superconductivity was provided by Bardeen, Cooper and Schrieffer in 1957 [105]. Their theory became famous under the name *BCS theory*, and they received the

Nobel Prize in 1972 [106]. Further major theoretical contributions to the understanding of superconductivity have been made by Abrikosov, Ginzburg and Leggett, for which they received the Nobel Prize in 2003 [107]. Interestingly, although being the first discovered superconductor, the first correct theoretical prediction of mercury's critical temperature and full theoretical explanation of its superconductivity has only recently been provided in 2022 [108], using superconducting density functional theory.

2.5.1 BCS Theory

The fundamental idea behind the BCS theory [105] is, that pairs of electrons form so-called Cooper pairs, which are bosonic quasiparticles. As bosons are not affected by the fermionic exclusion principle, they can form a collective quantum mechanical ground state, leading to perfect conductance. According to the BCS theory, an arbitrarily weak attractive interaction between electrons near the Fermi surface is sufficient for the formation of Cooper pairs. In conventional superconductors, this attractive interaction is mediated by phonons between electrons of opposite spins and momenta $\pm\vec{k}$. The attractive interaction causes the fermionic ground state to become instable and favor the formation of Cooper pairs for energies close to the Fermi level E_F. As the electrons close to E_F become Cooper pairs, a gap in the electronic density of states from $-\Delta$ to $+\Delta$ (for $E_\mathrm{F} = 0$) occurs, where Δ is the minimal energy needed to break a Cooper pair. Additionally, at $\pm\Delta$, so-called coherence peaks with a very large density of states occur. These peaks stem from a singularity in the density of states that gets smeared out in realistic systems due to the finite lifetime of Cooper pairs, as they are quasi-particles. An example of the density of states (DOS) of a superconductor is shown in Fig. 2.2.

2.5.2 Conventional and Unconventional Superconductivity

In conventional superconductors, the pairing is mediated by phonons and follows an s-wave symmetry, giving them the name *s-wave superconductors*. Elec-

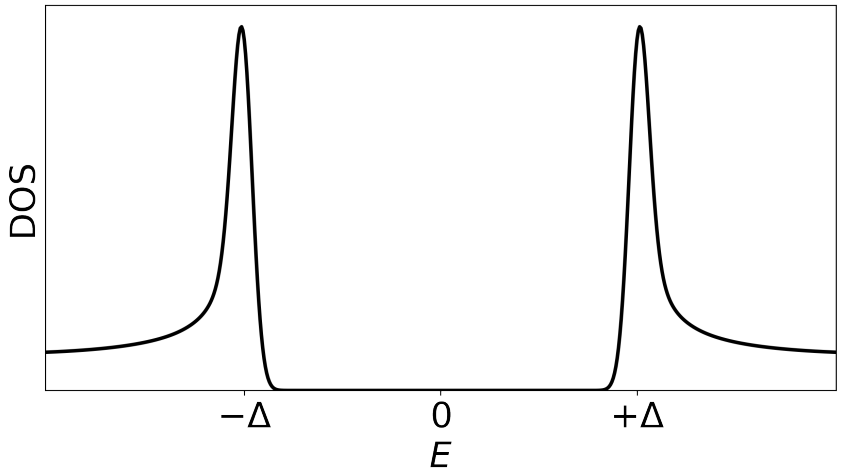

Figure 2.2: **Example of the density of states of a superconductor** as a function of energy.

trons of opposite spins and momenta form Cooper pairs, leading to spin singlet states with $S = 0$ and orbital momenta of the Cooper pairs of $L = 0$.
But there are also more exotic mechanisms leading to superconductivity, where Cooper pairs are in a spin-triplet $S = 1$ state with identical spin and non-zero angular momenta $L \neq 0$, like in p-wave and d-wave superconductors, with the names stemming from the symmetry classification of the superconducting gap. Here, we focus on p-wave superconductors, as they can exhibit topologically non-trivial phases. They are rare in nature, but indications for intrinsic p-wave superconductivity have been found in Sr_2RuO_4 [109], UTe_2 [110], NdFeAs(O,F) [111], and $AuSn_4$ [112]. Additionally, structures with magnetic materials on top of conventional superconductors can exhibit unconventional superconductivity with spin-triplet pairing [8], as the combination of s-wave superconductivity and spin-orbit coupling can generate effective p-wave pairing. The latter mechanism lays the groundwork for large parts of this thesis, and is discussed in more detail in Sec. 2.8.2.

2.5.3 Proximity-Induced Superconductivity

The proximity effect, also known as Holm-Meissner effect [113], describes the effect that when a superconducting (SC) material is brought into close contact with a non-superconducting material, superconductivity gets induced into the non-superconducting material over small distances and the critical temperature of the system gets reduced. The microscopic origin of the proximity effect lies in the Andreev Reflection [114, 115]. Depending on the combination of materials, the thickness of both the SC and the non-SC material, and the amount of impurities, the size of the induced superconducting gap can be highly variable. In later chapters of this thesis, we discuss systems of thin layers and atomic chains with proximity-induced superconductivity.

2.5.4 YSR States

Large magnetic fields usually suppress conventional s-wave superconductivity. But what happens when the magnetic perturbation is minimal, like in the smallest possible case of a single magnetic impurity atom in proximity to a superconductor? This question has been answered independently in the late 1960s by Yu, Shiba and Rusinov [116–118]. When placing a single magnetic impurity in proximity to an s-wave superconductor, a pair of additional sub-gap solutions with energies $|E| < |\Delta|$ emerges. These states are called Yu-Shiba-Rusinov (YSR) states or Shiba states. Both names are common in the literature, but here, we will refer to them as YSR states. They are caused by a local breaking of Cooper pairs, as the exchange with the magnetic impurity lowers the energy required to break a Cooper pair to less than Δ. YSR states are particle-hole symmetric and appear in pairs at energies $\pm E_{\mathrm{YSR}}$ around $E_{\mathrm{F}} = 0$. When the magnetic coupling to the impurity is weak, the YSR state's energies $\pm E_{\mathrm{YSR}}$ merge with the coherence peaks, as weak magnetic coupling only has a minimal effect on the breaking of Cooper pairs. For increasing coupling strength, E_{YSR} shifts towards E_{F} until the energies of the particle-hole symmetric pair cross. YSR states are expected to be spin-polarized [119, 120], which has also been shown experimentally [121, 122]. They are bound states

localized around the impurity with an extent on the scale of the superconductor's coherence length. In realistic systems, the magnetic impurity atom can have multiple spin-polarized orbitals which can contribute, each producing a pair of YSR states, potentially at different energies.

2.6 Rashba Spin-Orbit Coupling

Rashba spin-orbit (RSO) coupling is created by the breaking of mirror symmetry through the xy-plane at a surface, i.e., by the fact that there is a bulk in one z-direction and a vacuum or gas in the opposite direction at the surface. It owes its name to the influential paper of Rashba and Sheka [123] where they showed that under certain symmetry conditions a relativistic Hamiltonian contains energy terms that are linear in momentum. This linear coupling between the spin and the momentum is the central feature of RSO coupling and causes a momentum dependent splitting of spin bands.
Traditionally, RSO coupling is derived as follows. At the surface, the inversion symmetry in the z-direction is broken. From the electric fields of the nuclei, this symmetry breaking introduces an electric field E_z in z-direction.

$$H_E = -E_z \cdot e \cdot z, \tag{2.33}$$

with the electron charge $-e$. Given that an electron is moving with momentum $\vec{k}$, relativistic corrections let the electron experience a magnetic field $\vec{B}$.

$$\vec{B} = -(\vec{k} \times \vec{E})/(mc^2) \tag{2.34}$$

This magnetic field couples to the spin of the electron

$$H_{\mathrm{RSO}} = \frac{g\mu_B}{2mc^2}(\vec{k} \times \vec{E}) \cdot \vec{\sigma} \tag{2.35}$$

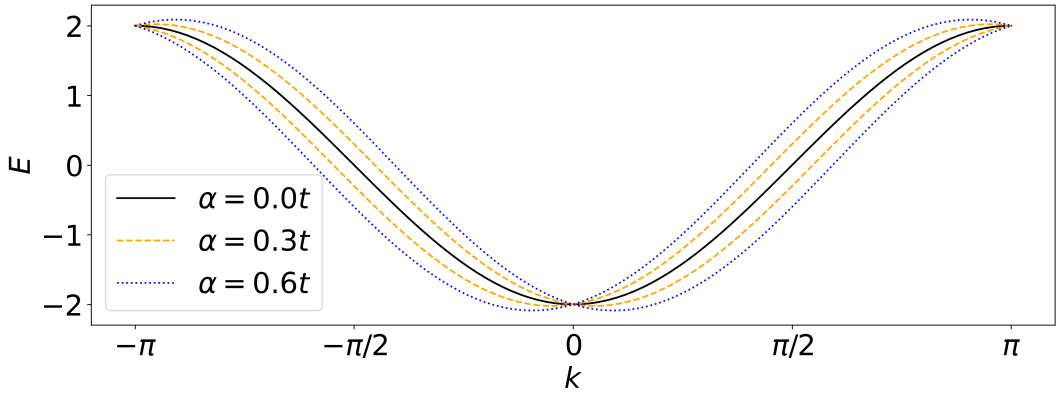

Figure 2.3: **Effect of Rashba spin-orbit coupling on the band structure.** Band structure from the eigenvalues calculated in Eq. (2.39) for $\alpha = 0.0\,t,\ 0.3\,t,\ 0.6\,t$.

with the magnetic moment $\frac{g\mu_B}{2}$ and the vector of Pauli matrices $\vec{\sigma}$. Knowing the direction of the E-field, we can write the RSO Hamiltonian as

$$H_{\mathrm{RSO}} = -\alpha(\vec{e}_z \times \vec{k}) \cdot \vec{\sigma} \text{ with } \alpha = \frac{g\mu_B E_z}{2mc^2}, \tag{2.36}$$

with the unit vector $\vec{e}_z$ in z-direction and the Rashba constant α, which is a material parameter. Qualitatively, this approach yields a good description of RSO coupling and has been confirmed in experiments on Ag(111) and Au(111) with angular resolved photoemission spectroscopy (ARPES), where the predicted spin splitting and the expected spin structure of the surface states have been observed [124, 125]. Quantitatively though, this approach provides values for α which are orders of magnitude too low. A detailed discussion on the microscopic origin of RSO coupling can be found in the review article [126], for example.

Example of RSO coupling in Tight-Binding

To gain a better understanding of RSO coupling, let us discuss an example of the effect of RSO on the band structure. Consider a tight-binding Hamiltonian

with nearest neighbor hopping and RSO coupling

$$H = \sum_i (\vec{c}_i^{\,\dagger}(-t\sigma_0 + \frac{\mathrm{i}}{2}\alpha\sigma_y)\vec{c}_i + \text{h.c.}), \tag{2.37}$$

with $\vec{c}_i = (c_{i,\uparrow}, c_{i,\downarrow})^T$, the hopping parameter t, RSO coupling constant α, and the Pauli matrices σ_m ($m = 0, x, y, z$). Using the approach from Eq. (2.28), we find the k-dependent Hamiltonian

$$H(k) = \vec{c}_k^{\,\dagger}(-2t\cos(k)\sigma_0 - \alpha\sin(k)\sigma_y)\vec{c}_k, \tag{2.38}$$

with $\vec{c}_k = (c_{k,\uparrow}, c_{k,\downarrow})^T$ and the eigenvalues

$$E_{1,2}(k) = -2t\cos(k) \pm \alpha\sin(k). \tag{2.39}$$

These bands are shown in Fig. 2.3 for $\alpha = 0.0\,t,\ 0.3\,t,\ 0.6\,t$. The RSO coupling splits the spin bands, but leaves their values for $k = 0$ and $k = \pm\pi$ unaffected.

2.7 Topology - Topological Numbers and Why They Affect Physics

Topology is a field of mathematics that describes which geometrical properties of objects are unaffected by smooth deformations. Smooth, in this context, means without cutting or gluing. This can be visualized by the difference between a donut and sphere. The sphere can be smoothly deformed into many objects, like a plate, a book or a table. But it cannot be deformed into a donut without cutting a hole. The donut in turn can only be deformed into objects that have exactly one hole like a bagel or a mug with a handle. Thus, the donut and the sphere are not topologically equivalent. They can be differentiated by an integer topological invariant called genus g, i.e., the number of holes. A topological invariant or topological number is a number that cannot change under smooth deformation, and thus is the same for topologically equivalent objects. In the following, we discuss how we can apply this concept to Hamil-

tonians in physics, loosely following the pedagogical approach of the online lecture in Ref. [127].

2.7.1 Topological Equivalence

In physics, the concept of topological equivalence can be applied to understand quantum phase transitions that do not break any symmetries. Historically, the quantum Hall effect was the first physical quantum phenomenon that has been described with topological order [128, 129].
Here, we focus on how to apply topological invariants to topological insulators, which have a bulk energy gap which separates the highest occupied electronic state from the lowest unoccupied state. It should be noted here that superconductors belong into this category, as they exhibit a superconducting gap around the Fermi edge, even though the naming naively suggests the opposite. In a gapped system, there is a finite energy cost to excite the system above its ground state, since there are no eigenvalues within a finite energy interval around zero energy. Two gapped systems are considered to be topologically equivalent if there is a continuous transformation from one Hamiltonians to the other without the system leaving the ground state, i.e., without closing the gap.
Let us assume two random Hamiltonian H_1 and H_2 and a continuous transformation between them:

$$H(\alpha) = \alpha H_1 + (1 - \alpha) H_2, \tag{2.40}$$

where α is a number running from 0 to 1. We can define a topological invariant Q to be the number of states below the Fermi edge $E_\mathrm{F} = 0$. Naturally, this number cannot change without a state crossing E_F. Fig. 2.4 (a) shows the eigenvalues of $H(\alpha)$ and the respective topological number Q. As the topological number Q changes with α, we find multiple different topological phases, which are not invariant towards each other, since their number of states below the Fermi edge differs.

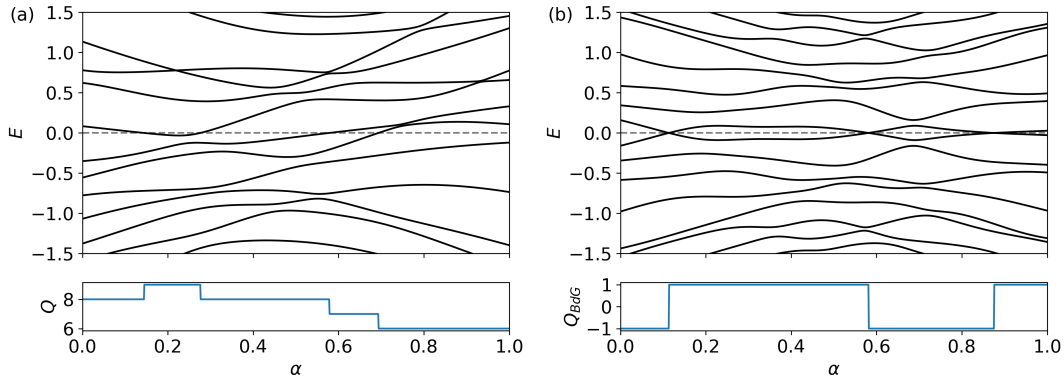

Figure 2.4: **Eigenvalues and topological numbers** Q of Hamiltonians $H(\alpha)$ with respect to α, see Eq. (2.40). In **(a)**, H_1 and H_2 are created by generating random hermitian matrices. In **(b)**, random Bogoliubov Hamiltonians are created using Eq. (2.44) by generating random hermitian H and Δ matrices.

2.7.2 Superconductors

Let us now look at superconductors and add particle-hole symmetry to our Hamiltonian and see what happens. We construct a generic superconducting Hamiltonian that has a term to create and annihilate Cooper pairs

$$\mathcal{H} = \sum_{n,m} H_{n,m} c_n^\dagger c_m + \frac{1}{2}(\Delta_{n,m} c_n^\dagger c_m^\dagger + \Delta_{n,m}^* c_n c_m), \tag{2.41}$$

with the electronic creation and annihilation operators $c_n^\dagger$ and c_n. The H term defines the electron dynamics and the Δ term the creation and annihilation of Cooper pairs. For the Hamiltonian $\mathcal{H}$ the total number of electrons is not conserved, but the parity of the electrons, i.e., whether the number of electrons is odd or even, is still conserved because the creation and destruction of Cooper pairs affect pairs of electrons, not singular electrons. We can write $\mathcal{H}$ in the Bogoliubov-de Gennes formalism using the vector $C = (c_1, ..., c_N, c_1^\dagger, ...c_N^\dagger)^T$

$$H = \frac{1}{2} C^\dagger H_{\mathrm{BdG}} C, \tag{2.42}$$

with

$$H_{\mathrm{BdG}} = \begin{pmatrix} H & \Delta \\ \Delta^* & -H \end{pmatrix}. \tag{2.43}$$

Because of the codified relation between electrons and holes in H_{BdG}, it automatically fulfills particle-hole symmetry

$$\mathcal{P} H_{\mathrm{BdG}} \mathcal{P}^{-1} = -H_{\mathrm{BdG}}, \tag{2.44}$$

with the anti-unitary operator $\mathcal{P} = \tau_x \mathcal{K}$, with the complex conjugation operator $\mathcal{K}$, and the Pauli matrix τ_x.[1] The particle-hole symmetry is the symmetry under the exchange of particles and holes. Since this symmetry operator anti-commutes with H_{BdG}, and thus introduces a minus sign, it follows that the spectrum of H_{BdG} must be symmetric around zero. For each particle eigenstate $|\Psi\rangle$ with energy E of H_{BdG}, we find a hole eigenstate $\mathcal{P}|\Psi\rangle$ with energy $-E$. Let us generate a set of two random Bogoliubov-de Gennes Hamiltonians and continuously transform them as above, see Fig. 2.4 (b). Crossings at zero energy still appear, but, because of the added symmetry, the number of states below the Fermi edge can never change. However, the number of particle states below $E_{\mathrm{F}} = 0$ still changes at the crossings, as one electron and one hole state cross zero. Thus, there is still a topological phase transition at the zero energy crossings, but it cannot be seen in the total number of states below zero. So, we need to define another topological invariant to classify H_{BdG}.

By switching to H_{BdG}, we doubled the degrees of freedom. Because of this, $\pm E$ does not refer to two distinct states, but rather a single quantum state with a superposition of particles and holes, referred to as a *Bogoliubov quasiparticle*. When a pair $\pm E_n$ crosses the Fermi edge, E_n changes sign, reflecting the change of the respective Bogoliubov quasiparticle between being energetically favorable or not. Thus, at these crossings, the ground state fermion parity switches between even and odd. The ground state fermion parity is conserved unless a Bogoliubov quasiparticle crosses zero. Thus, we can use the ground state fermion parity as our new topological number. But how do we access it efficiently?

[1] Throughout this thesis, we use τ for Pauli matrices that connect particles and holes, and σ for Pauli matrices that connect spin up and spin down.

The Pfaffian Invariant

To access the ground state fermion parity, we use the Pfaffian. For our concerns, its most notable property is that it is the square root of the determinant. For a Hamiltonian H_{BdG} with the eigenvalues $\pm E_n$, generally

$$\mathrm{Det}(H) = \prod_n -(E_n)^2. \tag{2.45}$$

Since the Pfaffian is the square root of the determinant, it is $\pm\prod_n(iE_n)$. From this, we can already see that the Pfaffian switches signs when an E_n crosses zero, i.e., when the ground state fermion parity switches. The Pfaffian is only defined for anti-symmetric matrices $A^T = -A$. To calculate it, we first must bring the Hamiltonian into an anti-symmetric form. We can do so with the unitary transformation

$$\tilde{H}_{\mathrm{BdG}} = \frac{1}{2}\begin{pmatrix} 1 & 1 \\ \mathrm{i} & -\mathrm{i} \end{pmatrix} H_{\mathrm{BdG}} \begin{pmatrix} 1 & -\mathrm{i} \\ 1 & \mathrm{i} \end{pmatrix}. \tag{2.46}$$

$$\tilde{H}_{\mathrm{BdG}} = \begin{pmatrix} H - H^* + \Delta - \Delta^* & -\mathrm{i}H - \mathrm{i}H^* + \mathrm{i}\Delta + \mathrm{i}\Delta^* \\ \mathrm{i}H + \mathrm{i}H^* + \mathrm{i}\Delta + \mathrm{i}\Delta^* & H - H^* + \Delta - \Delta^* \end{pmatrix} \tag{2.47}$$

$H + H^*$ is symmetric and $H - H^*$ anti-symmetric because H is Hermitian. The superconducting pairing Δ is anti-symmetric in nature. Thus, $\tilde{H}_{\mathrm{BdG}}$ is anti-symmetric. Using this, we can calculate our new topological invariant as

$$Q_{\mathrm{BdG}} = \mathrm{sign}\big(\mathrm{Pf}(\mathrm{i}H_{\mathrm{BdG}})\big), \tag{2.48}$$

with the Pfaffian Pf where the factor i is added to guarantee that Q_{BdG} is a real number for any size of the Hamiltonian. Q_{BdG} is a $\mathbb{Z}_2$ topological invariant, which is either $+1$ or -1 and changes signs at the crossings. In Fig. 2.4 (b) the spectrum of a smooth transition between two random BdG Hamiltonians and their respective Q_{BdG} are shown.

2.7.3 Band Theory

The concept of topological equivalence can be translated from finite systems to quasi-infinite bulk systems. For this, we define the notion of topological equivalence in momentum space, i.e., via the band structure. Insulators have an energy gap that separates the ground state and excited states. We can introduce a concept of topological equivalence based on adiabatic continuity. Two Hamiltonians are equivalent if and only if they can be slowly changed to one another with the system remaining in the ground state as defined above. As insulators have a band gap Δ_E around the Fermi edge $E_\mathrm{F} = 0$, two insulators are topologically equivalent if their Hamiltonians can be transformed into one another without closing the band gap Δ_E. Thus, at phase transitions between two topologically inequivalent phases, the energy gap vanishes.

2.7.4 Bulk-Boundary Correspondence

Imagine an interface between two topologically inequivalent phases. A parameter slowly changes spatially from one side to the other, ultimately causing a topological phase transition and thus a gap closing somewhere along the interface, as the energy gap has to go to zero at the phase transition. This results in an electronic state at zero energy that is bound to where the phase transition happens. These zero-energy states can be classified topologically. According to the bulk-boundary correspondence [130, 131] the bulk topological invariant relates to the presence of these edge states.

2.7.5 The Tenfold Way

The tenfold way is a method to categorize all gapped single-particle Hamiltonians into one of ten classes based on three symmetries [132]. In combination with the dimensionality of a given system, the tenfold way can predict what type of topological number the system has.

The first symmetry is the particle-hole symmetry. If a system is particle-hole symmetric, it is symmetric under the exchange of particles and holes. If this symmetry is present, the particle-hole exchange operator $\mathcal{P}$ anti-commutes with

the Hamiltonian H

$$\{\mathcal{P}, H\} = 0. \tag{2.49}$$

This symmetry is usually present in superconducting systems. $\mathcal{P}$ is anti-unitary and can square to -1 or $+1$.

The second symmetry is the time-reversal symmetry. A system with time-reversal symmetry will act the same when the time runs backwards: $t \to -t$. This symmetry is present if the time-reversal operator $\mathcal{T}$ commutes with H

$$[\mathcal{T}, H] = 0. \tag{2.50}$$

Typically, time-reversal symmetry is broken by magnetic fields. $\mathcal{T}$ is also anti-unitary and can square to -1 or $+1$.

The third symmetry is the chiral symmetry $\mathcal{C}$, which is equivalent to the symmetry under simultaneous reversal of the time and exchange of particles and holes. When only one of these symmetries is present but the other is absent, there is no chiral symmetry. But when neither is present on its own, it is still possible that the system is symmetric under simultaneous particle-hole exchange and time-reversal. This gives us a tenth type of matter. The chiral symmetry is present when its operator $\mathcal{C}$ anti-commutes with the Hamiltonian

$$\{\mathcal{C}, H\} = \{\mathcal{P} \cdot \mathcal{T}, H\} = 0. \tag{2.51}$$

$\mathcal{C}$ is a unitary operator and thus can only square to 1.

By combining these symmetries with the dimensionality, we can predict the type of topological number as shown in Table 2.1.

class	$\mathcal{T}^2$	$\mathcal{P}^2$	$\mathcal{C}^2$	$D=1$	$D=2$	$D=3$
A					$\mathbb{Z}$	
AIII			1	$\mathbb{Z}$		$\mathbb{Z}$
AI	1					
BDI	1	1	1	$\mathbb{Z}$		
D		1		$\mathbb{Z}_2$	$\mathbb{Z}$	
DIII	-1	1	1	$\mathbb{Z}_2$	$\mathbb{Z}_2$	$\mathbb{Z}$
AII	-1				$\mathbb{Z}_2$	$\mathbb{Z}_2$
CII	-1	-1	1	$\mathbb{Z}$		$\mathbb{Z}_2$
C		-1			$\mathbb{Z}$	
CI	1	-1	1			$\mathbb{Z}$

Table 2.1: **The tenfold way.** The table shows which type of topological number a system has, based on the squares of its time-reversal symmetry $\mathcal{T}$, particle-hole symmetry $\mathcal{P}$, and chiral symmetry $\mathcal{C}$, in combination with its dimension D. An empty field in the table means the absence of a given symmetry or the lack of a topological number. $\mathbb{Z}_2$ describes a binary topological number, e.g., one that can take the values ± 1 like the Pfaffian introduced above. $\mathbb{Z}$ refers to an integer topological number like the Chern number [133].

2.8 Majoranas and Where to Find Them

2.8.1 The Kitaev Chain and Majorana Zero Modes

In this section, we introduce the Kitaev chain. The Kitaev chain is the most minimalist known 1D model that can host so-called Majorana zero modes which we will also introduce in this section. The pedagogical approach in this section is inspired by the online lecture notes [127].

We define fermionic creation and annihilation operators $c^\dagger$ and c that satisfy the anticommutator relation $c^\dagger c + cc^\dagger = 1$ and square to zero $c^2 = (c^\dagger)^2 = 0$. They connect the vacuum state $|0\rangle$ and the filled state with one particle $|1\rangle$ as follows:

$$c^\dagger |0\rangle = |1\rangle\,, \quad c\,|1\rangle = |0\rangle\,, \quad c\,|0\rangle = 0, \quad c^\dagger\,|1\rangle = 0. \tag{2.52}$$

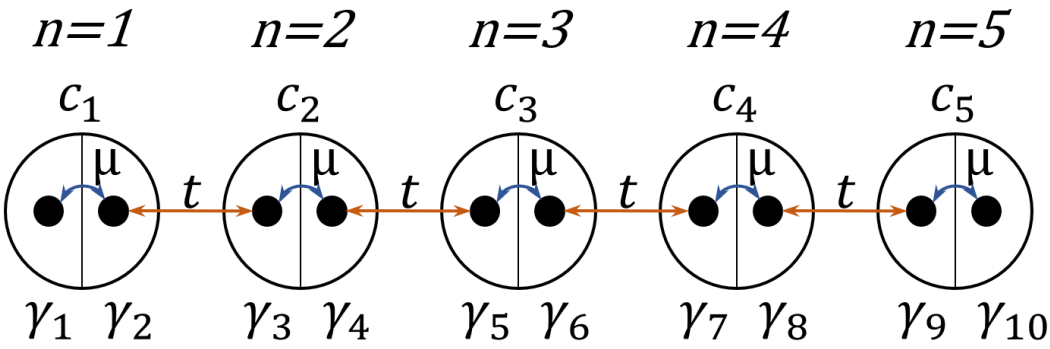

Figure 2.5: **Sketch of Majorana pairing** for $N = 5$. The black dots represent Majoranas. The black circles represent electronic sites. Within an electronic site, the Majoranas are coupled by μ. Between two neighboring electronic sites, the Majoranas are coupled by t.

They can also be written as

$$c^\dagger = \frac{1}{2}(\gamma_1 + \mathrm{i}\gamma_2), \quad c = \frac{1}{2}(\gamma_1 - \mathrm{i}\gamma_2), \tag{2.53}$$

with the Majorana operators γ_1 and γ_2. The inverted transformation

$$\gamma_1 = c + c^\dagger, \quad \gamma_2 = \mathrm{i}(c - c^\dagger), \tag{2.54}$$

shows that $\gamma_1 = \gamma_1^\dagger$ and $\gamma_2 = \gamma_2^\dagger$. The Majorana operators owe their name to this property, in reference to proposed Majorana particles, which are their own anti-particles [134, 135]. In the framework of solid state physics, this property means that a Majorana mode cannot be 'empty' or 'filled'. Using the properties of c, we can calculate that

$$\gamma_1\gamma_2 + \gamma_2\gamma_1 = 0, \quad \gamma_1^2 = 1, \quad \gamma_2^2 = 1. \tag{2.55}$$

The Majorana operators still act on the states $|0\rangle$ and $|1\rangle$. For example, a Hamiltonian $H = \epsilon c^\dagger c$, which describes an energy difference of ϵ between the two states, can be written as $H = \frac{1}{2}\epsilon(1 - \mathrm{i}\gamma_1\gamma_2)$.

Now that we represent a single fermion with two Majorana modes, the question occurs whether it is possible to have a single isolated Majorana mode not close to its partner Majorana mode. Naively, one might guess 'no' as condensed

matter systems are made out of electrons corresponding to pairs of Majoranas. But, we can engineer a Hamiltonian that makes this possible.

To construct this Hamiltonian, we consider N fermionic sites with creation and annihilation operators $c_n^\dagger$ and c_n. This is equivalent to each site having two Majorana modes γ_{2n-1} and γ_{2n}, see Fig. 2.5. We can pair the Majoranas by adding an energy cost for each fermionic site to be occupied, resulting in the Hamiltonian

$$H = \frac{\mathrm{i}}{2}\mu \sum_{n=1}^{N} \gamma_{2n-1}\gamma_{2n}. \tag{2.56}$$

This leads to no unpaired Majoranas. All excitations have an energy of $\pm|\mu|/2$, the bulk spectrum is gapped and there are no zero-energy edge states.
Now, we instead only pair Majorana operators from neighboring sites with a coupling factor $\mathrm{i} \cdot t$. In the electron basis, this means that we assign an energy difference of $2t$ between an empty state and a neighboring filled state, i.e., the energy associated with an electron going from one site to the next.

$$H = \mathrm{i}t \sum_{n=1}^{N-1} \gamma_{2n+1}\gamma_{2n} = 0 \cdot \gamma_1\gamma_{2N} + \mathrm{i}t \sum_{n=1}^{N-1} \gamma_{2n+1}\gamma_{2n} \tag{2.57}$$

The end modes do not appear in this Hamiltonian, which is equivalent to them being associated with zero energy. All other excitations have an energy of $\pm|t|$. This results in a gapped bulk spectrum with zero-energy states at the ends of the chain.

The Kitaev Model

We combine the Eq. (2.56) with Eq. (2.57) and add superconducting pairing using $\gamma_{2n-1} = (c_n^\dagger + c_n)$ and $\gamma_{2n} = -\mathrm{i}(c_n^\dagger - c_n)$ to construct the Kitaev model

$$H = -\mu \sum_n \left(c_n^\dagger c_n - \frac{1}{2} \right) - t \sum_n \left(c_{n+1}^\dagger c_n + \text{h.c.} \right) + \Delta \sum_n \left(c_{n+1} c_n + \text{h.c.} \right), \tag{2.58}$$

with the onsite energy μ, the hopping term t, and the superconducting pairing Δ. For $t = \Delta = 0$, this Hamiltonian is identical to the completely trivial case

in Eq. (2.56). For $\mu = 0$ and $\Delta = t$, it is identical to the case with edge mode from Eq. (2.57).
Now, we bring the Kitaev model into the Bogoliubov-de Gennes formalism.

$$H = \frac{1}{2} C^\dagger H_{\mathrm{BdG}} C, \tag{2.59}$$

with $C = (c_1, ..., c_N, c_1^\dagger, ...c_N^\dagger)^T$ and a $2N \times 2N$-matrix H_{BdG}. We can write H_{BdG} in a compact form with Pauli matrices τ_i $(i = 0, x, y, z)$ and basis vectors $|n\rangle = (0, ..., 1, 0, ...)^T$ with the 1 on the n-th site of the chain. For example, we can write $2c_n^\dagger c_n - 1 = C^\dagger (\tau_z \otimes |n\rangle \langle n|) C$ with the Kronecker product $\otimes$. In this form H_{BdG} reads

$$H_{\mathrm{BdG}} = -\sum_n^N \mu (\tau_z \otimes |n\rangle \langle n|) - \sum_n^{N-1} \left[(t\tau_z + \mathrm{i}\Delta\tau_y) \otimes |n\rangle \langle n+1| + \mathrm{h.c.} \right]. \tag{2.60}$$

For the researchers getting into this field, it should be noted that it is very common in the literature to not write a Kronecker product and merely imply it to make equations more compact. Often, this is done without ever noting that a Kronecker product was used at all, which can lead to confusion. When reading literature in the field, and matrix sizes seemingly make no sense, it is often a good first step to check, whether the equation makes sense when adding Kronecker products. So with this more common compact notation the BdG-Hamiltonian reads

$$H_{\mathrm{BdG}} = -\sum_n^N \mu\tau_z |n\rangle \langle n| - \sum_n^{N-1} \big[(t\tau_z + \mathrm{i}\Delta\tau_y) |n\rangle \langle n+1| + \mathrm{h.c.} \big]. \tag{2.61}$$

The BdG Hamiltonian is particle-hole symmetric with $\mathcal{P} H_{\mathrm{BdG}} \mathcal{P}^{-1} = -H_{\mathrm{BdG}}$ with $\mathcal{P} = \tau_x \mathcal{K}$, i.e., exchanging particles and holes changes the sign of H_{BdG}.
Now, it might be objected that the zero modes so far only appeared for exactly tuned parameters, and that if a specific solution only exists for exact parameters with no room for error, it will be extremely unlikely to actually occur in experiments. To counteract this argument, Fig. 2.6 shows the eigenvalue spectrum of a chain with length $N = 100$ and $\Delta = 0.5\, t$ with respect to μ. For

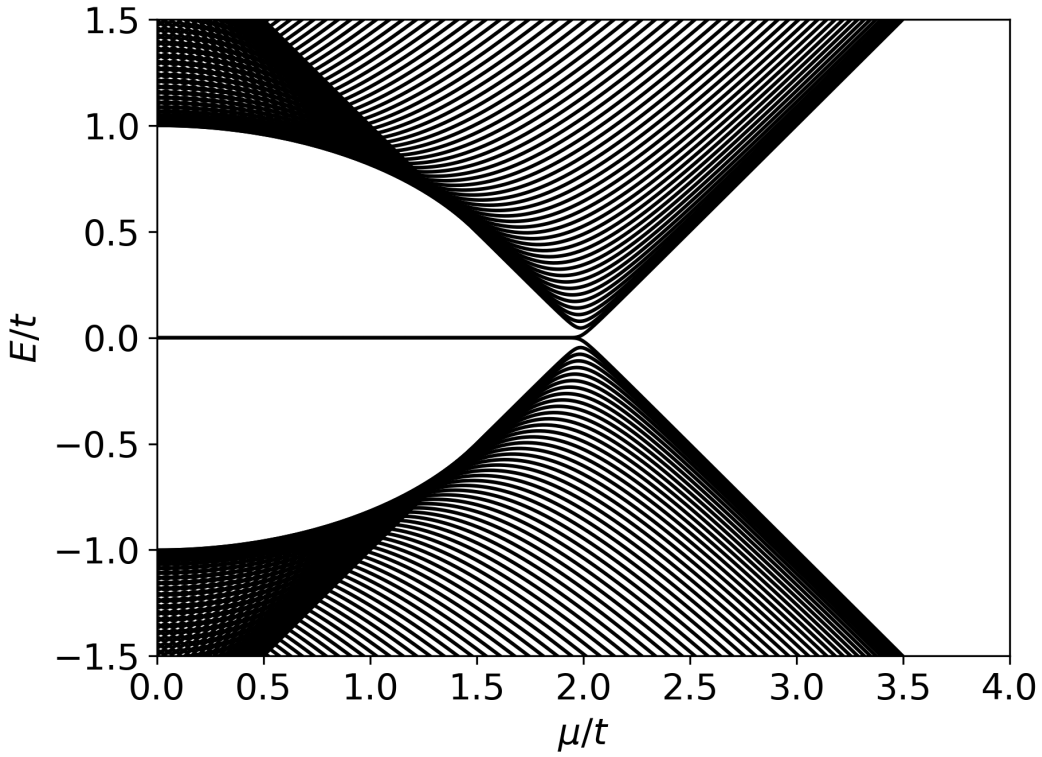

Figure 2.6: **Eigenvalue spectrum** of Eq. (2.60) with respect to μ for $N = 100$ and $\Delta = 0.5\,t$.

$\mu \lesssim 2t$, we find Majorana zero modes. Around $\mu \sim 2t$ the bulk gap closes and for larger μ no zero modes are to be found. Note that the eigenvalue spectrum is mirrored for negative μ. To make sense of this, we need to remember a few things. First, the Hamiltonian is particle-hole symmetric. Thus, the spectrum is mirrored at zero energy. Second, for $\mu = 0$, there are two zero-energy states, each localized at one end of the chain and thus far away from each other. Because of the particle-hole symmetry, they cannot be moved from zero energy individually (one has to shift down, while the other is shifting up). In the presence of an energy gap, they can only be moved from zero energy when they couple to each other, but this coupling is suppressed by the distance between the two ends. Thus, the two zero energy modes cannot split away from zero energy unless the bulk gap closes, which happens at $\mu = 2t$. In conclusion, Majorana modes are protected by the symmetry of the spectrum and absence

of zero-energy excitation. This sudden change in behavior at zero energy crossings (gap closings) reminds us of the discussion on topology in the previous section. In the following, we show how to apply topological methods to predict the occurrence of Majorana zero modes from the bulk Hamiltonian.

Kitaev Chain in Momentum Space

To discuss the bulk properties, we first go to momentum space. We connect the last site of the chain to the first site, turning the Kitaev chain into a Kitaev ring. This introduces translational symmetry $|n\rangle \rightarrow |n+1\rangle$. With a Fourier transformation, we bring the Hamiltonian to momentum space. For this, a state with momentum k is given by

$$|k\rangle = \frac{1}{\sqrt{N}} \sum_{n=1}^{N} e^{-\mathrm{i}kn} |n\rangle \tag{2.62}$$

with the periodic boundary condition $\langle k|n=0\rangle = \langle k|n=N\rangle$. We consider very large N for the bulk system. Thus, we can consider k to be continuous and limited to the interval $[-\pi, \pi]$ with periodic boundaries. We can write the k-dependent BdG Hamiltonian

$$H(k) = \langle k| H_{\mathrm{BdG}} |k\rangle = \big(-\mu - 2t\cos(k)\big)\tau_z + 2\Delta \sin(k)\tau_y. \tag{2.63}$$

The full momentum space BdG Hamiltonian can be obtained by

$$H_{\mathrm{BdG}} = \sum_k H(k) |k\rangle \langle k| , \tag{2.64}$$

where the sum becomes an integral in the limit of an infinite chain.

Band Structure

The band structure can be calculated by diagonalizing the 2×2 matrix Eq. (2.63), which yields the eigenvalue spectrum

$$E_{\pm}(k) = \pm\sqrt{(\mu + 2t\cos(k) + 4\Delta^2\sin^2(k)}. \tag{2.65}$$

From this, we can see that the spectrum is gapped for all k in both, the non-trivial regime (e.g., $\mu = 0$, $t = \Delta$) and the trivial regime (e.g., $\mu = 3t$, $t = \Delta$). This is unsurprising, since there are no ends in the bulk system. So, it cannot have end states. From the bands, we can identify two gap closings, one at $\mu = 2t$ and $k = \pi$, the other at $\mu = -2t$ and $k = 0$. These gap closings mark the topological phase transitions. The band structure itself looks very similar in the trivial and non-trivial phase. So, we cannot easily identify the topological phase by just looking at the band structure. Therefore, we need a more sophisticated method to distinguish the topological phases. This is where the Majorana number comes into play.

The Majorana Number

The Majorana number is the bulk topological invariant of the Kitaev chain and similar systems and can be calculated from the k-dependent bulk Hamiltonian (Eq. (2.63)). The full derivation can be found in Kitaev's original paper [5]. Here, we will only focus on how to calculate the Majorana number and present arguments to make it plausible.
The Majorana number M is calculated as the sign of the product of the Pfaffians of the k-dependent Hamiltonian $H(k)$ at the points $k = 0$ and $k = \pi$

$$M = \mathrm{sgn}(\mathrm{Pf}[\mathrm{i}\tilde{H}(k=0)]\mathrm{Pf}[\mathrm{i}\tilde{H}(k=\pi)]). \tag{2.66}$$

To calculate the Pfaffian, $H(k = 0)$ and $H(k = \pi)$ must first be brought into anti-symmetric form. Particle-hole symmetry means that $\mathcal{P}H(k)\mathcal{P}^{-1} = -H(-k)$. In 1D, the points $k = 0$ and $k = \pi$ are the symmetry points of the

Brillouin zone and reflected onto themselves, thus

$$\mathcal{P}H(0)\mathcal{P}^{-1} = -H(0) \text{ and } \mathcal{P}H(\pi)\mathcal{P}^{-1} = -H(\pi). \tag{2.67}$$

Because of this, it is always possible to bring $H(0)$ and $H(\pi)$ into anti-symmetric form via a unitary transformation

$$\begin{aligned} \tilde{H}(0) &= \frac{1}{2}\begin{pmatrix} 1 & 1 \\ \mathrm{i} & -\mathrm{i} \end{pmatrix}(-2t-\mu)\tau_z \begin{pmatrix} 1 & -\mathrm{i} \\ 1 & \mathrm{i} \end{pmatrix} = -\mathrm{i}\begin{pmatrix} 0 & -2t-\mu \\ 2t+\mu & 0 \end{pmatrix}, \\ \tilde{H}(\pi) &= \frac{1}{2}\begin{pmatrix} 1 & 1 \\ i & -i \end{pmatrix}(2t-\mu)\tau_z \begin{pmatrix} 1 & -\mathrm{i} \\ 1 & \mathrm{i} \end{pmatrix} = -\mathrm{i}\begin{pmatrix} 0 & 2t-\mu \\ -2t+\mu & 0 \end{pmatrix}. \end{aligned} \tag{2.68}$$

The Pfaffians are then

$$\begin{aligned} \mathrm{Pf}\big(\mathrm{i}H(0)\big) &= -2t-\mu \\ \mathrm{Pf}\big(\mathrm{i}H(\pi)\big) &= 2t-\mu. \end{aligned} \tag{2.69}$$

and the Majorana number of the Kitaev chain is

$$M = \mathrm{sgn}\left[(-2t-\mu)(2t-\mu)\right] = \mathrm{sgn}\left[\mu^2 - 4t^2\right]. \tag{2.70}$$

Therefore, the sign of M changes at $\mu = \pm 2t$, which lines up with the previous findings on the gap closings and the topological phases.
As we discussed in Sec. 2.7.2, a change in sign of the Pfaffian indicates a parity switch and thus a pair of eigenvalues passing the Fermi energy. So it intuitively makes sense to make use of the Pfaffian. But why do we calculate the product of the Pfaffians for $k = 0$ and $k = \pi$ instead of, for example, constructing some formula that employs all possible values of k? The points $k = 0$ and $k = \pi$ are the symmetry points of the Brillouin zone. They are the only points that are mirrored onto themselves, and the k-points between them effectively contain the complete information of the Brillouin zone, as the Brillouin zone itself is mirrored at these points. If M is positive/negative, we know that there is an even/odd number of (avoided) crossings. When M changes, an (avoided) crossing is added or removed. To add or remove a crossing by a continuous

transformation, the band gap must momentarily close, indicating a topological phase transition. Thus, the Majorana number cannot change under continuous transformations without a gap closing.
Finally, we find that the system is in the non-trivial phase for $M = -1$ and in the trivial phase for $M = +1$.

2.8.2 From the Kitaev Chain to Realistic Chains with Proximity-Induced s-Wave Superconductivity

The Kitaev chain is the simplest model that can host Majoranas, but it is somewhat far away from realistic systems. Here, we show how to adapt the Kitaev chain to a model with more realistic assumptions step by step.
We start with the Kitaev chain

$$H_{\text{Kitaev}} = -\sum_{n}^{N} \vec{c}_n^{\dagger} \mu \tau_z \vec{c}_n - \sum_{n}^{N-1} \left[\vec{c}_n^{\dagger} (t\tau_z + \mathrm{i}\Delta\tau_y) \vec{c}_{n+1} + \text{h.c.} \right], \tag{2.71}$$

with $\vec{c_n} = (c_n, c_n^{\dagger})^T$, the chemical potential μ, the hopping parameter t, the superconducting order parameter Δ, and the Pauli matrices τ_i with $i \in \{0, x, y, z\}$. First, we shift our chemical potential $\mu \to \mu - 2t$ to make it easier to define μ with respect to the band bottom. With this, the topological phase transition between trivial and non-trivial states occurs at $\mu = 0$. So far, this is only a change in definitions and no functional change.
The Kitaev chain is formulated for spinless fermions. To make the model more realistic, we add spin to all electrons and holes, and add an interaction in spin space, mediated by an additional set of Pauli matrices σ_i with $i \in \{0, x, y, z\}$. This expands our bases to $\vec{c}_n = (c_{n,\uparrow}, c_{n,\downarrow}, c_{n,\uparrow}^{\dagger}, c_{n,\downarrow}^{\dagger})^T$

$$H = \sum_{n}^{N} \vec{c}_n^{\dagger} (2t - \mu)(\tau_z \otimes \sigma_0) \vec{c}_n - \sum_{n}^{N-1} \left[\vec{c}_n^{\dagger} (t(\tau_z \otimes \sigma_0) + \mathrm{i}\Delta(\tau_y \otimes \sigma_0)) \vec{c}_{n+1} + \text{h.c.} \right], \tag{2.72}$$

with the Kronecker product $\otimes$ and σ_0 as the unity matrix. From here on, we will use a simplified notation common in literature. τ_i and σ_i both represent the same Pauli matrices with $i \in \{0, x, y, z\}$, where the 0-th Pauli matrix is a

2×2 unity matrix. The Kronecker product $\otimes$ will not be explicitly written and is implied between a τ_i and a σ_i. The only difference between τ_i and σ_i is whether they are on the left (τ_i) or right (σ_i) of the Kronecker product, which is non-commutative. Given our choice of basis, this implies that τ_i describe how electrons and holes interact, while σ_i describe how spin up and spin down interact. Lastly, we should note here that it is also common in literature to not explicitly write τ_0 and σ_0 and just imply them instead. We specifically choose to keep the unitary matrices for easier readability. So, with this notation, the above Hamiltonian reads

$$H = \sum_n^N \vec{c}_n^\dagger (2t - \mu)\tau_z\sigma_0\vec{c}_n - \sum_n^{N-1} \left[\vec{c}_n^\dagger (t\tau_z\sigma_0 + \mathrm{i}\Delta\tau_y\sigma_0)\vec{c}_{n+1} + \mathrm{h.c.}\right]. \tag{2.73}$$

So far, this just added an extra degeneracy, but this already creates the first problem. The reason why the Kitaev chain is interesting to us is that it can host unpaired Majorana modes. With a fully twofold degenerate spectrum, each end of the chain would host two Majorana modes, which combine to just a regular fermion tuned to zero energy. So, how can we lift this degeneracy? One way is to apply an external magnetic field and Zeeman coupling $-B_z(c_\uparrow^\dagger c_\uparrow - c_\downarrow^\dagger c_\downarrow - c_\uparrow c_\uparrow^\dagger + c_\downarrow c_\downarrow^\dagger) = \vec{c}_n^\dagger B_z\sigma_z\tau_z\vec{c}_n$, which results in the Hamiltonian

$$H = \sum_n^N \vec{c}_n^\dagger \left((2t - \mu)\tau_z\sigma_0 - B\tau_z\sigma_z\right)\vec{c}_n - \sum_n^{N-1} \left[\vec{c}_n^\dagger (t\tau_z\sigma_0 + \mathrm{i}\Delta\tau_y\sigma_0)\vec{c}_{n+1} + \mathrm{h.c.}\right]. \tag{2.74}$$

With sufficiently large Zeeman splitting, the electrons of different spin can be separated, which allows us to make one spin species trivial and the other non-trivial. Thus, we can find unpaired Majorana modes at the ends of the chain again.

Now, the Hamiltonian contains spin information, but we still rely on p-wave superconductors, since the Δ-term creates spin-triplet Cooper pairs with identical spin

$$\vec{c}_n^\dagger(\mathrm{i}\Delta\tau_y\sigma_0)\vec{c}_{n+1} = \Delta\left(c_{n,\uparrow}^\dagger c_{n+1,\uparrow}^\dagger + c_{n,\downarrow}^\dagger c_{n+1,\downarrow}^\dagger - c_{n,\uparrow}c_{n+1,\uparrow} - c_{n,\downarrow}c_{n+1,\downarrow}\right). \tag{2.75}$$

Even though some experimental indications for p-wave superconductors have been found, they appear to be extremely rare in nature [109–112]. Given that there are many known s-wave superconductors, a good next step is to change the pairing to s-wave. It should be noted here that s-wave superconductivity in a pure 1D system is not fully realistic, but we can work around that by assuming that the superconductivity is proximity-induced and stems from a superconducting substrate. For s-wave pairing, we need a term to create Cooper pairs in spin-singlet states $H_{\text{s-wave}} = \Delta(c_\uparrow c_\downarrow - c_\downarrow c_\uparrow) + \text{h.c.}$. Before we introduce this term to our Hamiltonian, we change the basis to $\vec{c}_n = (c_{n,\uparrow}, c_{n,\downarrow}, c^\dagger_{n,\downarrow}, -c^\dagger_{n,\uparrow})^T$. This basis mostly makes the Hamiltonian more convenient to read and write. The s-wave pairing is just $\Delta\tau_x\sigma_0$ in this basis. The Hamiltonian of holes can be calculated directly from the Hamiltonian of electrons by changing the sign of all terms that respect time-reversal symmetry, while leaving the signs of terms that break time-reversal symmetry, such as the Zeeman term. In this basis, the Hamiltonian reads

$$H = \sum_n^N \vec{c}_n^\dagger \big((2t-\mu)\tau_z\sigma_0 - B\tau_0\sigma_z + \Delta\tau_x\sigma_0\big)\vec{c}_n - \sum_n^{N-1} \left[\vec{c}_n^\dagger (t\tau_z\sigma_0)\vec{c}_{n+1} + \text{h.c.}\right]. \tag{2.76}$$

Now, we have a new problem. For this Hamiltonian, there is no parameter set that leads to an open band gap that is simultaneously non-trivial. The above Hamiltonian only has one Pauli matrix interacting with the spin, which is σ_z. Thus, the spin of each electron is conserved. So when bands cross zero energy from tuning B, they have opposite spin and do not couple. Therefore, the gap closes.

To find non-trivial states, we need to open the gap again. One way to reopen the gap, is to include Rashba spin-orbit (RSO) coupling $H_{\text{RSO}} = i\frac{\alpha}{2}\tau_z\sigma_y$ (see. Sec. 2.6)

$$\begin{aligned} H = &\sum_n^N \vec{c}_n^\dagger \big((2t-\mu)\tau_z\sigma_0 - B\tau_0\sigma_z + \Delta\tau_x\sigma_0\big)\vec{c}_n \\ &+ \sum_n^{N-1} \left[\vec{c}_n^\dagger (-t\tau_z\sigma_0 + i\frac{\alpha}{2}\tau_z\sigma_y)\vec{c}_{n+1} + \text{h.c.}\right]. \end{aligned} \tag{2.77}$$

The RSO coupling causes the spin of each electron to not be conserved anymore and therefore couples crossing bands. This causes the gap to open again. It has been shown by Oreg et al. [9] and Lutchyn et al. [10] that, with the interplay of the s-wave superconductivity, a magnetic field, and RSO coupling, effective p-wave pairing can occur even though we use a conventional s-wave superconductor. This allows us to find Majoranas. Perge et al. have shown that this effective p-wave pairing can also be achieved by a spin spiral state in proximity to a superconducting host without explicit spin-orbit coupling [8]. Summarizing the above, we need a magnetic field plus Rashba spin-orbit coupling or a spin spiral state in addition to s-wave pairing to make a topologically non-trivial state possible in a realistic system. It should be noted that this list of ingredients is specific to one- and two-dimensional class D and class BDI materials. In the following, we explain how the effective p-wave pairing occurs.

Effective p-Wave Pairing

The Kitaev chain features p-wave superconducting pairing and requires a 'spinless' system, i.e., a system with one pair of Fermi points. Following the derivation of Oreg et al. [9], we consider a wire in x-direction, with a magnetic Zeeman field in z-direction, Rashba spin-orbit coupling in y-direction, and proximity-induced superconductivity

$$\begin{aligned} H &= \int \Psi^\dagger(x)\mathcal{H}\Psi(x)dy \quad \text{with} \quad \Psi^\dagger = (\psi_\uparrow^\dagger, \psi_\downarrow^\dagger, \psi_\downarrow, -\psi_\uparrow) \\ \mathcal{H} &= (k^2/2m - \mu)\tau_z\sigma_0 + \mathrm{i}\alpha k\tau_z\sigma_y + B\tau_0\sigma_z + \Delta\tau_x\sigma_0 \end{aligned} \tag{2.78}$$

where $\psi_\uparrow(x)$ annihilates an electron with spin up at position x. The energy spectrum of this Hamiltonian can be calculated as follows:

$$E_{1,2,3,4} = \pm\sqrt{B^2 + \Delta^2 + \xi_k^2 + \alpha^2k^2 \pm 2\sqrt{B^2\Delta^2 + B^2\xi_k^2 + \alpha^2k^2\xi_k^2}}, \tag{2.79}$$

with $\xi_k = \frac{k^2}{2m} - \mu$. The resulting dispersion relation is shown in Fig. 2.7 for a few sets of parameters. First, we consider the case of $B = \Delta = 0$. The dispersion relation consists of two shifted parabolas (mirrored because

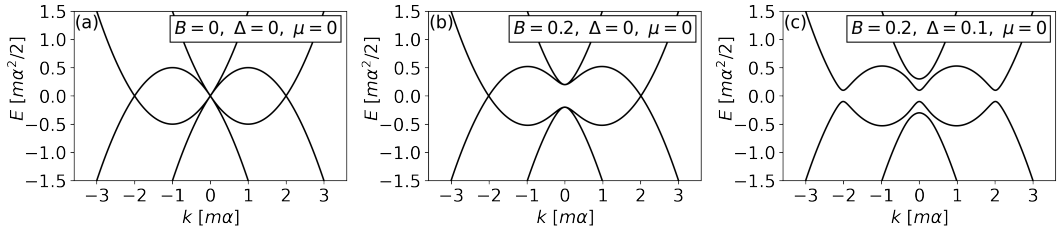

Figure 2.7: **Dispersion relation for a model with effective p-wave pairing.** For the calculation, we set $m = 1$ and $\alpha = 1$ and use $m\alpha$ as our unit of momenta, and $m\alpha^2/2$ as our unit of energy. **(a)** $B = \Delta = \mu = 0$, **(b)** $B = 0.2,\ \Delta = 0,\ \mu = 0$, **(c)** $B = 0.2,\ \Delta = 0.1,\ \mu = 0$.

of the system's particle-hole symmetry). Since there are four Fermi points, no 'spinless' regime is possible for this case. Increasing the magnetic field B causes a band gap opening proportional to $|B|$ at $k = 0$. When μ lies within that gap, there is a single pair of Fermi points as desired for the 'spinless' system. When we now turn on Δ, we effectively get p-wave pairing in the lower bands, because spin-orbit coupling favors opposite spins when pairing opposite momenta k and $-k$. Looking at the bands with a minus within the square root, we find that the size of the gap at $k = 0$ is

$$\delta E(k = 0) = |B - \sqrt{\Delta^2 + \mu^2}|. \tag{2.80}$$

At $B^2 = \Delta^2 + \mu^2$, the gap closes and a band crossing occurs, resulting in a topological phase transition. For $B^2 < \Delta^2 + \mu^2$, both gaps are dominated by the superconducting pairing, and the system is in a trivial state. For $B^2 > \Delta^2 + \mu^2$, the gap at $k = 0$ is dominated by the magnetic field B, and the system is in a topologically non-trivial state with Majorana zero modes at the ends of the wire.

Chapter 3

Models and Methods

In this chapter, we introduce the models and methods used in this thesis. In Sec. 3.1, we begin by introducing the tight-binding model for a one-dimensional chain featuring magnetism, Rashba spin-orbit coupling, and proximity-induced s-wave superconductivity. In Sec 3.2, we discuss how to identify magnetic ground states with the Metropolis Monte-Carlo method. Following up on that, we describe how to adapt this method to different systems in Sec. 3.3. Thereafter, we discuss how to calculate the total energy of all occupied states in a tight-binding model in Sec. 3.4. In Sec. 3.5, we calculate the analytical eigenvalues of the model presented in Sec. 3.1 for the case of harmonic spin spirals. In Sec. 3.6 and 3.7, we show how we calculate the Majorana number for bulk and finite-size systems, respectively. In Sec. 3.8, we give a brief introduction to scanning tunneling microscopy to explain the methods used in the experiments that are the basis for the calculations presented in Chapters 6 and 7.

3.1 Tight-Binding Model for a Spinful 1D Chain with Proximity-Induced Superconductivity

The Kitaev chain, see Sec. 2.8.1, has a problem for experimental realization. It is a p-wave superconductor, and p-wave superconducting materials appear to be rare and difficult to find, although experimental evidence for p-wave superconductivity has been found in a handful of sample systems recently [109–112]. Since most known superconductors are s-wave superconductors, building an s-wave superconducting model system which can host Majoranas is a natural step towards the realization of Majorana zero modes. This can be achieved by

adding magnetic interactions with local magnetic Zeeman-fields to an s-wave superconducting system, when combined with a spin spiral structure or Rashba spin-orbit coupling, which leads to an effective p-wave pairing [8]. Using this knowledge, we construct the following Hamiltonian

$$\begin{aligned} H =& \sum_{j=1}^{L} \vec{c}_j^{\,\dagger} \big[- J\tau_0 \vec{s}_j \cdot \vec{\sigma} + (2t - \mu)\tau_z\sigma_0 + \Delta\tau_x\sigma_0 \big] \vec{c}_j \\ &+ \sum_{\langle i,j\rangle_1} \vec{c}_i^{\,\dagger} \big[- t\tau_z\sigma_0 + i\frac{\alpha}{2}\tau_z\sigma_y \big] \vec{c}_j, \end{aligned} \tag{3.1}$$

with the Nambu spinor $\vec{c}_j = (c_{j,\uparrow}, c_{j,\downarrow}, c^\dagger_{j,\downarrow}, -c^\dagger_{j,\uparrow})$ [136], the coupling strength J between a magnetic moment on a given site and the spin of a conducting electron, the orientation $\vec{s}_j$ of the local magnetic moment on the j-th site, the chemical potential μ, the hopping amplitude t, the length of the chain L, the Rashba spin-orbit coupling constant α, and the superconducting order parameter Δ, which we assume to be constant along the chain. The local magnetic moments on each atomic site represent quasi-classical spins whose interactions are mediated by itinerant electrons, which is an approximation for atoms with large total spin (e.g, 7/2). The Pauli matrices σ and τ are connected by a Kronecker product and operate in spin and particle-hole space, respectively. This Hamiltonian effectively includes spin interactions mediated by the itinerant electrons and neglects direct interactions between the spins. We choose a Rashba spin-orbit coupling in the σ_y direction without loss of generality. As this is the only non-isotropic term in the Hamiltonian, i.e., the only term that is not invariant under global rotation, this choice can be made freely as long as we make sure that the RSO coupling is perpendicular to the direction of the chain. By the local gauge transformation $c = e^{ij\theta\sigma_y} c'$ [31], the Rashba spin-orbit coupling can be rotated into the magnetic moments $\vec{s}\,'_j = R(2j\theta)\vec{s}_j$, where R is the rotation matrix around the y-axis by an angle of $2j\theta$. To fully rotate Rashba spin-orbit coupling of strength α into the local magnetic moments, one has to set $\theta = \arctan(\alpha/t)$, which rescales the hopping term to $t' = t\sqrt{1 + \frac{\alpha^2}{t^2}}$ and rotates the magnetic moments around the y-axis by an angle of $2j \cdot \arctan(\alpha/t)$. In Chapter 4, where we identify the magnetic

ground states of this model, we therefore restrict our analysis to $\alpha = 0$ and $t = 1$. The results for non-vanishing Rashba spin-orbit coupling can be obtained from the presented results by a backrotation of each magnetic moment $\vec{s}_j$ by $-2j \cdot \arctan(\alpha/t)$ and rescaling of all energies by $\sqrt{1 + \frac{\alpha^2}{t^2}}^{-1}$.

3.2 Finding Magnetic Ground States with the Metropolis Monte-Carlo Algorithm

In this section, we describe how to find the magnetic ground state of a given system with Metropolis Monte-Carlo algorithms. Monte-Carlo simulations are a broad class of methods that use randomness and probability theory to find numerical solutions. In general, a Metropolis algorithm iterates evolving samples accepting or rejecting changes to the samples based on a probability distribution. Here, we focus specifically on the application of the Metropolis algorithm to magnetic systems with three-dimensional classical or quasi-classical spins, utilizing the Boltzmann distribution as the aforementioned probability distribution [137, 138]. Assume a system with N spins $\vec{s}_i$ and a total energy $E(\vec{s}_1, ..., \vec{s}_N)$ which depends on the alignment of those spins, e.g., classical spins as introduced in Sec. 2.3 or quasi-classical spins as in the model introduced in Sec. 3.1. First, a random spin configuration is generated and the respective total energy calculated. Then, the following steps are applied:

1. One random spin $\vec{s}_i$ is chosen.
2. The chosen spin is changed by picking a random value from a continuous distribution of vectors on the unit sphere.
3. The total energy of the new configuration E_{new} is calculated and compared to the total energy of the previous configuration E_{old}.
   (a) If $E_{\text{new}} < E_{\text{old}}$, the new configuration is accepted.
   (b) If $E_{\text{new}} > E_{\text{old}}$, the new configuration is either accepted with a probability equal to the Boltzmann distribution $\exp(\frac{E_{\text{old}} - E_{\text{new}}}{k_B T})$ or declined.

Performing these steps N times is called a Monte-Carlo step [137]. These steps are repeated while the temperature T is progressively reduced in a slow annealing approach to the equilibrium, which in turn lowers the probability of accepting new states with a higher energy. Occasionally accepting states with a higher than previous energy, allows the system to get out of local minima. As the system approaches the ground state, updating spins by picking from a full unit sphere becomes very inefficient. For example, the system might be already almost ferromagnetically aligned, but most spins are off by only a few degrees. In that scenario, picking fully random spins would lead to testing primarily less favorable configurations. To circumvent that, we update the spins only by small random rotations, randomly rotating them by up to 0.03π in each rotational direction, at low temperatures. We consider a simulation to be convergent when a large increase in the total number of steps shows no further reduction in total energy of the final state, using spot checks with up to 10 times more steps.

Example of a Simple System

To illustrate the method described above, we use it to find the ground state of a very simple magnetic model. Let us consider a system of 10×10 Heisenberg spins $\vec{s}_i$ which are coupled only by first neighbor exchange interactions, so that the total energy of the system is

$$E = \sum_{\langle i,j \rangle} J \vec{s}_i \cdot \vec{s}_j, \tag{3.2}$$

with the magnetic exchange J and the summation over nearest neighbors $\langle i, j \rangle$. We choose $J = -1$ meV, which means that E is minimal when all $\vec{s}_i$ are identical, i.e., when the system is ferromagnetically aligned. In Fig. 3.1 (a), we visualize how the system begins in chaos and slowly approaches its ground state. In the panels (b,c,d), we show the corresponding temperature chosen for each step, the absolute value of the magnetization $|M| = |\sum_i \vec{s}_i/N|$, and the total energy E, respectively. In this example, the temperature is chosen to fall logarithmically from $T = 10$ °K to $T = 0.03$ °K. With falling temperature,

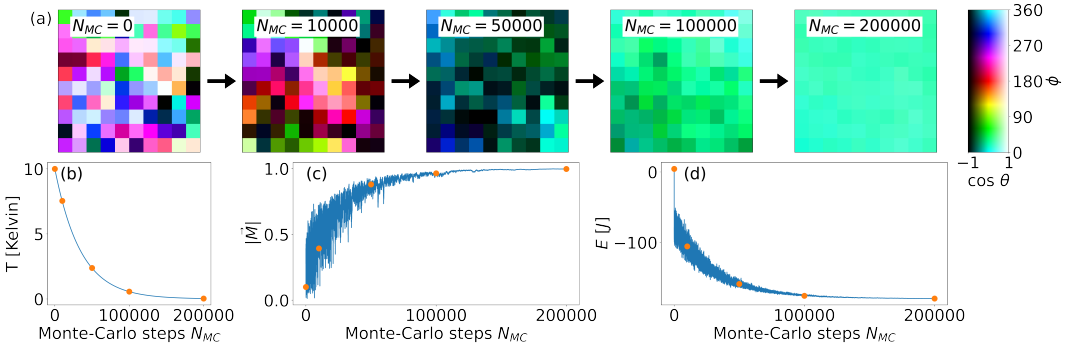

Figure 3.1: **Example of a Metropolis Monte-Carlo simulation.** The figures illustrate a Metropolis Monte-Carlo simulation of the 10×10 classical Heisenberg model given in Eq. (3.2) for $J = -1$ meV. **(a)** Visualization of the Heisenberg spins at different steps of the simulation. **(b)** Temperature T, **(c)** absolute value of the magnetization $|\vec{M}|$, and **(d)** total energy E in units of J with respect to the Monte-Carlo steps. The orange dots mark the simulation step at which the snapshots in (a) are taken.

the system approaches its ground state energy first quickly, but needs a lot of additional steps for the last remaining optimizations. In the fourth panel of Fig. 3.1 (a), the system is already almost fully ferromagnetic after 100,000 Monte-Carlo steps, but then still needs about 60,000 additional Monte-Carlo steps, to become fully ferromagnetic (within a small error margin). In the case of this example, the cause of this behavior can be explained as follows. Since the total energy only takes nearest neighbors into account, in the beginning a randomly chosen spin is likely in an unoptimized state compared to its neighbors. Therefore, there is a good chance of picking a spin that needs to be further optimized. In addition to that, the longer the simulation runs, the closer the system is to a fully ferromagnetic configuration. When changing a spin that is already almost parallelly aligned to its neighbors to a fully random spin from the whole unit sphere, it is very unlikely to pick a spin, such that the new spin is an improvement. The latter issue can be solved by restricting the spin updates to small changes at low temperatures when the system is already close to its ground state. We do this in all other Monte-Carlo simulations which use 3D spins throughout this thesis.

3.3 Adapting Metropolis Monte-Carlo to Different Models

Throughout the thesis, we adapt the Metropolis Monte-Carlo method to multiple different models to find their magnetic ground states. Here, we give a brief overview over these adaptations.

3.3.1 Classical Heisenberg Spins

For the case of classical Heisenberg spins, the Metropolis algorithm functions as described above. The total energy is calculated from a classical spin model which, in the later chapters, contains exchange interactions, Dzyaloshinskii–Moriya interaction (DMI) and 4-spin interactions up to the n-th neighbor. All of these interactions can be calculated by vector multiplications, and changes in total energy can be calculated by local changes. As each spin only interacts with other spins up to their n-th nearest neighbor, energy updates can be done by only calculating the energy change in the vicinity of the updated spin. This means that the computation time of the energy calculation itself does not scale with system size. Only the number of required updates increases with system size. This makes this model very efficient for large systems.

3.3.2 Tight-Binding Models

We also use the Metropolis Monte-Carlo algorithm to find the magnetic ground states of finite tight-binding models with quasi-classical spins like Eq. (3.1).
In these models, the spin interactions are mediated by itinerant electrons. To calculate the total energy, one needs to solve the complete eigenvalue problem (see Sec. 3.4 for details on the total energy calculation). As the complete Hamiltonian matrix needs to be solved, the energy updates cannot be done by just solving the vicinity of the changed spin. Therefore, the calculation time of each update scales heavily with the size of the system.

3.3.3 Monte-Carlo Method for Magnetic Ground States of Quasi-Infinite One-dimensional Isotropic Tight-Binding Models

While Metropolis Monte-Carlo methods are usually employed to identify ground states of finite magnetic systems, here, we develop a method to apply a Metropolis Monte-Carlo algorithm to effectively infinite tight-binding bulk systems. For this method the tight-binding Hamiltonian needs to be isotropic, i.e., invariant under a global rotation. If the 1D model is isotropic, we can limit all spins to a single rotational plane without loss of generality except for excluding spontaneous symmetry breaking into non-coplanar magnetic structures. Here, we choose the x-y-plane for a chain along the x-axis. Later, in Sec. 4.1, we show that this limitation is justified for our model with finite-size calculations that are not limited to a single plane, but produce only coplanar magnetic ground states. Using the model introduced in 3.1 with $\alpha = 0$, we consider N sites to be a unit cell, which gets repeated infinitely. On each site j of the unit cell, we employ a j-dependent spin basis rotation

$$R_{\Theta_j} = \begin{pmatrix} \cos(\Theta_j/2) & -\sin(\Theta_j/2) \\ \sin(\Theta_j/2) & \cos(\Theta_j/2) \end{pmatrix}, \tag{3.3}$$

representing a rotation with the angle Θ_j of the magnetization within the xy-plane, where Θ_j is the sum of relative angles along the chain up to the j-th site $\Theta_j = \sum_{n=1}^{j-1} \theta_n$ with the relative angle θ_n between the n-th and the $(n+1)$-th site of the unit cell. This rotation removes the spin direction from the onsite potential and adds a relative change in spin direction to the hopping terms between the j-th and $(j+1)$-th site. Carrying out the calculations, we start with the isotropic Hamiltonian

$$\begin{aligned} H = &\sum_{j}^{N} \vec{c}_j^{\,\dagger} \left(-J\tau_0(\vec{s}_j \cdot \vec{\sigma}) + (2t - \mu)\,\tau_z\sigma_0 + \Delta\tau_x\sigma_0\right) \vec{c}_j \\ &+ \sum_{\langle i,j \rangle}^{N-1} \vec{c}_i^{\,\dagger} \left(t\tau_z\sigma_0\right) \vec{c}_j + \text{h.c.} \end{aligned} \tag{3.4}$$

which is Eq. (3.1) for $\alpha = 0$ where we limit the spin to rotations around the y-axis without loss of generality. We can then write the spin on the j-th site as a rotation of a spin pointing in z-direction, where the angle of rotation is the sum of the relative angles leading up to the j-th site.

$$\vec{s}_j = R^{y,3D}_{\Theta_j} \begin{pmatrix} 0 \\ 0 \\ 1 \end{pmatrix} = \begin{pmatrix} \cos\Theta_j & 0 & \sin\Theta_j \\ 0 & 1 & 0 \\ -\sin\Theta_j & 0 & \cos\Theta_j \end{pmatrix} \cdot \begin{pmatrix} 0 \\ 0 \\ 1 \end{pmatrix} = \begin{pmatrix} \sin\Theta_j \\ 0 \\ \cos\Theta_j \end{pmatrix}, \tag{3.5}$$

where $\Theta_j = \sum_{n=1}^{j-1} \theta_n$ with the relative angle θ_n between the n-th and $(n+1)$-th site. We apply the site-dependent basis rotation

$$R_{\Theta_j} = \begin{pmatrix} \cos(\Theta_j/2) & -\sin(\Theta_j/2) \\ \sin(\Theta_j/2) & \cos(\Theta_j/2) \end{pmatrix}, \tag{3.6}$$

to the Hamiltonian. Because of

$$R^\dagger_{\Theta_j} \sigma_0 R_{\Theta_j} = \sigma_0, \tag{3.7}$$

the onsite chemical potential and superconducting terms are not affected by the rotation. With

$$R^\dagger_{\Theta_j} \left(\begin{pmatrix} \sin\Theta_j \\ 0 \\ \cos\Theta_j \end{pmatrix} \cdot \vec{\sigma} \right) R_{\Theta_j} = \sigma_z, \tag{3.8}$$

we get a site-independent magnetic onsite term. Finally, for the hopping term we get

$$R^\dagger_{\Theta_j} \sigma_0 R_{\Theta_{j+1}} = R^\dagger_{\sum_{n=1}^{j-1} \theta_n} R_{\sum_{n=1}^{j} \theta_n} = R_{\theta_j} \tag{3.9}$$

Putting everything together, the Hamiltonian in the rotated basis reads

$$\begin{aligned} H = &\sum_j^N \vec{c}_j^\dagger \left(-J\tau_0\sigma_z + (2t-\mu)\,\tau_z\sigma_0 + \Delta\tau_x\sigma_0 \right) \vec{c}_j \\ &+ \sum_{\langle i,j \rangle} \vec{c}_i^\dagger \left(t\tau_z \otimes R_{\theta_i} \right) \vec{c}_j. \end{aligned} \tag{3.10}$$

To calculate the total energy of the quasi-infinite chain, we assume infinitely repeating unit cells, find the k-dependent Hamiltonian using Eq. 2.28, calculate the k-dependent eigenvalues to find the bands, and then numerically integrate over all bands below $E_\mathrm{F} = 0$. As the magnetic behavior is now fully represented by relative rotation of neighboring spins, the Hamiltonian can represent spin systems via much smaller unit cells, as the onsite terms are translationally invariant. For example, let us assume a system where the ground state consists of spins with two alternating angles $\theta_1 = 2°$ and $\theta_2 = 5°$ between them. With the non-rotated Hamiltonian, one would need a unit cell of exactly $N = 2520$ sites or an integer multiple of that to fit a whole rotation into a unit cell, which is required to expand it to infinity. Additionally, one would need to check all possible sizes of unit cells to assure that there is no better combination of angles that does not fit in this unit cell. And even that would not account for irrational angles. Thus, one would need to run an infinite number of Monte-Carlo simulations to converge. Using the rotated basis, $N = 2$ is enough to represent any combination of two relative angles. To correctly identify the ground states, it is still necessary to run multiple simulations with different unit cell sizes N, but a handful of simulations can account for a much larger amount of possible states.

For our calculations in Chapter 4, we test unit cells of size $N = 1, 2, ..., 8$. We calculate the bands and sample 11000 k-points for the numerical integration to find the total energy. We then use a Metropolis Monte-Carlo method, see Sec. 3.2, to optimize the sets of relative angles θ_j for each size of unit cell. As a last step, we choose the unit cell with the lowest total energy per site. To account for numerical precision, we additionally check for repeating sequences in the chosen unit cell. For example, if a unit cell of $N = 4$ repeating angles is chosen with $\theta_1 \approx \theta_3$ and $\theta_2 \approx \theta_4$ within a tolerance of 0.015π, we reduce the system to a unit cell of $N = 2$ repeating angles.

3.4 Total Energy of a Superconducting Tight-Binding Model

To calculate the total energy of a superconducting tight-binding model, we start from a generic superconducting Hamiltonian in the BCS mean field description

$$H = \vec{c}^{\,\dagger} h \vec{c} + \vec{c} \Delta \vec{c} + \vec{c}^{\,\dagger} \Delta^{\dagger} \vec{c}^{\,\dagger}, \tag{3.11}$$

where h and Δ are hermitian matrices and $\vec{c} = (c_1, c_2, ..., c_N)^T$ is a vector containing all fermionic annihilation operators. In the Bogoliubov-de Gennes formalism, this is transformed to

$$H = \vec{p}^{\,\dagger} \begin{pmatrix} h/2 & \Delta/2 \\ \Delta^{\dagger}/2 & -h^*/2 \end{pmatrix} \vec{p} + \frac{1}{2} \operatorname{Tr}(h), \tag{3.12}$$

with $\vec{p} = (\vec{c}, \vec{c}^{\,\dagger})^T$ and the trace Tr.
We then use a unitary transformation U to diagonalize the Hamiltonian

$$\begin{aligned} H &= (U\vec{p})^{\dagger} U \begin{pmatrix} h/2 & \Delta/2 \\ \Delta^{\dagger}/2 & -h^*/2 \end{pmatrix} U^{\dagger} (U\vec{p}) + \frac{1}{2} \operatorname{Tr}(h) \\ &= \vec{d}^{\,\dagger} \begin{pmatrix} \epsilon/2 & 0 \\ 0 & -\epsilon/2 \end{pmatrix} \vec{d} + \frac{1}{2} \operatorname{Tr}(h), \end{aligned} \tag{3.13}$$

where ϵ is a matrix that contains all positive eigenvalues and $\vec{d} = (\vec{b}, \vec{b}^{\,\dagger})^T$ with the Bogoliubov quasiparticles $\vec{b}$. Using fermionic algebra, the Hamiltonian becomes

$$H = \vec{b}^{\,\dagger} \epsilon \vec{b} + \frac{1}{2} (\operatorname{Tr}(h) - \operatorname{Tr}(\epsilon)). \tag{3.14}$$

In this representation, all Bogoliubov quasiparticles have positive energies and the ground state energy is

$$E_{\text{total}} = \sum_i \frac{\epsilon_i - \mu}{2}. \tag{3.15}$$

3.5 Analytical Eigenvalues for the Case of Harmonic Spirals

Investigating the system introduced in Sec. 3.1 for the case of harmonic spirals, i.e., spirals with a fixed rotational angle θ between all nearest neighbors along the chain, we can compute the analytical energy eigenvalues. Using the Hamiltonian with a rotated spin basis from Eq. (3.10) for the case $N = 1$, and the method to find the k-dependent Hamiltonian $H(k)$ from Eq. (2.28), we can construct the k-space Hamiltonian matrix $\tilde{h}(k)$ for a harmonic spiral

$$\tilde{h}(k) = \begin{pmatrix} b - J & \mathrm{i}c & \Delta & 0 \\ -\mathrm{i}c & b + J & 0 & \Delta \\ \Delta & 0 & -b - J & -\mathrm{i}c \\ 0 & \Delta & \mathrm{i}c & -b - J \end{pmatrix}, \tag{3.16}$$

$$\text{with } b = 2t - \mu - 2\cos(\theta/2)\cos(k)$$
$$\text{and } \mathrm{i}c = 2\mathrm{i}t \cdot \sin(\theta/2)\sin(k).$$

From this, we can calculate the k-dependent eigenvalues, i.e., the bands

$$\lambda_{1,2,3,4}(k) = \pm\sqrt{b^2 + c^2 + \Delta^2 + J^2 \pm 2\sqrt{b^2c^2 + b^2J^2 + \Delta^2J^2}}. \tag{3.17}$$

We later use these eigenvalues to efficiently calculate the total energy of harmonic bulk spiral systems by integrating over the bands below the Fermi edge.

3.6 Majorana Number for Infinite Systems

A 1D material in class D (time-reversal symmetry being broken by the magnetic moments and the particle-hole symmetry squaring to +1) has a $\mathbb{Z}_2$ topological invariant [132]. We employ the Majorana number M [5] for the topological

classification of infinitely long chains, which is

$$M = \mathrm{sgn}(\mathrm{Pf}(\tilde{H}(k=0))) \cdot \mathrm{sgn}(\mathrm{Pf}(\tilde{H}(k=\pi))), \tag{3.18}$$

with the Pfaffian Pf and the k-space Hamiltonian $\tilde{H}$ in a Majorana basis. Assuming the basis $\vec{c}_j = (c_{j\uparrow}, c_{j\downarrow}, c_{j\downarrow}^\dagger, -c_{j\uparrow}^\dagger)$, which we use throughout this thesis, the Hamiltonian is brought into a Majorana basis via the unitary transformation $\tilde{H} = U^\dagger H U$ with

$$U = \frac{1}{\sqrt{2}} \begin{pmatrix} 1 & 0 & 0 & i \\ 0 & 1 & i & 0 \\ 0 & 1 & -i & 0 \\ -1 & 0 & 0 & i \end{pmatrix}. \tag{3.19}$$

The system is topologically non-trivial when it has a non-zero spectral gap and $M = -1$.

3.7 Majorana Number for Finite Systems

As the standard Majorana number is calculated through k-space, it can only be calculated for translationally invariant systems, for which one can perform a Fourier transform to reach k-space. When one wants to find out if a given finite system without translation invariance hosts Majoranas, an alternative approach is needed. Here, we explain such a method, following Ref. [139].
To calculate the topological number of finite-size chains, we use the reflection matrix r which is defined as the matrix that connects an incoming mode at zero energy from an infinite lead with the reflected outgoing mode. The lead is defined by the Hamiltonian

$$H_{\mathrm{lead}} = \sum_{\langle i,j \rangle} \vec{c}_i^{\,\dagger} \left(t \tau_z \sigma_0\right) \vec{c}_j, \tag{3.20}$$

and connects to the first site of the chain via $\vec{c}_{\mathrm{lead}}^{\,\dagger} \left(t \tau_z \sigma_0\right) c_{\mathrm{chain,j=1}}$ where the symbols have the same meaning as in Sec. 3.1. The topological number is then

calculated as

$$Q = \mathrm{sgn}(\det(r)) \tag{3.21}$$

in a Majorana basis by using the same unitary transformation as in Eq. (3.19). This approach converges to the Majorana number as defined by Kitaev for clean infinite systems, but can also be applied to finite systems with impurities [139].

3.8 Scanning Tunneling Microscopy

In this section, we explain the concepts behind scanning tunneling microscopy (STM) and scanning tunneling spectroscopy (STS). We focus on explaining the basic principles needed to understand the results presented in Chapters 6 and 7, rather than details of experimental realization.

Scanning tunneling microscopy (STM) is a measurement technique that utilizes the tunneling effect to measure surfaces and their electronic properties at subatomic resolution [140, 141]. The first STM was invented by Binnig, Rohrer et al. [141], for which Binnig and Rohrer received the Nobel Prize in 1986 [142]. In an STM, a tip and a sample are separated by a small vacuum gap of a few Å. When a bias voltage V on the order of mV to V is applied between the tip and the sample, a tunneling current I on the order of pA to several nA flows through the vacuum barrier. The tunneling through a vacuum decays exponentially with the distance, which allows for a precise measurement of relative distances between tip and sample. The tip can be moved in all three spatial dimensions with piezoelectric elements, i.e., by using materials which deform when a voltage is applied to them due to the reverse piezoelectric effect. With this, the tip can be moved across the surface in a scanning manner to create a topography of the surface. The resolution in the xy-plane is dependent on the sharpness of the tip, which ideally has a single atom apex. In the vertical direction, subatomic resolution is obtained due to the exponential decay of I.

To model the tunneling current, following the approach of J. Bardeen [143], we assume that the eigenstates of the tip and the sample are the solutions to their individual Schrödinger equations. Their eigenstates are coupled by a

tunneling junction, which can be understood as a weak perturbation. With Fermi's golden rule, the transition rates between tip and sample can be calculated and the matrix elements can be obtained with a perturbative approach. Additionally, we simplify the tip apex to a spherical s-orbital as suggested by Tersoff and Hamann [144]. With this, we receive the tunneling current

$$I(V,T) = \frac{4\pi e}{\hbar} \int_{-\infty}^{+\infty} \rho_{\text{sample}}(E - E_{\text{F}}, x, y, z)\rho_{\text{tip}}(E - E_{\text{F}} + e \cdot V)\mathcal{T}(E, V, d) \cdot \big[f(E - E_{\text{F}} + e \cdot V, T) - f(E - E_{\text{F}}, T)\big]\mathrm{d}E, \tag{3.22}$$

where ρ_{tip} is the density of states at the tip apex, ρ_{sample} is the energy-dependent local density of states (LDOS) of the sample in the vacuum at the tip location, T is the temperature, $\mathcal{T}$ is the transmission coefficient, and $f(E,T) = \frac{1}{1+e^{E/k_B T}}$ is the Fermi-Dirac distribution with the Boltzmann constant k_B, accounting for the thermal population of fermionic states. From this equation, we can see that the tunneling current scales with the amount of available states in the tip and the sample to tunnel into. The term $\big[f(E - E_{\text{F}} + e \cdot V, T) - f(E - E_{\text{F}}, T)\big]$ accounts for the fact that tunneling is only possible between an occupied and an unoccupied state. A shift in the bias voltage V causes a relative shift in the occupation numbers and energy-dependent LDOS between tip and sample.
Using a few realistic assumptions, Eq. (3.22) can be heavily simplified. When the bias voltage V is small compared to the work functions of tip and sample, the transmission coefficient $\mathcal{T}(E, V, d)$ becomes independent of E and V, turning it into a constant within the integration. For metallic tips, it is valid to assume that ρ_{tip} is constant for small energy ranges around E_{F}. Additionally, for low temperature experiments, we can approximate low $T \approx 0$ °K. This simplifies the proportionality of the tunneling current to

$$I(V) \propto \int_{E_{\text{F}}}^{E_{\text{F}}+e\cdot V} \rho_{\text{sample}}(E)\mathrm{d}E. \tag{3.23}$$

Thus, the tunneling current is approximately proportional to the vacuum density of states of the sample integrated from E_{F} to $E_{\text{F}} + e \cdot V$.

Constant-Current and Constant-Height Mode

When scanning in the xy-plane, STMs can switch between two main measuring modes, which come with their own advantages and disadvantages. These two modes are the constant-current and the constant-height modes.
In constant-current mode, a feedback loop between the piezoelectric element in z-direction and the tunneling current is used to automatically adjust the distance to the tip, so that the tunneling current is kept constant. Thus, when moving the tip in the xy-plane, the height of the tip is adjusted to the topography and the LDOS. The relative tip height is measured to create an image of the surface.
In constant-height mode, the tip is fixed in z-direction and moved only in x- and y-direction. Thus, the tunneling current changes dependent on the LDOS and topography. This mode is particularly useful when investigating atomically flat surfaces, as it avoids artifacts introduced by the feedback loop of the constant-current mode. But it is unreliable on surfaces with step edges, as the resolution and tip distance can only be adjusted to one of the terraces in constant-height mode. Additionally, in constant-height-mode the tip can potentially crash into higher surface features.

Atom Manipulation

An STM can also be used as a tool to move adatoms on the surface. There are various forces acting between the tip apex and the adatoms on the sample surface. By bringing the tip very close to the sample, a semi-stable bond between tip and adatom can be created. Then, moving the tip in the xy-plane can push or drag the adatom if the bond is strong enough. When the tip is retracted from the surface in z-direction, the bond is broken, leaving the adatom at the new position. This technique is called *lateral manipulation* and was first demonstrated by Eigler and Schweizer in 1990 [145].
An alternative technique is called *vertical manipulation* [146, 147]. Here, the tip is brought into close proximity with the adatom. Then a short voltage pulse is applied, which causes the adatom to transfer from the surface to the tip. The tip is then moved to a new position, where the adatom is transferred

back to the surface with another voltage pulse. It should be noted that, for any manipulation technique, the adatom will only remain at energetically favorable adsorption sites.
Atom manipulation allows to build precise atomic structures and is widely used when investigating atom-scale nanostructures [4, 83, 148–154] or atomic chains [3, 17, 155–161].

Scanning Tunneling Spectroscopy

Scanning tunneling spectroscopy is a technique that allows to access the energy dependence of the LDOS directly with an STM.
The tunneling current I is related to the LDOS integrated from E_F to $E_\mathrm{F}+e\cdot V$. In turn, the differential tunneling conductance $\frac{\mathrm{d}I}{\mathrm{d}V}$ is related to the energy-dependent LDOS. We differentiate Eq. (3.22) by the bias voltage V, assuming constant-height mode and that $\mathcal{T}(E,V,d)$ is a constant,

$$\begin{aligned}\frac{\mathrm{d}I}{\mathrm{d}V}(V,T) \propto &\int_{-\infty}^{+\infty} \rho_\mathrm{sample}(E)\frac{\partial\rho_\mathrm{tip}(E+e\cdot V)}{\partial V}\big[f(E+e\cdot V,T)-f(E,T)\big]\mathrm{d}E \\ &+\int_{-\infty}^{+\infty}\rho_\mathrm{sample}(E)\rho_\mathrm{tip}(E+e\cdot V)\frac{\partial f(E+e\cdot V,T)}{\partial V}\mathrm{d}E.\end{aligned} \tag{3.24}$$

Here, we set $E_\mathrm{F}=0$ for simplicity. If needed, it can be reintroduced by setting $E\mapsto E-E_\mathrm{F}$. As before, we assume ρ_tip to be constant around $E_\mathrm{F}=0$ for a few meV for metallic tips, and we assume very low temperatures $T\approx 0$ °K, reaching the simplified proportionality of the differential tunneling conductance

$$\frac{\mathrm{d}I}{\mathrm{d}V}(V)\propto\rho_\mathrm{sample}(E=e\cdot V). \tag{3.25}$$

Thus, the energy dependence of the sample LDOS $\rho_\mathrm{sample}(E)$ is directly accessible through the bias voltage dependence of the differential tunneling conductance. The main limiting factor for the resolution of STS is the finite temperature. As thermal tunneling processes cause a broadening of the Fermi-Dirac distribution, the $\frac{\mathrm{d}I}{\mathrm{d}V}$ curves get smeared out. For a temperature of $T\approx 0.32$ °K (the temperature used in the experiments described in Chapters 6 and 7), the resolution is limited to 85 μeV.

STS with Superconducting Tips

The precision of STS can be significantly improved by using superconducting tips. Looking at Eq. (3.24), if $\rho_{\text{tip}}(E)$ was a Dirac delta function, we could measure ρ_{sample} with optimal energy resolution, independent of the temperature T. In that case, only tunneling from a single discrete tip state to the sample and vice versa would be possible. The coherence peaks of a superconductor can be extremely sharp, to the point where they are a good approximation to this idea.

When the sample and the tip both are superconducting, a few details need to be considered for analyzing the measurement data. At $e \cdot V = \pm(\Delta_{\text{tip}} + \Delta_{\text{sample}})$ a massive conductance channel occurs due to the tunneling from one occupied coherence peak to the other unoccupied coherence peak. For finite temperatures, another peak can be measured at $e \cdot V = \pm(\Delta_{\text{tip}} - \Delta_{\text{sample}})$, because thermally excited particles are in the coherence peak that would be unoccupied at zero temperature [162, 163]. The latter effect is not visible at very low temperatures, however. For small distances between tip and sample, direct tunneling of Cooper pairs is also possible, which causes peaks at zero bias voltage. This effect is known as Josephson tunneling [164–167]. Electrons can also tunnel into the superconductor and be reflected as a hole, which leads to peaks at an energy below $e \cdot V = \pm(\Delta_{\text{tip}} + \Delta_{\text{sample}})$ being known as Andreev reflection [162, 163, 168, 169]. However, both of these effects can be avoided by measuring $\frac{\mathrm{d}I}{\mathrm{d}V}$ spectra at sufficiently large tunneling gap resistances, i.e., sufficiently large distances between tip and sample.

Chapter 4

Magnetic Ground States and Topological Phases of One-Dimensional Chains

In this chapter, we investigate the electronic topological phases of one-dimensional chains of atoms with local magnetic moments, proximity-induced superconductivity, and self-consistently found magnetic ground states. For this, we employ the tight-binding model

$$\begin{aligned} H = &\sum_{j=1}^{L} \vec{c}_j^{\,\dagger}\big[- J\tau_0 \vec{s}_j \cdot \vec{\sigma} + (2t-\mu)\tau_z\sigma_0 + \Delta\tau_x\sigma_0\big]\vec{c}_j \\ &+ \sum_{\langle i,j\rangle_1} \vec{c}_i^{\,\dagger}\big[t\tau_z\sigma_0 + \mathrm{i}\alpha\tau_z\sigma_y\big]\vec{c}_j + \mathrm{h.c.}, \end{aligned} \tag{4.1}$$

which has been introduced in detail in Sec. 3.1. Large parts of the results presented in this section are published in the article [1]

> Jannis Neuhaus-Steinmetz, Elena Y. Vedmedenko, Thore Posske, and Roland Wiesendanger
>
> *Complex magnetic ground states and topological electronic phases of atomic spin chains on superconductors*
>
> Phys. Rev. B **105**, 165415 – Published 13 April, 2022
>
>

We start by calculating the ground state of a number of finite-size trial configurations in Sec. 4.1 and use the information gathered from those as a starting point to determine the magnetic phases of quasi-infinite chains in Sec. 4.2. We

first investigate the magnetic phases with vanishing superconductivity. Then, we slightly increase the superconducting order parameter, enough to open a small spectral gap, but not enough to significantly affect the magnetic states. From this, we calculate the Majorana number. Following that, further increasing the superconducting order parameter, we investigate how increased superconductivity affects the magnetic phases and in turn changes the topological phases. As physical systems in many STM experiments are often finite and small, e.g., on the order of tens of atoms [3, 17–19], we choose to also investigate the magnetic ground states and resulting electronic topology under increased superconductivity of short finite chains in Sec. 4.3. Following up on these two sections, we compare the results for finite and infinite chains in Sec. 4.4. Additionally, in Sec. 4.5, we introduce a new approximative method to identify magnetic ground states of tight-binding models by fitting a classical spin model. We reproduce some of the results presented in this chapter with this new method to investigate the reliability of our approximative method and discuss its advantages and disadvantages. Finally, in Sec. 4.6, we summarize our results on the one-dimensional systems and provide an outlook for future research directions.

4.1 Trial Configurations from Finite Chains

We begin by identifying finite trial configurations using a Metropolis Monte-Carlo algorithm (see Sec. 3.2 and Sec. 3.3.2) to gain a better understanding of the possible magnetic states of this system before determining the magnetic phases.[1] We find that all ground states are invariant under a global rotation, i.e., rotating all spins around the same axis by the same angle simultaneously will result in no changes for the electronic system and thus no changes in total energy. A few examples for the magnetic grounds states are shown in Fig. 4.1. Besides typical collinear states like ferromagnetic and anti-ferromagnetic states,

[1] To achieve convergence we use 100,000 Monte-Carlo steps (MCS) in the first part of the cooling with a logarithmic temperature function, then 50,000 MCS further cooling the system with only small changes to the spins and finally 10,000 MCS at zero temperature with only small changes (see Sec. 3.2).

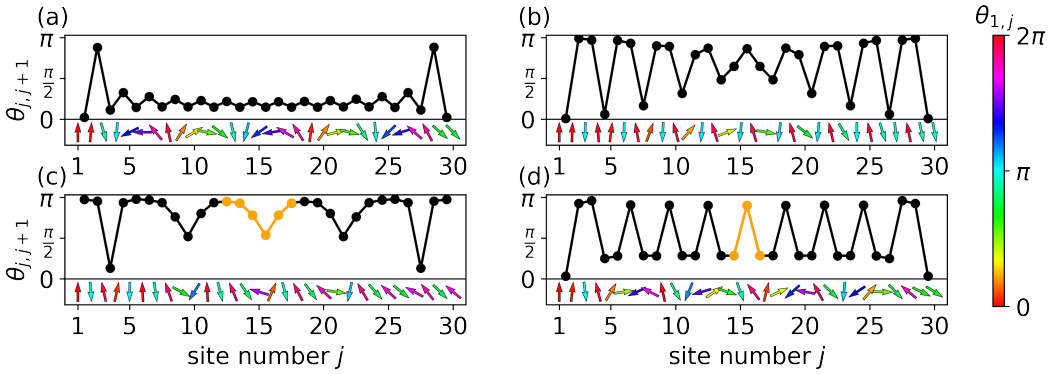

Figure 4.1: **Ground state spin configurations of finite-size chains.** Relative angles between neighboring spins along the chain for representative examples of ground states of finite-size chains with open boundary conditions with $\Delta = 0$ and $L = 30$. The periodic parts that can be used as a unit cell are marked in orange. The insets show a 2D projection of the spins. The color denotes the relative angle between the j-th spin and the first spin $\theta_{1,j}$. **(a)** $J = 1.4\,t$, $\mu = 0.5\,t$, **(b)** $J = 0.2\,t$, $\mu = 1.0\,t$, **(c)** $J = 0.6\,t$, $\mu = 1.4\,t$, **(d)** $J = 1.6\,t$, $\mu = 0.6\,t$.

we also find more exotic collinear states: In the transition region between the ferromagnetic and anti-ferromagnetic phase, we find structures that follow patterns like ↑↑↓↓, ↑↑↑↓↓↓ or ↑↑↑↓. The shorthand notation ↑↑↑↓ describes a ground state in which a magnetic unit cell can be formed by three parallelly aligned spins followed by one spin anti-parallel to the previous three. We also find structures that host configurations close to harmonic spin spirals[2] in the inner part of the chain and strong boundary effects in the form of almost collinear spins at the ends of the chain, e.g., Fig. 4.1 (a). There are also states which are completely dominated by boundary effects, e.g, Fig. 4.1 (b). Additionally, we find structures that can be described by a repeating sequence of relative angles, e.g, Fig. 4.1 (c,d). Furthermore, we find that all ground states are coplanar.

[2]A harmonic spin spiral is a spin spiral which can be described by the repetition of a single relative angle

4.2 Infinite Chains

Phase Diagram of Infinite Chains

Here, we investigate the magnetic phase diagram of the quasi-infinite bulk chain. To determine the magnetic phase for a given set of parameters, we employ multiple methods of calculating the ideal magnetic configuration and compare the total energies of each. Let us start by providing an overview over the employed methods.

For all methods, the total energy is calculated in k-space using 11000 k-points for the numerical integration, which is equivalent to a periodic chain with 11000 atoms. First, we calculate the total energy for all collinear unit cells identified from the finite trial configurations. Second, we determine the energetically most favorable harmonic spin spiral by integrating over the analytically found eigenvalues (see Sec. 3.5), trying all θ in steps of $\Delta\theta = \frac{\pi}{3600}$. Third, we employ a Metropolis Monte-Carlo method based on unit-cells of repeating angles as described in Sec. 3.3.3 to identify non-harmonic non-collinear phases.[3] As a last step, we compare the total energies of the ground states identified by these three methods and pick the one with the lowest energy per site. The main reason for using these three methods here instead of fully relying on the third is that the first two are computationally faster allowing for a higher resolution.

The identified magnetic phases are shown in Fig. 4.2. We find that most of the phase space is either ferromagnetic (A) or anti-ferromagnetic (B). The system is anti-ferromagnetic for all $J \gtrsim -\frac{4}{3}\mu + \frac{8}{3}t$. The magnetic phase space is mirrored at $\mu = 2t$, which is why it is only shown for $\mu < 2t$ here. For $J < 3.0\,t$, we find a rich and complex magnetic phase diagram between the ferromagnetic (FM) and anti-ferromagnetic (AFM) phases. Within this transition region, for $J < 2.0\,t$, we find non-collinear harmonic spin-spirals (C) as the background, which is interrupted by two other phases. First, there is an $\uparrow\uparrow\downarrow\downarrow$-phase around $\mu = 0.6\,t$ (D). Second, between the $\uparrow\uparrow\downarrow\downarrow$-phase and the AFM phase, we find

[3] For this method we use 10,000 MCS in the first part of the cooling with a logarithmic temperature function, and then 1,000 MCS further cooling the system with only small changes to the relative angles.

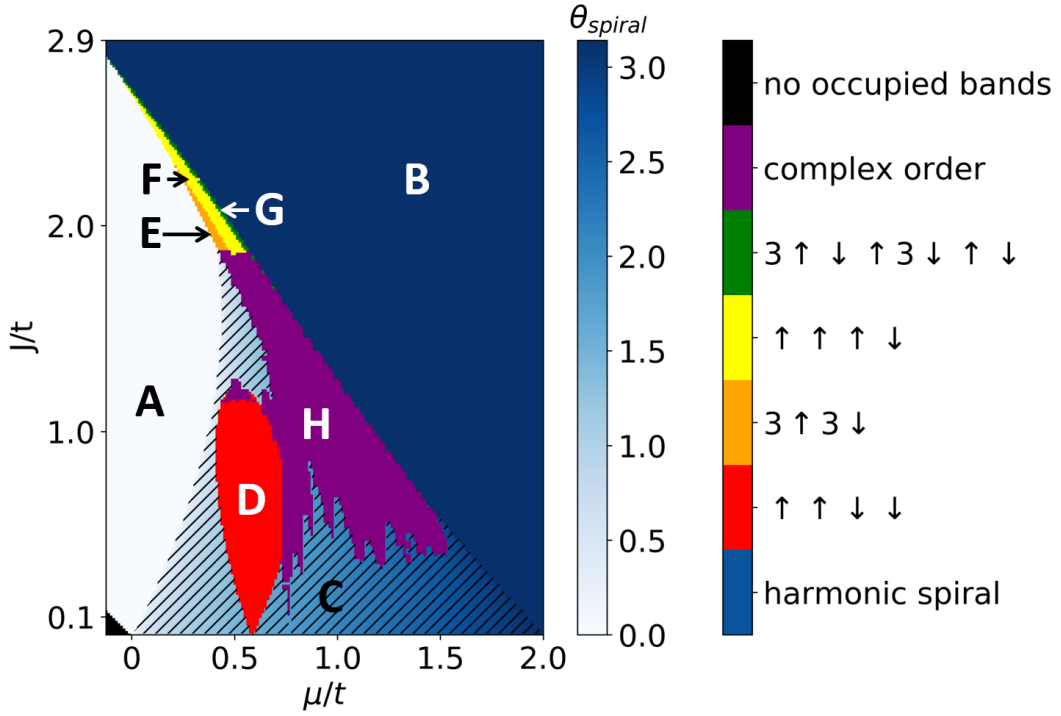

Figure 4.2: **Magnetic phases for vanishing superconductivity** in dependence on J and μ for infinite chains. The shades from white to dark blue denote a spiral, where color saturation describes the spiral pitch θ_{spiral}, see left color bar. The right color bar labels magnetic phases. The shortened notation $3\uparrow$ refers to $\uparrow\uparrow\uparrow$. In the hatched area, we find a negative Majorana number $M = -1$ and an opening of a spectral gap for infinitesimal superconductivity, calculated with $\Delta = 0.001\,t$, while the other regions remain gapless or have a positive Majorana number $M = +1$.

a phase that is characterized by repeating sequences of relative angles (H) like those found in the trial configurations. When compared to the energy of the most favorable harmonic spiral for the respective parameter set, the total energy of those states is lower by a value between 0.002 J per atom (close to the $\uparrow\uparrow\downarrow\downarrow$-phase) and 0.03 J per atom (close to the AFM phase). For $J > 2.0\,t$, we find complex collinear structures, namely $\uparrow\uparrow\uparrow\downarrow\downarrow\downarrow$ (E), $\uparrow\uparrow\uparrow\downarrow$ (F) and $\uparrow\uparrow\uparrow\downarrow\uparrow\downarrow\downarrow\downarrow\uparrow\downarrow$ (G). The latter is an extremely narrow phase, which leads to speculations that there might exist even more complex phases which one could only identify with a higher resolution of the parameter space. The total energy of those structures

is on average 0.005 J per atom lower than the most favorable harmonic spiral, which includes FM and AFM as possible harmonic spirals. Note that the ↑↑↓↓- and ↑↑↑↓↓↓-phase as well as the harmonic phases have been previously reported by Minami and Kawamura [28]. Lastly, for $\mu < -|J|$, no bands are occupied, which is why that region is blacked out.

Adding Superconductivity as a Small Perturbation

To investigate, which of the magnetic phases shown in Fig. 4.2 coincide with non-trivial electronic topological phases, we increase the superconducting order parameter to $\Delta = 0.001\,t$, which is enough to open a small spectral gap, but does not affect the magnetic ground states in a significant manner. The system at hand is a class D material with time-reversal symmetry broken by magnetic moments and a particle-hole symmetry which squares to +1 [132]. Thus, this system has a $\mathbb{Z}_2$-invariant. To determine whether a phase is topologically trivial or non-trivial, we employ the Majorana number M [5] introduced in Sec. 3.6. The system is non-trivial if and only if $M = -1$ while the spectral gap is open. The hatched area in Fig. 4.2 shows where $M = -1$ and a spectral gap is open. With this, we can conclude that the electronic topology is only non-trivial when the magnetic ground state is a non-collinear harmonic spiral.

Further Increasing Superconductivity

We further increase the superconducting order parameter Δ, using the method introduced in Sec. 3.3.3 to investigate how the magnetic phases change under enhanced superconductivity. To gain a better understanding of the magnetic ground states, we introduce three measures to describe it. First, we introduce the periodicity, which is corresponding to the size of the unit cell L_{cell} that achieved the lowest total energy. To account for numerical precision, we check for repeating sequences and allow a tolerance of 0.015π. Second, we introduce the number of collinear spins N_{col} in a unit cell, which is the number of pairs of spins in a unit cell with relative angles equal to 0 or π. Here, we consider an angle to be collinear when $|\cos(\theta)| > 0.995$ to account for numerical precision. Third, we introduce a parameter that measures how much a given structure

deviates from a harmonic spin spiral. This parameter is the average of the absolute difference of neighboring relative angles θ_i

$$\theta_{\text{change}} = \frac{1}{L_{\text{cell}} - 1} \sum_{\langle i,j \rangle} |\theta_i - \theta_j|, \tag{4.2}$$

where we sum over neighboring relative angles assuming periodic boundaries. To visualize this parameter, one can follow the relative angles given in Fig. 4.1, note the difference between each point, sum their absolute values and then normalize for a given chain length L. A harmonic spin spiral, i.e., a chain where all relative angles θ_i are the same, would result in $\theta_{\text{change}} = 0$.

These three measures along with the product of the band gap and the Majorana number M (see Sec. 3.6 on how M is calculated) are shown in Fig. 4.3 for increasing Δ. The size of the complex order region, which is defined by a periodicity of angles greater than 1 and non-collinear neighbors, decreases with increasing Δ. At $\Delta = 0.4\,t$, it only remains at the transition from the ferromagnetic to the anti-ferromagnetic phase. Thus, larger parts of the phase space can be represented by harmonic spirals. The $\uparrow\uparrow\downarrow\downarrow$-phase can be identified by $\theta_{\text{change}} = \pi$. It shrinks for increasing Δ and vanishes between $\Delta = 0.2\,t$ and $\Delta = 0.3\,t$. We find that the quotient of N_{col} and the periodicity is almost always 0 or 1. Thus, for infinite chains either all or no angles in a unit cell are collinear. The electronic system can only be topologically non-trivial when the magnetic state is neither collinear nor of complex order. As both of these states take a lower portion of the phase space for increasing Δ, the non-trivial region grows until its size settles at around $\Delta \approx 0.3\,t$. Further increasing Δ mostly deforms the topological phase and moves it towards larger J, as for $J < \Delta$ the system is always trivial.

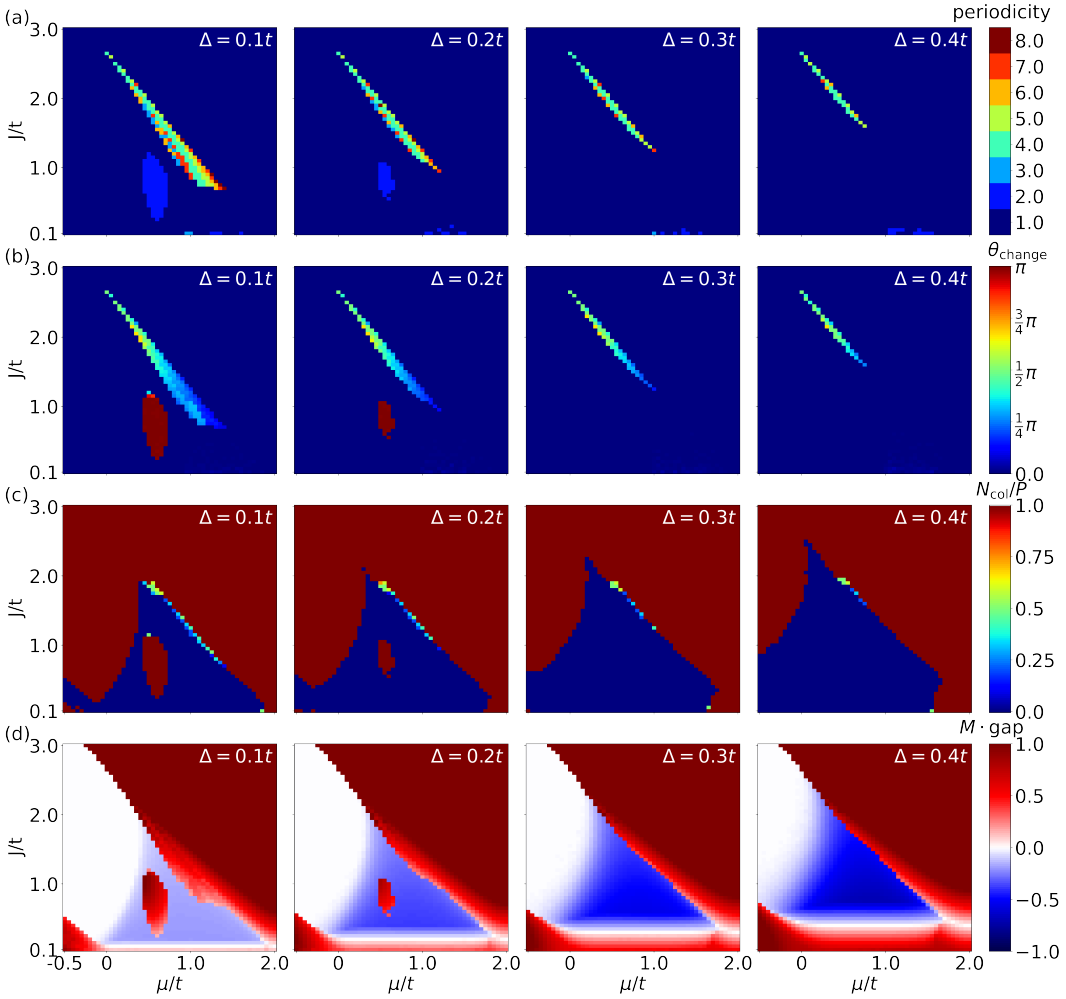

Figure 4.3: **Magnetic properties and topological phases of infinite chains for non-vanishing superconducting order parameters** $\Delta > 0$ with respect to J and μ. The chosen values of Δ are noted in the panels. **(a)** Periodicity, **(b)** θ_{change}, **(c)** Percentage of collinear spins in a magnetic unit cell N_{col}/P, **(d)** Majorana number multiplied with the band gap. Negative values (blue) indicate that the system is in a non-trivial state.

4.3 Finite Chains

Going back to finite chains, we first adapt the measures for the number of collinear pairs of spins and the change of the relative angle to finite chains. First, we change the number of collinear spins N_{col} in a unit cell to the number of collinearly aligned pairs of neighbors along a given chain. Here, we consider two spins to be collinear when $|\vec{s}_i \cdot \vec{s}_j| > 0.995$ to account for numerical precision. Second, θ_{change} is calculated along the finite chain for neighboring spins $\vec{s}_i$, $\vec{s}_{i+1}$, $\vec{s}_{i+2}$ by

$$\theta_{\text{change}} = \frac{1}{L-2} \sum_{j=1}^{L-1} |\arccos(\vec{s}_j \cdot \vec{s}_{j+1}) - \arccos(\vec{s}_{j+1} \cdot \vec{s}_{j+2})|. \tag{4.3}$$

Fig. 4.4 shows N_{col} and θ_{change} for a chain of length $L = 40$ with open boundary conditions along with the topological number calculated by the determinant of the reflection matrix r as introduced in Sec. 3.7. Here, we show the determinant instead of its sign, because numerical precision causes the sign to become almost random when $\det(r) \approx 0$. We consider the system to be topologically trivial when $\det(r) \approx 0$ because this indicates that the spectral gap is closed, since the phase transition happens when $\det(r)$ crosses zero and is associated with a gap closing. For small Δ, large parts of the phase space between the FM and AFM phases are non-harmonic, even though they are harmonic in the infinite chain. Most states have at least some collinear neighboring spins which are located at the ends of the chain. The exotic collinear phases, as found in the infinite case, persist with small changes to the shape of their phases. In Fig. 4.4, they can be identified by having a maximal $N_{\text{col}} = 39$ with a non-zero θ_{change}. Further increasing Δ causes larger parts of the parameter space to become harmonic or show at least a smaller θ_{change}. The amount of collinear spins at the ends of the chains is also significantly reduced, as we find that enhanced superconductivity lowers the relevance of boundary effects. We also find that the exotic collinear states vanish with increasing superconductivity. The $\uparrow\uparrow\downarrow\downarrow$-phase vanishes around $\Delta \gtrsim 0.35\,t$, and the $\uparrow\uparrow\uparrow\downarrow$- and $\uparrow\uparrow\uparrow\downarrow\downarrow\downarrow$-phases vanish at $\Delta \gtrsim 1.5\,t$. Concerning the electronic topological phase, we find that

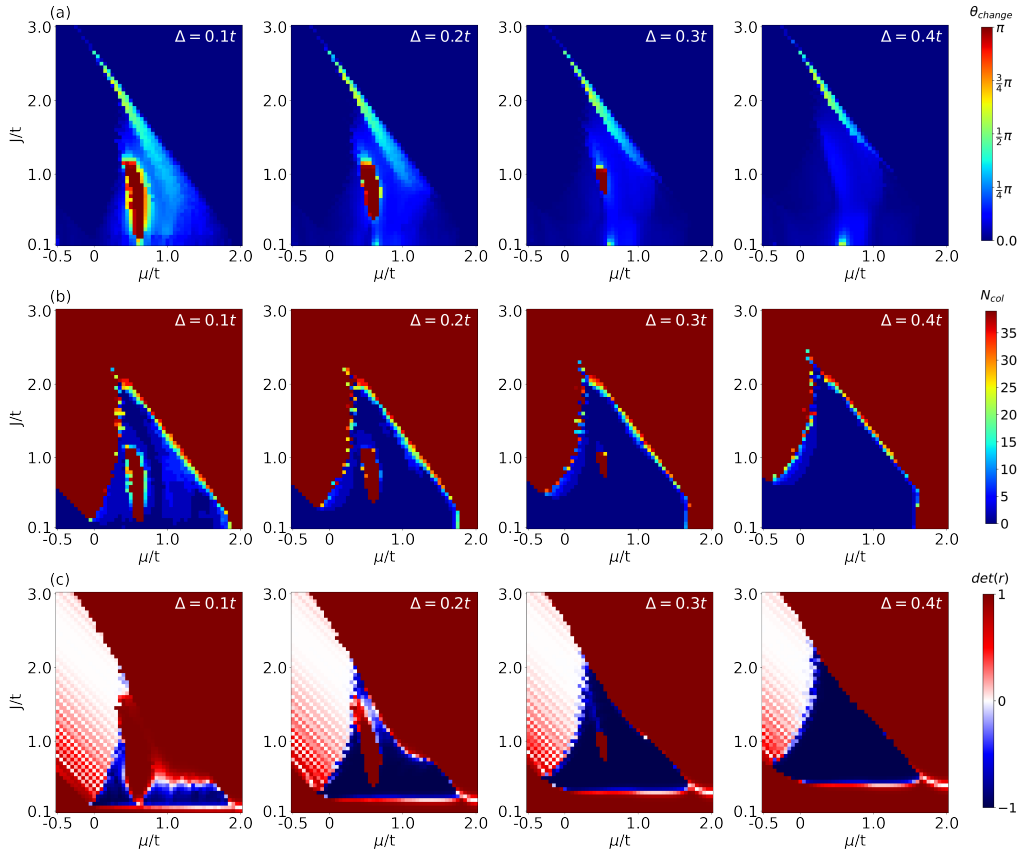

Figure 4.4: **Magnetic properties and topological phases of finite-size chains for non-vanishing superconducting order parameters** $\Delta > 0$ with respect to J and μ, calculated for a chain of length $L = 40$ with open boundary conditions. The chosen values of Δ are noted in the panels. **(a)** θ_{change}. **(b)** Number of collinear spins N_{col}. **(c)** The determinant of the reflection matrix $\det(r)$ in the magnetic ground state. Negative values (blue) indicate that the system is in a non-trivial state.

for $\Delta = 0.1\,t$ large parts of the parameter space are trivial in the finite system even though they are non-trivial in the infinite system. This can be attributed to the boundary effects. While pure boundary effects usually do not prevent the formation of Majoranas, here, they cause such a significant change to the magnetic structure, even in the inner parts of the chains, that chains of the given length ($L = 40$) are pushed into the trivial regime. Spot checks show that this effect diminishes with increased system size. Thus, the topological

phase space for the finite system eventually approaches that of the infinite system for long chains. For further increased Δ, the magnetic boundary effects appear to have a weaker butterfly effect on the rest of the magnetic structure. Fig. 4.5 (a,b) shows two examples of ground states for the same J and μ, but different Δ. For infinitely long chains (see Sec. 4.2), we find harmonic spirals as the magnetic ground state for both parameter sets. For chains of length $L = 40$, in the case of $\Delta = 0.2\,t$, the inner part is a harmonic spiral despite hosting a few collinear aligned spins at the ends of the chains. In a structure like this, the Majoranas are pushed into the chain and smeared out, but still occur. For $\Delta = 0.1\,t$, the boundary condition has a ripple effect causing the magnetic structure to strongly deviate from the structure found for continuum chains, ultimately causing a magnetic structure that does not host Majoranas anymore. For increasing chain lengths, this ripple effect decreases. In the example given in Fig. 4.5 (a,c,d), the inner parts of the chain are similar enough to a harmonic spiral state for $L = 60$ and $L = 80$ to host Majoranas, but not for $L = 40$. We confirmed for up to $L = 100$ with spot checks that the inner part of the chain does not become harmonic when the calculations for infinite chains predict a non-harmonic ground state, see Fig. 4.5 (e). It is also known that in these kinds of systems Majoranas appear only with non-collinear spin structures or non-vanishing Rashba spin-orbit coupling. It should be noted though that the absence of collinear spins does not guarantee that the electronic system is non-trivial.

When increasing Δ further, a larger part of the parameter space becomes topologically non-trivial as the $\uparrow\uparrow\downarrow\downarrow$-state vanishes and the weakened butterfly effect from the boundary conditions allows for more harmonic spirals. Around $\Delta \approx 0.35\,t$, the size of the non-trivial portion of the parameter space is not significantly changing further for further increases in Δ. Further increasing Δ mostly deforms the topological phase and shifts it towards larger J, as for $J < \Delta$ the system is always trivial, which is in agreement with our results for infinitely long chains.

Overall, these results suggest that systems with large superconducting order parameters might naturally stabilize magnetic structures that support Majorana-zero-modes better than systems with a small spectral gap. Our results also

suggest that in some systems short chains might not lead to the magnetic structures required for Majoranas, whereas longer chains could.

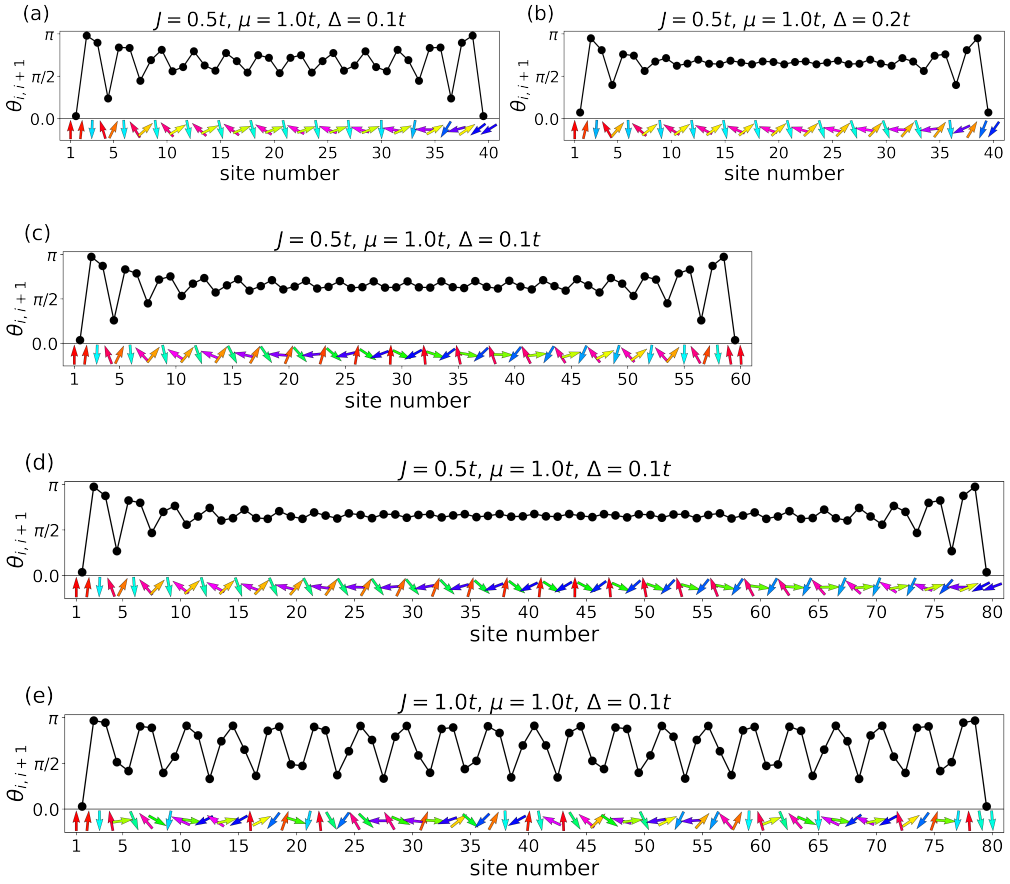

Figure 4.5: **Boundary effects on magnetic ground states with non-vanishing superconductivity.** Relative angle between neighboring spins along finite-size chains with open boundary conditions for $J = 0.5\,t$ and $\mu = 1.0\,t$ for different length L and superconducting order parameters Δ. The insets show a 2D projection of the spins. The color denotes the relative angle between the j-th spin and the first spin $\theta_{1,j}$. **(a)** $L = 40$, $\Delta = 0.1\,t$, **(b)** $L = 40$, $\Delta = 0.2\,t$, **(c)** $L = 60$, $\Delta = 0.1\,t$, **(d)** $L = 80$, $\Delta = 0.1\,t$, **(e)** $L = 80$, $\Delta = 0.1\,t$, $J = 1.0\,t$, $\mu = 1.0\,t$.

4.4 Comparison of Infinitely Long and Finite Chains

Here, we compare the results from the finite and infinite chains to discuss which effects are caused by the finite size and open boundaries. In contrast to infinite chains, in finite chains we find states that consist of a mixture of collinear and non-collinear neighbors. In these states the collinear neighbors are found at the ends of the chains. When increasing Δ, the $\uparrow\uparrow\downarrow\downarrow$-phase and the complex order phase shrink slower for finite chains than for infinite chains. Due to boundary effects, the relative angles along a given chain vary more for finite chains. But in contrast to infinite chains, θ_{change} does not have to be 0 to find electronic non-trivial states in finite chains. Overall, the superconducting order parameter needs to be larger in finite chains in order to fully push out the magnetic states which prevent the formation of non-trivial electronic states in the transition region. This shows that, for magnetically self-consistent calculations, it is important to also consider how boundary effects can change the dynamics of the system.

4.5 Tight-Binding based Classical Spin Monte-Carlo

In this section, we introduce an alternative method for approximating the magnetic ground states of tight-binding models with quasi-classical magnetic moments. First, we start by explaining how this method works and what problems it aims to solve. Second, we compare the results gained from this approximative method to the results from Sec. 4.3, demonstrating its reliability. Third, we discuss the advantages and disadvantages of this method.

Tight-Binding based Classical Spin Monte-Carlo

We developed a new and numerically efficient method to calculate the magnetic ground state of a tight-binding model like the one used in Sec. 4.3. Using a

Monte-Carlo method directly on a tight-binding model is numerically very demanding for large systems. This is mainly caused by the fact that one has to find all eigenvalues in every step of the calculation, causing each iteration of the calculation to scale with $\mathcal{O}(N^3)$. For illustration how this scales to larger systems, in Sec. 4.3, we investigate chains of length $L = 40$. If we wanted to investigate a 2D system with 40×40 sites instead, that would require 64000 times more computation time for each step and approximately 40 times more steps. Considering that the calculation time needed for the 1D system is roughly 20 hours (single-threaded calculations for each data point) on the CPUs available to us (Lenovo Dataplex Servers based on Intel Xeon Processors), without further optimization the calculations would require 5840 years, i.e., not feasible within reasonable time constraints. The other problem of finding the magnetic ground state directly within the tight-binding model is that we gain very little insight into the underlying magnetic forces beyond a few reasonable assumptions. Our method aims to solve both of these issues simultaneously. It works by following these steps:

1. We generate a large set of random magnetic configurations, typically $10^3 - 10^4$ configurations are required. These magnetic configurations are generated by choosing the magnetic moments on each site uniformly randomly from a unit sphere. (Done in milliseconds).

2. We calculate the total energy of the tight-binding Hamiltonian for each configuration as explained in Sec. 3.4. (Scaling with $\mathcal{O}(N^3)$).

3. We construct a classical magnetic Hamiltonian H_{cl}, which can reproduce the magnetism of the tight-binding system. Hereby, the energy parameters of this Hamiltonian serve as fitting parameters. (Between minutes and months of human work, depending on the complexity of the system and the human trying to solve it).

4. We find the constants of H_{cl} by fitting them to the total energies and their respective magnetic configurations. For this, we employ the Levenberg-Marquardt algorithm as implemented in Scipy [170]. (Scaling primarily

with the number of trial configurations and the complexity of the classical Hamiltonian).

5. Finally, we employ a Metropolis Monte-Carlo method, as explained in Sec. 3.2, to identify the magnetic ground states of the fitted classical Hamiltonian H_{cl}.[4] (Scaling with $\mathcal{O}(N^1)$).

The most difficult part of this process is to identify a good classical magnetic Hamiltonian. This Hamiltonian needs to capture all magnetic interactions important to the system while still being simple enough to be fittable, since too many fitting parameters may cause overfitting. Tight-binding systems can inherently cover complex multi-spin interactions. For example, the $\uparrow\uparrow\downarrow\downarrow$-state found in Sec. 4.1 indicates the existence of multi-spin interactions, as a pure translationally invariant two-spin Hamiltonian would always result in harmonic spirals [171]. If those complex interactions are relevant, they need to be included to obtain a high fitting quality. But one cannot simply add all imaginable multi-spin interactions, as this would result in hundreds or even thousands of fitting parameters. Thus, one needs to make educated guesses and some trials to identify a good classical Hamiltonian, identified by a low fitting variance. In general, a good first step is to look into the symmetries of the tight-binding system. For example, without Rashba spin-orbit coupling, the tight-binding system introduced in Eq. (4.1) is completely isotropic, i.e., it is symmetric under a global rotation of all spins. Thus, one can conclude that H_{cl} should only include isotropic terms. This already excludes Dzyaloshinskii–Moriya interaction (DMI) and anisotropic exchange interactions. Effectively, this assumption reduces the number of fitting parameters for two-spin interactions from 9 (a 3×3-matrix connecting two spins) to 1 per considered neighbor. One can also check if natural assumptions for the fitted parameters hold true. For example, it is reasonable to assume that, averaged over many sets of tight-binding parameters, long-range interactions should be less significant than short-range interactions.

[4] Here, we use 2,000,000 MCS in the first part of the cooling with a logarithmic temperature function, then 600,000 MCS further cooling the system with only small changes to the spins and finally 200,000 MCS at zero temperature with only small changes (see Sec. 3.2).

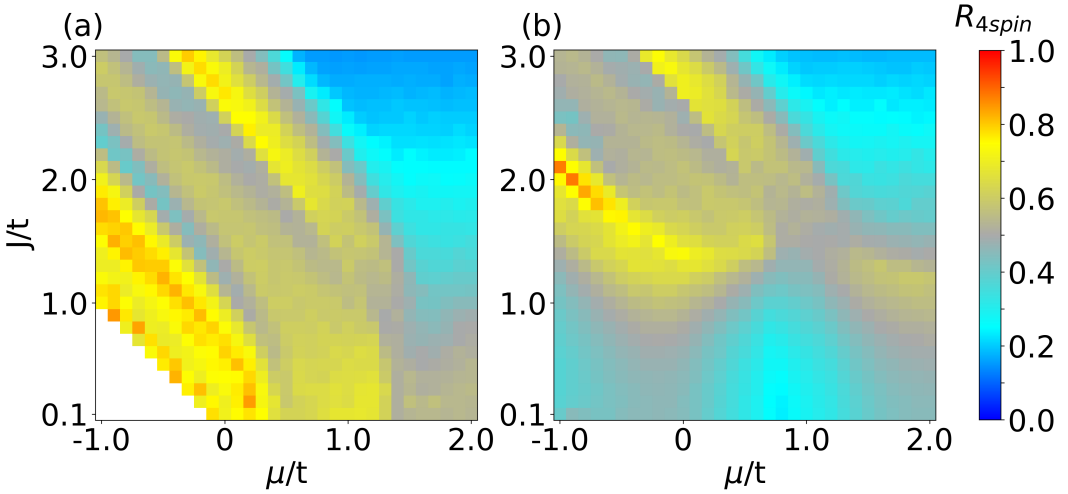

Figure 4.6: **Ratio of the 4-spin interaction** $R_{4\text{spin}}$ for $L = 40$, **(a)** $\Delta = 0$ and **(b)** $\Delta = 1.0\,t$.

To approximate the model used in Sec. 4.3, we employ the classical Hamiltonian

$$\begin{aligned} H_{\text{cl}} = &\sum_{\langle i,j\rangle_5} J_{i,j}\vec{s}_i \cdot \vec{s}_j + \sum_{\langle i,j\rangle_5} A_{i,j}(\vec{s}_i \cdot \vec{s}_j)^2 \\ &+ \sum_{\langle i,j,k\rangle_5} B_{i,j,k}(\vec{s}_i \cdot (\vec{s}_j \times \vec{s}_j)) \\ &+ \sum_{\langle i,j,k,l\rangle_5} C_{i,j,k,l}\big([\vec{s}_i \cdot \vec{s}_j][\vec{s}_k \cdot \vec{s}_l] + [\vec{s}_i \cdot \vec{s}_k][\vec{s}_j \cdot \vec{s}_l] + [\vec{s}_i \cdot \vec{s}_l][\vec{s}_j \cdot \vec{s}_k]\big) \\ &+ \sum_{\langle i,j,k,l\rangle_5} D_{i,j,k,l}\big([\vec{s}_i \cdot \vec{s}_j][\vec{s}_k \cdot \vec{s}_l] + [\vec{s}_i \cdot \vec{s}_k][\vec{s}_j \cdot \vec{s}_l] - 2[\vec{s}_i \cdot \vec{s}_l][\vec{s}_j \cdot \vec{s}_k]\big). \end{aligned} \tag{4.4}$$

This Hamiltonian contains all isotropic two-, three- and four-spin interactions up to the fifth neighbor. The summation over $\langle i,j,k,l\rangle_5$ runs over all combinations up to the fifth neighbor that include at least three different sites. The two-site four-spin interactions are covered by $A_{i,j}$. All constants $J_{i,j}$, $A_{i,j}$, $B_{i,j,k}$, $C_{i,j,k,l}$, $D_{i,j,k,l}$ are translationally invariant, i.e., $J_{i+a,j+a} = J_{i,j}$. We find that the constants before the three-spin interaction, i.e., the scalar triple product of three spins, is consistently fitted to zero. This aligns well with our findings that the system only hosts coplanar states, as a non-zero scalar triple product would incentivize non-coplanar structures. We find that the four-spin interac-

tions are non-vanishing in a significant part of the phase space. The ratio of four-spin interactions

$$R_{4\text{spin}} = \frac{\sum_i (|C_i| + |D_i|)}{\sum_i (|J_i| + |A_i| + |B_i| + |C_i| + |D_i|)} \tag{4.5}$$

is shown in Fig. 4.6. In the AFM-phase, two-spin interactions are dominant, while in all other phases two- and four-spin interactions are of similar strength.

Benchmarking

Here, we discuss how well our approximative method performs when compared to calculations done directly in tight-binding. For this comparison, we choose a 1D system with $L = 40$. To ensure that we do not overfit the classical model, we increase the sample size until the fitting parameters do not change anymore. Here, we set $N = 3000$. Increasing the sample size to $N = 50000$ results only in minimal changes to the fitting parameters. We find

$$\frac{\text{var}(\mathbf{F}(N = 3000) - \mathbf{F}(N = 50000)}{\text{var}(\mathbf{F}(N = 50000))} < 0.01 \tag{4.6}$$

for all tested J, μ and Δ, where $\mathbf{F}$ is a vector that contains all fitting parameters.

To judge the quality of the fits, we use a normalized variance calculated as

$$V = \frac{\text{var}(\mathbf{E}_{\text{HB}} - \mathbf{E}_{\text{tb}})}{\text{var}(\mathbf{E}_{\text{tb}})}, \tag{4.7}$$

where $\mathbf{E}_{\text{HB}}$ and $\mathbf{E}_{\text{tb}}$ are vectors containing the energies calculated via the classical Heisenberg spin-Hamiltonian and the tight-binding model for the same spin configurations, respectively. The variance for $\Delta = 0$ and $\Delta = 1$ is shown in Fig. 4.7. For $J \approx -\mu$ the fitting process fails at $\Delta = 0$, because for many spin configurations no electronic states are occupied. Within the potentially topologically non-trivial region (see Fig. 4.8), the fitting quality is the lowest. The magnetism in that region appears to be highly complex and might require even larger order spin interactions to be fully captured by a classical Heisen-

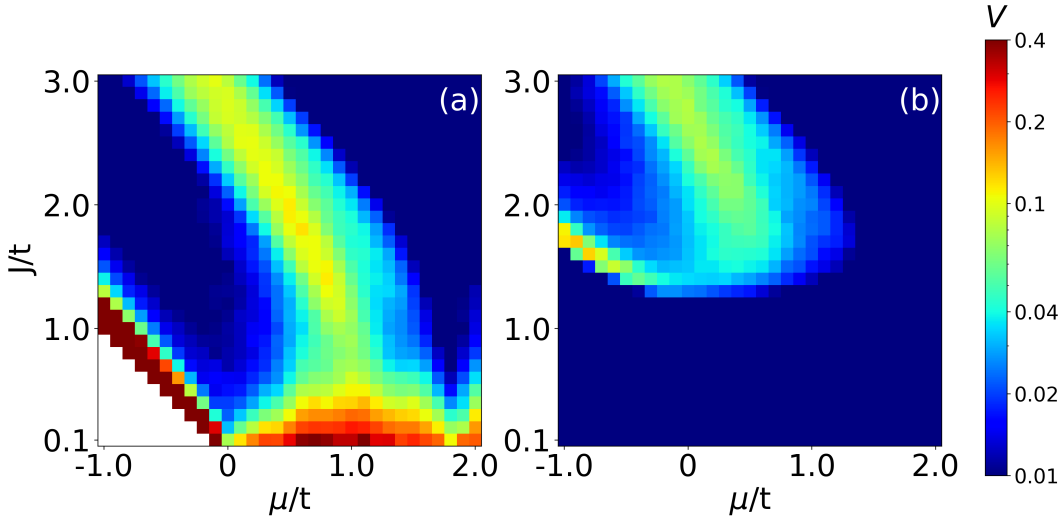

Figure 4.7: **Variance** V of the total energy difference between the tight-binding and the classical Heisenberg model with respect to J and μ for $L = 40$, **(a)** $\Delta = 0$ and **(b)** $\Delta = 1.0\,t$.

berg model. Yet, regarding the general structure of the magnetic ground states, we find good agreement with the tight-binding calculations in this parameter region as well. A direct comparison of θ_{change}, N_{col}, the average angle θ_{average}, and the topological phase between the two methods is shown in Fig. 4.8. The average angle shows a good agreement between the fitted classical model and the tight-binding model. The most notable difference is in an artifact, where the ground state should be ferromagnetic or anti-ferromagnetic, but deviates from that for small sections of the parameter space, showing harmonic spirals with angles close to 0 or π, respectively. It is most recognizable when comparing Fig. 4.8 (a) and (b). Notably, this artifact does not occur if we leave out 4-spin interactions. A direct comparison of total energies shows that these non-collinear structures are indeed energetically favorable in the fitted model, excluding convergence problems in the Monte-Carlo simulations as a potential cause. The fitting quality is also high in that region, showing that the fitting quality alone is not a fully reliable tool to check how good the classical model represents the quantum model. A non-zero θ_{change} occurs in the same general parameter regions in both models. The fitted model is also able to reproduce the $\uparrow\uparrow\downarrow\downarrow$-region, albeit with a slight deformation. For low Δ, we see significant

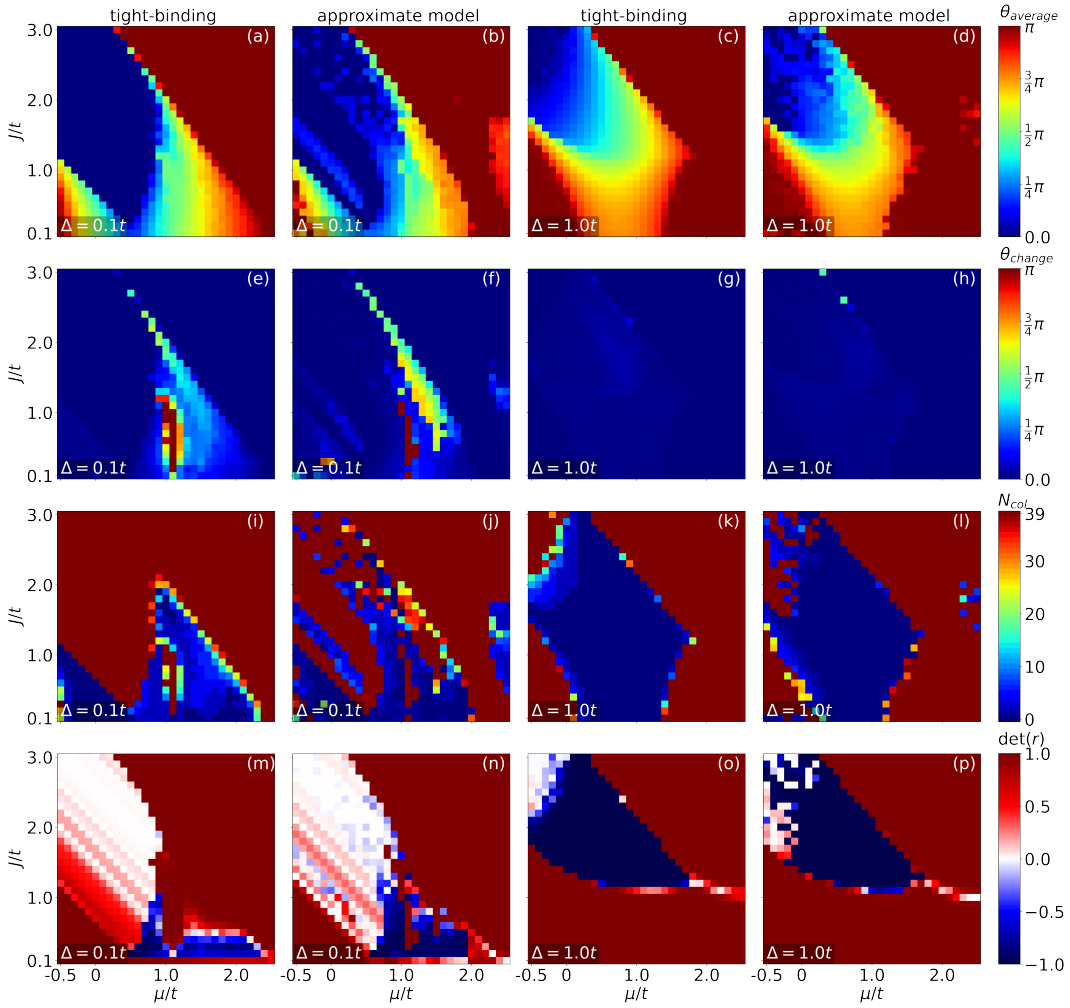

Figure 4.8: **Detailed comparison of our approximative method and Monte-Carlo directly done with the tight-binding model.** For a chain of length $L = 40$, with respect to J and μ, the panels show **(a,b,c,d)** the average angle θ_{average} between neighboring spins, **(e,f,g,h)** θ_{change}, **(i,j,k,l)** N_{col}, **(m,n,o,p)** the determinant of the reflection matrix $\det(r)$ for (a,b,e,f,i,j,m,n) $\Delta = 0.1\,t$ and (c,d,g,h,k,l,o,p) $\Delta = 1.0\,t$ with magnetic ground states obtained (a,c,e,g,i,k,m,o) directly in the tight-binding model, and (c,d,f,h,j,l,n,p) with the fitted classical spin model.

differences in the number of collinear spins N_{col}. In the fitted model, some non-collinear complex order ground states instead appear as collinear complex order, and some collinear states instead appear as spirals with an average angle close to either zero or π in the otherwise ferro- or anti-ferromagnetic regions,

respectively, as discussed above. The topological phase shows a good agreement between both models, albeit with small deviations for $\Delta = 0.1\,t$. Overall, the fitted model replicates general trends and forms of the magnetic phases well, but deviates when looking at exact parameters. Thus, this approximative method is good to explore the magnetic behavior of a system qualitatively, but should not be used for precise quantitative predictions.

Advantages and Disadvantages

As every approximation, our method of finding the magnetic ground state via a fitted classical Heisenberg model has advantages and disadvantages. Summarizing them, this approximative method is computationally very efficient, grants insight into the magnetic behavior and shows a good qualitative agreement for general trends in the parameter space. It comes with the disadvantage that it is not reliable when inspecting the outcomes for specific parameters. Hence, it should not be used for a quantitative analysis of a specific parameter set when high parameter precision is needed. Analyzing the variance of the fit can grant an understanding of how well the classical model is capable of replicating the magnetism of the tight-binding model, but should not be understood as an end-all be-all guarantee for reliable results on the magnetic states. The main advantage of this method is that it is multiple orders of magnitude faster than calculations directly done in the tight-binding model, especially when it comes to larger models. While the energy calculation after changing a single spin in a tight-binding model requires solving the complete eigenvalue problem in every step, scaling with $\mathcal{O}(N^3)$, in the fitted classical model each new spin can be tested locally. Thus, the cost per energy calculation does not scale at all with system size. Compared to other approximative models, our approach has very little limitations to the model. Ruderman–Kittel–Kasuya–Yosida (RKKY) approximations, for example, are limited to small values of J. In theory, our model is capable of capturing any kind of complex magnetism like the 4-spin-interactions shown here. In that regard, it is only limited by what a researcher is willing to implement and test. One can even use this method to test if a specific kind of magnetic interaction

plays a relevant role in the system, e.g., we showed that DMI does not play a role in the system presented above when Rashba spin-orbit coupling is turned off.

4.6 Discussion and Conclusions

We numerically determine the magnetic ground state of finite and infinite suspended magnetic chains with proximity-induced s-wave superconductivity, finding a number of complex collinear, complex non-harmonic, and harmonic spin spiral ground states. For finite Rashba spin-orbit coupling the magnetic ground states are superposed by a non-coplanar conical spiral with the y-axis as rotation axis. For vanishing Rashba spin-orbit coupling, all ground states are coplanar with a uniformly random axis of rotation, reflecting the rotational symmetry of the chains. Contrary to previous results, our investigations show that harmonic spirals are not the magnetic ground state for small to medium values of the superconducting order parameter in large regions of the parameter space. Only for very large superconducting order parameters $\Delta > 1.5\,t$, the assumption of harmonic spirals as ground states holds. While the harmonic spiral phases lead to a non-trivial electronic topological phase, the other magnetic ground states result in trivial electronic topological phases. We also show that for chains on the order of tens of atoms, i.e., typical chain length in atomic spin chain experiments [3], the length of the chain can play a crucial role for the structure of the magnetic ground state due to finite-size effect and thereby indirectly for the formation of Majorana zero modes. Additionally, we present an approximative method to find the magnetic ground state of tight-binding models, which scales better with system size than tight-binding calculations and grants physical insights into the magnetic interactions by setting up a classical Heisenberg model that reconstructs the system's energy from random spin configurations. We find that 4-spin interactions play an important role for the formation of the complex collinear phases.

The demonstration that simple tight-binding models host complex magnetic

structures motivates further research on magnetic tight-binding models and experiments on atomic magnetic chains. Parametric regions where a small change in parameters leads to large changes in the magnetic and electronic topological phases might be of special interest for additional research regarding the control of the location of topological boundary modes. Furthermore, our findings on magnetic ground states facilitate experiments with spin-polarized scanning tunneling microscopy, as knowledge about the structure of expectable magnetic states helps in identifying magnetic states experimentally. Finally, the presented classical Heisenberg approximation allows us to investigate the magnetic ground state of more complex and larger tight-binding models. As long as the tight-binding model can be solved often enough to generate a sample for the fit ($N_{\mathrm{sample}} \approx 10^3 - 10^4$) in reasonable computation times, it can be well approximated with the presented method. Possible systems include magnetic chains on non-magnetic 3D-bulk systems, models that account for large numbers of electronic orbitals, or two-dimensional surfaces. The latter is investigated in the following chapter.

Chapter 5

Magnetic Ground States of a Two-Dimensional Spin Lattice

In this chapter, we shift our focus to two-dimensional systems. We apply the method introduced in Sec. 4.5 to a two-dimensional square lattice and investigate the resulting magnetic states. This chapter is built on our published article [2]

> Jannis Neuhaus-Steinmetz, Tim Matthies, Elena Y. Vedmedenko, Thore Posske, and Roland Wiesendanger
>
> *Large diversity of magnetic phases in two-dimensional magnets with spin-orbit coupling and superconductivity*
>
> Phys. Rev. B **110**, 155427 – Published 15 October, 2024
>
>

First, we introduce the two-dimensional system and tight-binding model in Sec. 5.1.1 and discuss how we apply our approximative method to calculate its magnetic ground state in Sec. 5.1.2. Then, in Sec. 5.1.3, we discuss the Heisenberg parameters acquired from the fits. To categorize the large parameter space with many complex magnetic states, we employ an artificial neural network (ANN). This categorization procedure is explained in Sec. 5.1.4. In Sec. 5.1.5, we discuss the fitting quality and reliability of the magnetic model. In Sec. 5.2, we discuss our findings on the magnetic ground states. In Sec. 5.3, we summarize our results and give an outlook to possible future research.

Work Sharing

The ANN presented in Sec. 5.1.4 has been programmed and run by Tim Matthies, who also created Fig. 5.4 and Fig. 5.5. The calculations of the

magnetic ground state, manual sorting of ANN results, additional criteria for classification, and analysis of the data have been done by myself.

5.1 Model and Method

5.1.1 System

We investigate a two-dimensional electron square lattice with classical local magnetic moments, proximity-induced s-wave superconductivity, Rashba spin-orbit coupling (RSO), and periodic boundary conditions. The system is described by the Hamiltonian

$$\begin{aligned} H =& \sum_{j=1}^{N} \vec{c}_j^{\,\dagger} \Big(- J^{\mathrm{tb}} \tau_0 \vec{s}_j \cdot \vec{\sigma} - B_z \tau_0 \sigma_z - \mu \tau_z \sigma_0 + \Delta \tau_x \sigma_0 \Big) \vec{c}_j \\ &+ \sum_{\langle i,j \rangle_1} \vec{c}_i^{\,\dagger} \Big(t \tau_z \sigma_0 + \mathrm{i}\alpha \left[d_x(i,j) \tau_z \sigma_y - d_y(i,j) \tau_z \sigma_x \right] \Big) \vec{c}_j + \mathrm{h.c.}, \end{aligned} \tag{5.1}$$

with the Nambu spinor $\vec{c}_j = (c_{j\uparrow}, c_{j\downarrow}, c_{j\downarrow}^\dagger, -c_{j\uparrow}^\dagger)$ [136], the coupling J^{tb} between the spin of an electron and a magnetic moment on a given site j, the orientation of the local magnetic moments on the j-th site $\vec{s}_j$, the chemical potential μ, the hopping amplitude t, the superconducting order parameter Δ, the strength of a magnetic field B_z perpendicular to the lattice, and the strength of the Rashba spin-orbit coupling α. The difference in x- and y-position of the sites i and j is given by $d_x(i,j) = x_i - x_j$ and $d_y(i,j) = y_i - y_j$, respectively, assuming a lattice constant of unity and respecting the periodic boundaries. The Pauli matrices σ and τ operate in spin and particle-hole-space, respectively, and are connected by a tensor product. N is the number of sites in the system. The summation over $\langle i,j \rangle_m$ runs over all combinations up to the m-th nearest neighbor. In the above Hamiltonian $m = 1$, meaning that only hopping between nearest neighbors is included.

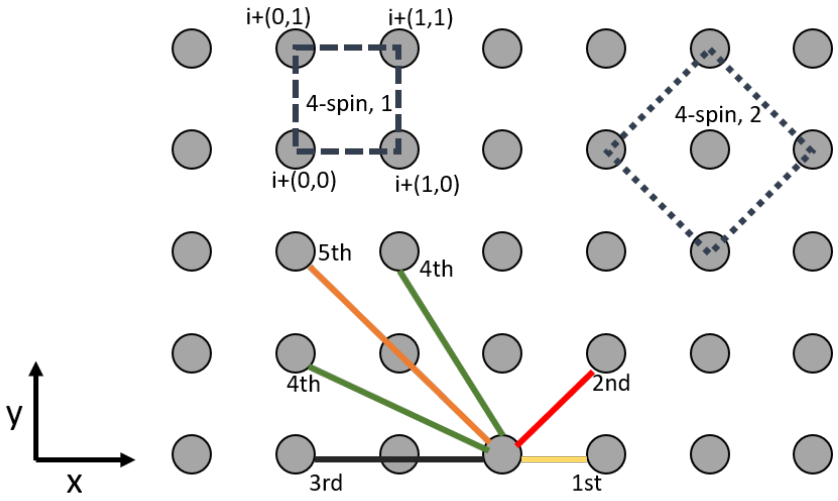

Figure 5.1: **Spin interactions used in Eq.** (5.2)**.** The gray dots represent spins on atomic sites. The filled lines mark 2-spin interactions with the 1st (yellow), 2nd (red), 3rd (black), 4th (green), and 5th (orange) nearest neighbor. The dotted lines show the two considered 4-spin interactions with 1 and 2 denoting the smaller and larger square, respectively.

5.1.2 Ground State Calculations

We consider the local magnetization $\vec{s}$ as a free parameter, not limited by a priori assumptions about the magnetic ground state, and identify the energetically most favorable configuration of the magnetizations $\vec{s}_i$ for a given set of tight-binding parameters J^{tb}, μ, Δ, B_z, and α. Subsequently, we find the ground state in the framework of the Metropolis Monte-Carlo algorithm [137, 138] (see Sec. 3.2). Finding the magnetic ground state, i.e., the magnetic configuration that minimizes the total energy of all occupied states, with a Monte-Carlo procedure directly in the tight-binding framework is computationally very expensive, as the time required to calculate the total energy scales as $\mathcal{O}(N^3)$ with the system size N. To address this problem, we use the approximative approach introduced in Sec. 4.5. First, we generate 8000 random magnetic configurations by choosing each spin $\vec{s}_j$ independently from a random uniform distribution on the unit sphere. Then, we calculate the total energy of the electronic system, i.e., the sum of all eigenvalues of the Hamiltonian in Eq. (5.1)

below the Fermi energy E_{F}, using the *Kwant* code [172]. Following that, we fit the obtained energies to a classical Heisenberg type Hamiltonian, using a least square method, obtaining the constants of the classical model. To take into account the itinerant nature of electrons in 2D systems, we pay particular attention to multi-spin interactions on the order of S^4. In the last step, we use the fitted classical spin model in a Metropolis Monte-Carlo simulation to identify the zero temperature magnetic ground state. The employed classical Heisenberg Hamiltonian on a square lattice with periodic boundary conditions is given by

$$\begin{aligned} H_{\mathrm{HB}} = & \sum_{\langle i,j\rangle_5} \vec{s}_i^{\,T} J_{i,j}^{\mathrm{cl}} \vec{s}_j - \sum_i \vec{B}\cdot\vec{s}_i \\ & + \sum_i C_1^1\big([\vec{s}_i\cdot\vec{s}_{i+(1,0)}][\vec{s}_{i+(1,1)}\cdot\vec{s}_{i+(0,1)}]\big) \\ & + \sum_i C_2^1\big([\vec{s}_i\cdot\vec{s}_{i+(1,1)}][\vec{s}_{i+(1,0)}\cdot\vec{s}_{i+(0,1)}]\big) \\ & + \sum_i C_3^1\big([\vec{s}_i\cdot\vec{s}_{i+(0,1)}][\vec{s}_{i+(1,0)}\cdot\vec{s}_{i+(1,1)}]\big) \\ & + \sum_i C_1^2\big([\vec{s}_i\cdot\vec{s}_{i+(1,1)}][\vec{s}_{i+(2,0)}\cdot\vec{s}_{i+(1,-1)}]\big) \\ & + \sum_i C_2^2\big([\vec{s}_i\cdot\vec{s}_{i+(2,0)}][\vec{s}_{i+(1,1)}\cdot\vec{s}_{i+(1,-1)}]\big) \\ & + \sum_i C_3^2\big([\vec{s}_i\cdot\vec{s}_{i+(1,-1)}][\vec{s}_{i+(1,1)}\cdot\vec{s}_{i+(2,0)}]\big), \end{aligned} \tag{5.2}$$

where the indices i and j are vector valued, containing the x-y-coordinate. $J_{i,j}^{\mathrm{cl}}$ is a 3x3-matrix that includes all possible linear 2-spin interactions. The 4-spin terms C_k^n build a complete linearly independent basis for all isotropic 4-site-4-spin interactions [173]. We exclude otherwise considered 3- and 2-site-4-spin interactions for the sake of simplicity [174]. The interaction strengths $J_{i,j}^{\mathrm{cl}}$, C_1^n, C_2^n, C_3^n are translationally invariant, e.g., $J_{i+a,j+a}^{\mathrm{cl}} = J_{i,j}^{\mathrm{cl}}$, but not a priori directionally invariant. $\vec{B}$ is a vector that represents an external magnetic field and is constant over the whole lattice. The spin interactions are visualized in Fig. 5.1. The summations for 2-spin interactions run over all combinations of spins up to the 5th nearest neighbor, which are induced in multi-hopping processes of the

tight-binding model. The 4-spin interactions consider the two smallest possible squares of sites, i.e., $(0,0),(1,0),(1,1),(0,1)$ and $(0,0),(1,1),(2,0),(1,-1)$ and all translationally equivalent ones. The index n denotes which of these two square types is chosen. To find all $J_{i,j}^{\mathrm{cl}}$, C_k^n, and $\vec{B}$, we fit the Heisenberg model to the energy dependence of the tight-binding model Eq. (5.1) using the Levenberg-Marquardt algorithm implemented in *SciPy* [170]. The resulting classical Heisenberg Hamiltonian is then used in a Metropolis Monte-Carlo simulation to determine the zero temperature ground state.[1] To generate the input for the fit, we use a 15×15 site system. We confirmed with spot checks that further increasing the system size does not lead to a significant change in fitting constants in Eq. (5.2). As we are able to calculate the fitting input from a smaller system, and the change in energy from changing a singular spin in the Metropolis Monte-Carlo simulation can be calculated locally in a classical spin model, the required calculation time for each energy calculation does not scale with system size. Thus, this provides a very efficient method to find ground states of large systems, such as the one at hand.

5.1.3 Heisenberg Parameters

In the following, we discuss our results of the fitted classical magnetic parameters. First, we can describe the components of J_{ij}^{cl} as exchange and Dzyaloshinskii–Moriya interaction (DMI):

$$\begin{aligned} \vec{s}_i J_{ij}^{\mathrm{cl}} \vec{s}_j &\approx \vec{s}_i \begin{pmatrix} J & D_{xy} & -D_{xz} \\ -D_{xy} & J & D_{yz} \\ D_{xz} & -D_{yz} & J \end{pmatrix} \vec{s}_j \\ &= J\vec{s}_i \cdot \vec{s}_j + \vec{D} \cdot \vec{s}_i \times \vec{s}_j \end{aligned} \tag{5.3}$$

with the DMI-vector $\vec{D} = (D_{yz}, D_{xz}, D_{xy})^T$ and the classical exchange J where negative J correspond to ferromagnetic coupling. The coupling constant J and the components of $\vec{D}$ depend on the combination of sites i and j, which is left

[1] Here, we use 6,400,000 MCS in the first part of the cooling with a logarithmic temperature function, and then 1,600,000 MCS further cooling the system with only small changes to the spins (see Sec. 3.2).

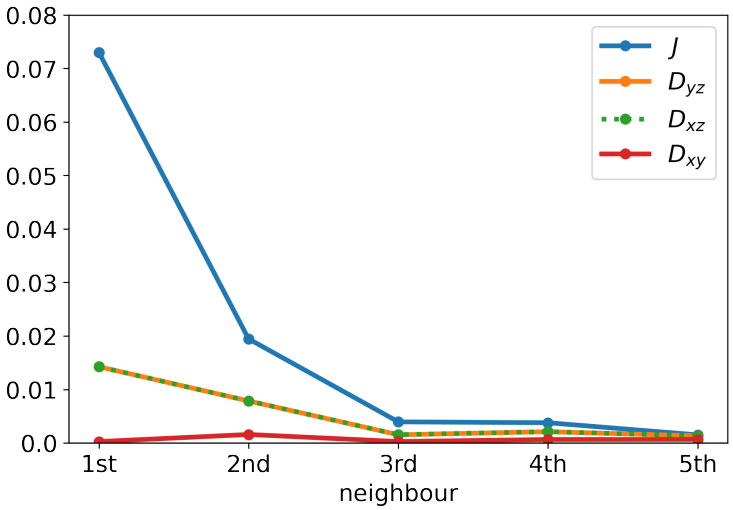

Figure 5.2: **Two-spin interactions.** Absolute values of diagonal and off-diagonal elements of J_{ij}^{cl} for $\alpha = 0.2\,t$, $\Delta = 0.5\,t$ and $B_z = 0$ with respect to the neighbors averaged over J^{tb} and μ, where the variance of the fit is lower than 0.2.

out in Eq. (5.3) for better readability. Notably, exchanging i and j changes the sign of $\vec{D}$. Fig. 5.2 shows the average of the absolute values of J and $\vec{D}$ with respect to the distance between i and j, averaged over all J^{tb} and μ for $\alpha = 0.2\,t$, $\Delta = 0.5\,t$ and $B_z = 0$. Changing the superconducting order parameter Δ and the magnetic field B within the considered parameter range only causes minimal changes to these averages. Setting the spin-orbit coupling $\alpha = 0$ removes the off-diagonal elements and increases the strength of the diagonal elements. In this case, we find that the diagonal elements of a given matrix J_{ij}^{cl} are always nearly identical, i.e., their variance is around 0.01%. Therefore, we find no anisotropy for the diagonal elements and they can be understood as the classical exchange interaction with a scalar product $\vec{s}_i \cdot \vec{s}_j$ as in Eq. (5.3), which is consistent with the symmetry of the initial tight-binding model. We also observe that the exchange interaction becomes significantly smaller on average with increasing distance, showing that long distance interactions are less important than short distance interactions as one would naturally expect, see Fig. 5.2 for representative parameters. The off-diagonal elements can be mapped to DMI-vectors, which are oriented perpendicular to

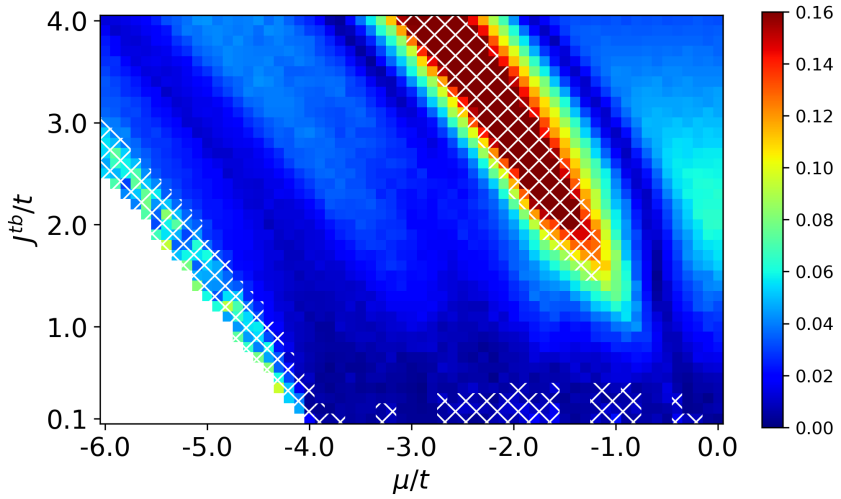

Figure 5.3: **Relative strength of 4-spin interactions** for $\alpha = B_z = \Delta = 0$ in dependence on J^{tb} and μ, calculated by the sum of the absolute values of all C_l^n divided by the sum of the absolute values of all parameters in Eq. (5.2). White denotes regions with largely unoccupied bands. In the hatched area, the variance of the fit exceeds 15%, which we consider unreliable, see Sec. 5.1.5.

the vector between the respective sites and mostly lie in the xy-plane, i.e., the D_{xy} component is very small. We also find that B_z in the tight-binding model directly translates to a $\vec{B}$-field in z-direction in the classical model, as expected. In Fig. 5.3, the relative strength of the 4-spin interaction is shown, which is calculated as the sum of the absolute values of all C divided by the sum of the absolute values of all fitted parameters in Eq. (5.2). We found a small, but still significant contribution of 4-spin interactions in well-fitted regions. This indicates that this simple seeming tight-binding system hosts complex multi-spin interactions beyond 2-spin interactions. The largest 4-spin contribution is found in a region, where the fitting quality is insufficient. Since the addition of 4-spin interactions improves the fitting quality in that region, we speculate that this region is dominated by higher order or further reaching multi-spin interactions. Adding non-vanishing RSO of $\alpha = 0.2\,t$ causes only minimal changes in the pattern of 4-spin interactions. The relative strength is lowered by $\sim$28% on average, mostly due to an absolute increase in the strength of 2-spin interactions due to the addition of DMI.

5.1.4 Classification of Magnetic Phases using Contrastive Clustering

Our model hosts a rich and complex magnetic phase diagram. With over 20,000 data points, manual classification by hand would be a time-consuming task, and algorithmic classification using if-statements has the disadvantage of potentially missing unexpected magnetic configurations. We solve this issue by combining Contrastive Clustering via an artificial neural network (ANN) with manual spot checks and additional criteria. First, we use Contrastive Clustering [66] to cluster our 20,000 data points into 40 clusters. Then, the clusters are categorized into magnetic phases by spot checks. This highlights the main advantage of using Contrastive Clustering to cluster our data. Instead of categorizing 20,000 data points by hand, we only need to perform a few hundred spot checks. Additionally, skyrmion phases are identified by calculating the skyrmion number. In the following, we explain our categorization process in detail.

To gain a better overview of the magnetic ground states, we employ Contrastive Clustering [66], an unsupervised learning technique where the learning of a latent representation and cluster assignment are performed simultaneously by comparing different samples. The samples get encoded into points in a representation space, called the *latent space*. The goal is to attract points in this space if they correspond to the same phase and repel them if they come from different phases. To achieve this, we apply symmetry transformations to magnetic configurations. Two transformed images attract each other if they originate from the same configuration or else they repel, as visualized in Fig. 5.4. The details of the implementation of Contrastive Clustering follow Ref. [66]. We use Resnet18 [177] as the encoder network, Adam [178] to train the network, and train our network for 2000 cycles over the whole dataset, ensuring sufficient convergence of our loss function. To deal with the unbalanced nature of our dataset, we adapt an oscillating computational temperature in the contrastive loss, as this has been shown to perform better with long-tail data [179], i.e., data where a small part of classes have a large number of sample points, but the others are associated with only a few samples [180]. We imple-

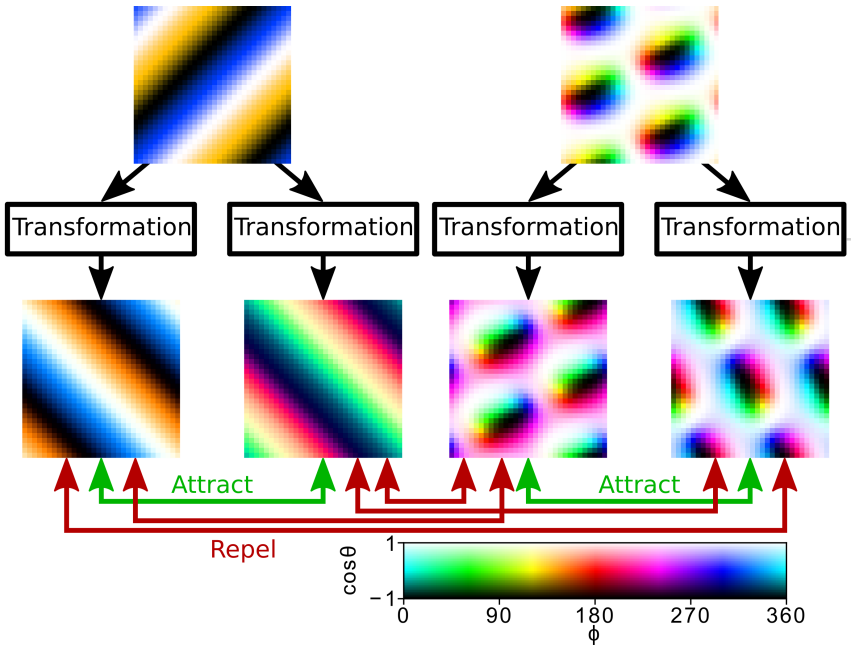

Figure 5.4: **Visualization of the transformations used for the contrastive learning procedure.** The top row shows two samples from the dataset, a spin spiral, and a skyrmionic configuration. We apply four different transformations to each sample: A random rotation in real space by 0°, 90°, 180°, or 270°, a random translation, and a random SO(3) rotation of all spins. All transformations are chosen uniformly randomly and are equally likely. The objective of contrastive learning is to put transformed samples from the same original configuration close together in a latent space and repel samples that do not come from the same configurations.

ment the best-performing parameters of Ref. [179]. For the transformations, we use intrinsic symmetries of the magnetic structure identification, which are a rotation of the whole lattice by either 0°, 90°, 180°, or 270°, a shift of the lattice by a random amount in the x- and y- directions, and rotation of all spins together in a random direction. This last step violates the axial anisotropy of the system when the Rashba spin-orbit coupling α or the magnetic field $\vec{B}$ is non-zero. We successfully classify the unlabeled spin data into different phases. Hence, we create a phase diagram without having to specify the phases in advance, which allows the detection of unexpected phases. The latent space after the training procedure can be seen in Fig. 5.5. We provide an online tool for a

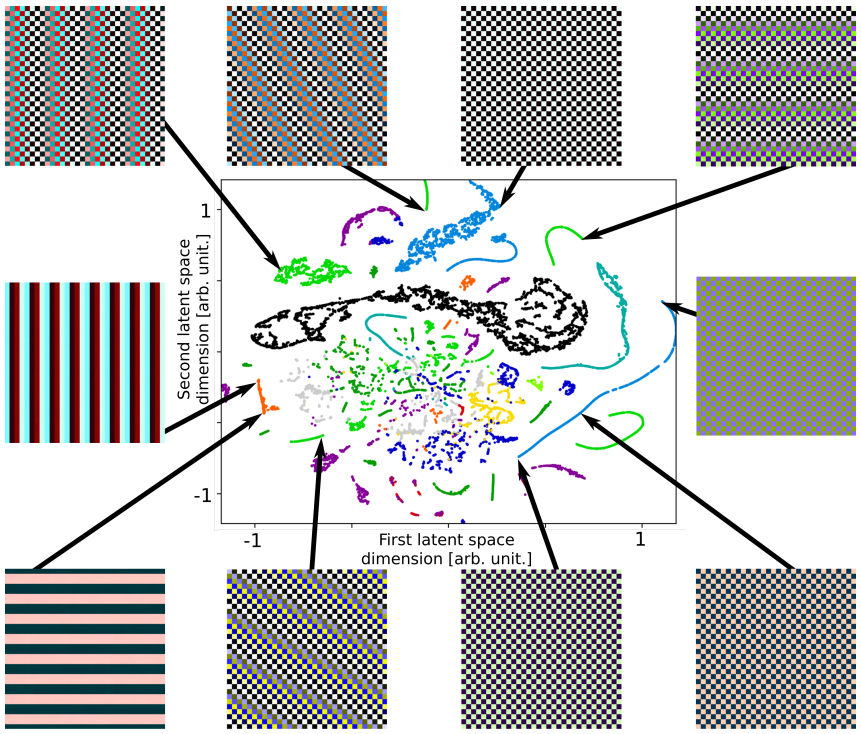

Figure 5.5: **Similar magnetic configurations identified by Contrastive Clustering and their location in latent space.** Each point in the scatter plot (center) corresponds to a configuration in the dataset. The 128-dimensional latent space is reduced to a two-dimensional space by t-distributed stochastic neighbor embedding (t-SNE) [175] for visualization. Each point is colored in accordance with the assigned phase, with the colors being the same as in Fig. 5.7. The color map for the configurations is the same as in Fig. 5.4. Arrows indicate the locations of ten representative configurations in the latent space. More samples can be viewed and explored online [176].

more in-depth exploration of the latent space and the data [176].

We use the Contrastive Clustering to split the magnetic ground states into 40 clusters. Those clusters are then manually assigned to 11 magnetic phases, which we identify by spot checks. Often, multiple clusters belong to the same magnetic phase, e.g., there are multiple clusters with harmonic spin spirals but different ranges of relative angles. Using more clusters than the number of magnetic phases is necessary because an ANN can only differentiate different-looking states without knowledge of the physical interpretation. For example, when limited by too few clusters, the ANN might wrongly assign a 177°-spiral to

anti-ferromagnets instead of spirals. When a cluster cannot be clearly assigned to a single magnetic phase, i.e., when we identify multiple different magnetic phases within one cluster, we label that cluster as *mixed*. Three of the clusters initially labeled as *mixed* could be separated by adding an additional condition. For one of those, all states with $\mu < -2.0\,t$ belong to a magnetic 2×2-pattern, while the rest belong to AFM spin spirals. The other two contain harmonic spin spirals and 2q-spin-spirals, but for $\alpha = 0$ only contain harmonic spin spirals. Additionally, the ANN often combines skyrmion lattices and spin spirals with a periodicity that is similar to the skyrmion size into one cluster. To reliably identify skyrmionic phases, we employ the skyrmion number N_{sk}, which is calculated by

$$N_{\mathrm{sk}} = \frac{1}{4\pi} \sum_{\mathrm{sites}} \vec{M} \cdot \left(\frac{\partial \vec{M}}{\partial x} \times \frac{\partial \vec{M}}{\partial y} \right), \tag{5.4}$$

where $\vec{M}$ is the local magnetization and where we calculate the derivatives of the continuum extrapolation by the inverse Discrete Fourier Transform (DFT) of the product of the DFT frequencies and the DFT of the spins using $f'(x) = \frac{1}{N} \sum_k e^{\mathrm{i}kx} (\mathrm{i}k) \sum_z e^{-\mathrm{i}kz} f(z)$. This avoids numerical artifacts for anti-ferromagnetic states that can appear with lattice adapted invariants [181] at the cost of deviations from the integer quantization of the skyrmion number. We assign all states with $|N_{\mathrm{sk}}| > 0.95$ as part of a skyrmionic phase, giving some tolerance for numerical precision.

5.1.5 Discussion on the Fitting Quality and Reliability of the Magnetic Model

To judge the quality of the fits, we employ the normalized variance

$$V = \frac{\mathrm{var}(\vec{E}_{\mathrm{cl}} - \vec{E}_{\mathrm{tb}})}{\mathrm{var}(\vec{E}_{\mathrm{tb}})}, \tag{5.5}$$

where $\vec{E}_{\mathrm{cl}}$ and $\vec{E}_{\mathrm{tb}}$ contain the total energies calculated with the fitted classical model and the original tight-binding model, respectively. The resulting variance is shown in Fig. 5.6 for the datasets used in the main text. For simul-

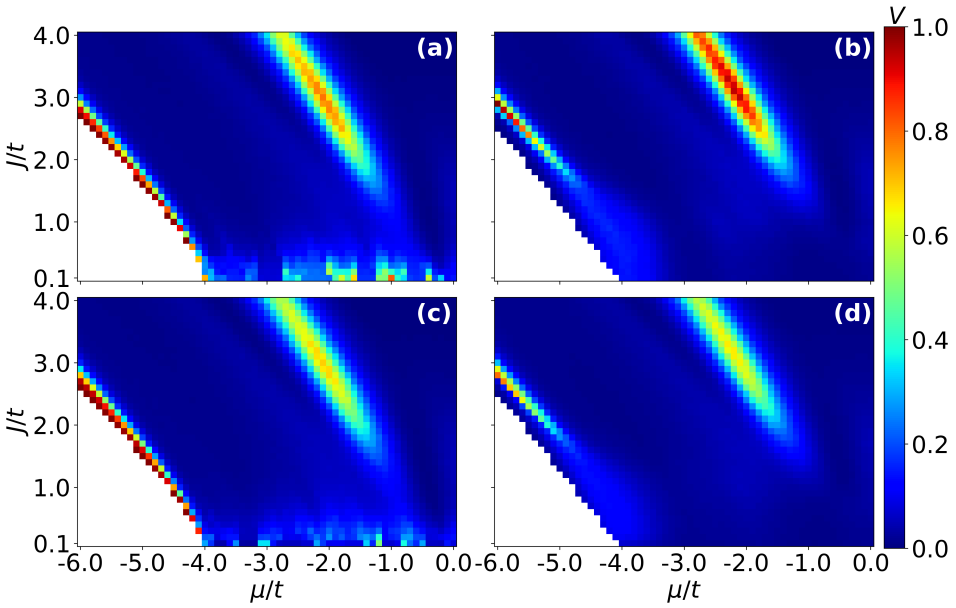

Figure 5.6: **Normalized variance as a measure for fitting quality** for **(a)** $\alpha = 0, B_z = 0, \Delta = 0$, **(b)** $\alpha = 0, B_z = 0, \Delta = 0.5\,t$, **(c)** $\alpha = 0.2\,t$, $B_z = 0.02\,t, \Delta = 0$ and **(d)** $\alpha = 0.2\,t$, $B_z = 0.02\,t$, $\Delta = 0.5\,t$ in dependence on J^{tb} and μ. White denotes regions with largely unoccupied bands.

taneously small μ and J, no bands reach below the Fermi energy for $\Delta = 0$, and for $\Delta > 0$ the spin structure has no significant contribution to the total energy. At the edge of this region, bands are only occupied for some magnetic configurations, which results in bad fits. The variance has a large peak next to the AFM region towards lower μ. In this region the fitting quality is not good enough to make reliable assessments. However, we did observe that the fitting quality significantly increased (lowering the peak variance from 0.96 to 0.78) by including 4-spin-interactions, while adding more long-range 2-spin-interactions, i.e., 6th to 10th neighbor 2-spin-interactions, did not lead to any improvements. This suggests that higher-order interactions are required to fully understand the magnetism in this region. This is also in line with our results from the one-dimension model (see Sec. 4.5), where a parameter region left of the AFM phase could only be fitted by including 4-spin-interactions. We also observe a high variance for small values of J when $\Delta = 0$. In Sec. 5.2, we crossed out regions where the variance is larger than 0.2 to display that the

results in these regions are not reliable. Similarly, data close to the crossed-out regions should also considered with caution, as the variance changes smoothly with the parameters of the tight-binding model.
Regarding the sample size, we settled for a value of $N_{\text{sample}} = 8000$. For larger sample sizes the variance does not increase further, showing that 8000 is sufficient to prevent overfitting.

5.2 Magnetic Ground States

For the sake of clarity, we limit ourselves to two distinct values for each of the parameters Δ, B_z and α, representing the presence or absence of the corresponding physical properties, while scanning for a wide range of J^{tb} and μ. We start by providing an overview of the kinds of magnetic ground states found in our calculations. Then, we describe systems with vanishing Rashba spin-orbit coupling and vanishing magnetic fields, with and without non-vanishing superconductivity. Afterwards, we show the influence of non-vanishing RSO in combination with an external magnetic field, which typically stabilizes skyrmions.

5.2.1 Vanishing Rashba Spin-Orbit Coupling

We calculate the magnetic ground states of a 32×32 system with periodic boundary conditions in real space. The ANN-classified magnetic states as described in Sec. 5.1.4 with respect to the magnetic coupling J^{tb} and the chemical potential μ are shown in Fig. 5.7 for $\Delta = 0$ and $\Delta = 0.5\,t$ without RSO, i.e., $\alpha = 0$. Fig. 5.7 (b) and (c) show phase diagrams for $\Delta = 0$ and $\Delta = 0.5\,t$, respectively. Examples of ground states are presented in Fig. 5.7 (a).

Let us first provide an overview over the types of identified magnetic ground states. The *ferromagnetic* (FM) state describes a state in which all spins are parallel. In the case of *x/y-row-wise spirals* and *spin spirals*, the spins are aligned parallelly in one direction and as a harmonic spin spiral in the perpendicular direction, i.e., the relative angle between spins remains constant in the propagation direction of the harmonic spin spiral. In the case of the *x/y-row-wise spin spirals*, the propagation direction of the spin spiral is either the x- or

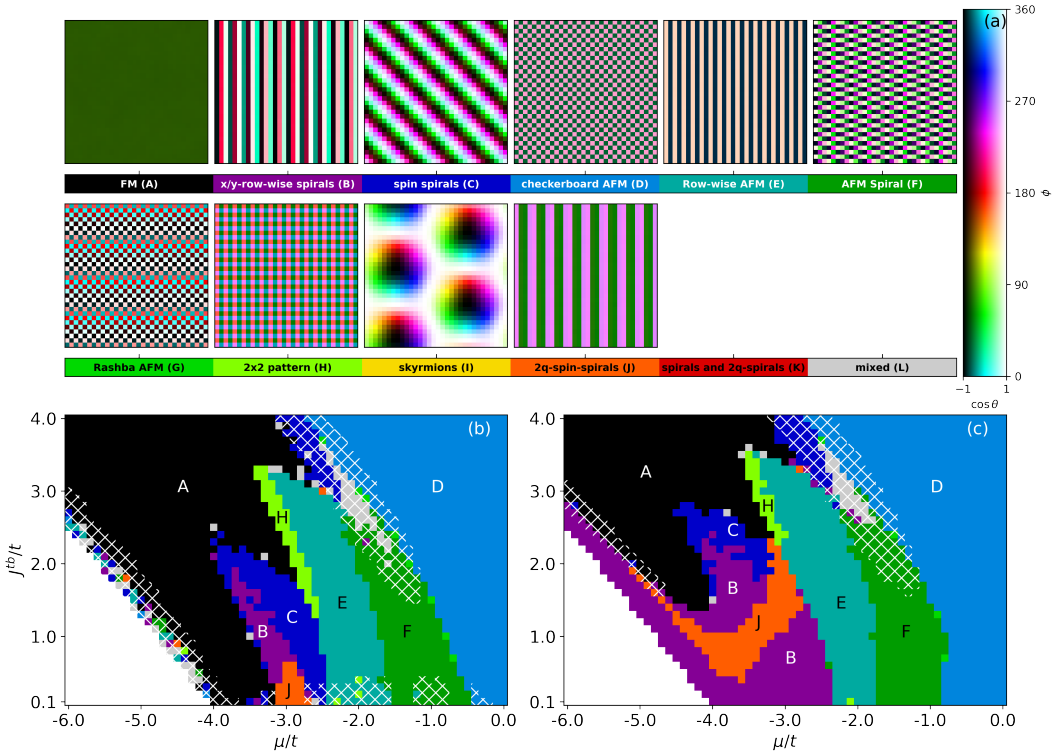

Figure 5.7: **Magnetic ground states** for $\alpha = 0$, $B_z = 0$ with **(b)** $\Delta = 0$ and **(c)** $\Delta = 0.5\,t$ with respect to μ and J^{tb}. The color white denotes regions with largely unoccupied bands. The hatched area leaves the validity regime of the model (see Fig. 5.3). The colorbar for (b) and (c) is given in **(a)** with examples for each type of magnetic ground state, where the color denotes the orientation of the spins with each pixel representing one spin. For *spin spirals and 2q-spin-spirals* and *mixed*, no examples are given.

y-axis, while the other *spin spirals* summarize all other spiral directions and clusters that were mixed between the x/y direction and other directions. The *checkerboard AFM* phase is defined by all spins being aligned anti-parallelly to all of their nearest neighbors. The *row-wise AFM* has parallel spins along one direction and anti-parallel nearest neighbors along the perpendicular direction. *AFM spin spirals* correspond to the spins being aligned as harmonic spin spirals in one direction and anti-parallel in the perpendicular direction. The *Rashba AFM* states are specific AFM spin spirals that can be described as a superposition of a *checkerboard AFM* and a harmonic spin spiral with an angle that is characteristic for the chosen RSO strength α, i.e., constant

for a chosen α. We observe no inherent preference for the orientation within the x-y-plane for the *Rashba AFM*, *row-wise AFM* and *AFM spin spiral*. We also identify a phase with a *2×2 pattern*, where we find a repeated structure of 2 times 2 spins with the following two additional properties. First, along the x- and the y-axis the relative angles are constant in their absolute value but alternating in sign along each axis, e.g., the relative angle along the x-axis alternates between $+80°$ and $-80°$. Second, all spins are anti-parallel to their next-nearest, i.e., diagonal, neighbor. We label a phase as *skyrmions* if we find a skyrmion number $|N_{\mathrm{sk}}| > 0.95$, see Eq. (5.4). In most skyrmionic cases, we observe a skyrmion lattice, while in some cases singular skyrmions appear in a ferromagnetic background. In *2q-spin-spirals*, we observe parallel spins in one direction and following a pattern of two alternating relative angles θ_1 and θ_2 in the perpendicular direction. For $\alpha = 0$, these two angles average to $(\theta_1 + \theta_2)/2 = \pi/2 \pm 0.01$ in 85% of cases. While in the harmonic FM and AFM spin spiral phases, the magnetization rotates with a wave-vector q along high symmetry crystallographic directions, the multi-q-spin-structures are superpositions of several rotations with high symmetry q-vectors [33]. *Spin spirals and 2q-spin-spirals* denote that the ANN cannot differentiate between 2q-spin-spirals and harmonic spin spirals, which only occurs for $\alpha = 0.2$. *Mixed* denotes that the ANN creates a label which we could not assign a definite magnetic state to.

Before discussing the influence of superconductivity, we start with $\Delta = 0$, i.e., vanishing superconductivity. For large $J^{\mathrm{tb}} > 5.0\,t$, we only observe ferromagnetic and anti-ferromagnetic phases. For smaller J^{tb}, we observe rich magnetic phases between the FM (A) and AFM (D) phase shown in Fig. 5.7 (b). For chemical potentials $-1.7t < \mu < -0.9t$, we find AFM spirals (F). At $\mu < -1.7t$, this phase transitions into row-wise AFMs (E). For lower chemical potentials, we find harmonic spin spirals with varying propagation directions other than the x- or y-axis (C). Lowering the chemical potential further results in x-y-row-wise spin spirals (B) and then in a FM phase. For $J^{\mathrm{tb}} > 1.2\,t$, the row-wise AFM phase first transitions into a 2×2 pattern (H) and then into the FM phase. Additionally, around $\mu = -3.0\,t$ and $J^{\mathrm{tb}} < 0.4\,t$, there is a small region in parameter space with 2q-spin-spirals (J).

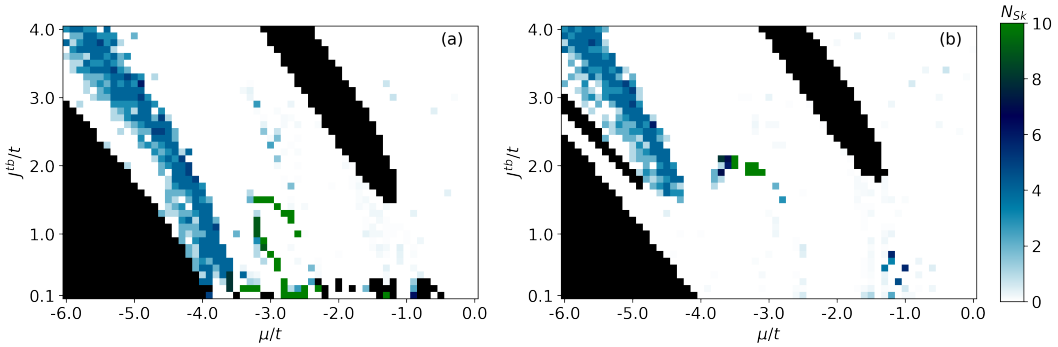

Figure 5.8: **Absolute value of the skyrmion number** $|N_{\mathrm{sk}}|$ (denoted by the color) with respect to J^{tb} and μ for $\alpha = 0.2\,t$, $B_z = 0.02\,t$ with **(a)** $\Delta = 0$ and **(b)** $\Delta = 0.5\,t$. The blacked out regions leaves the validity regime of the model and is equivalent to the hatched area in Fig. 5.3.

For non-vanishing superconductivity, $\Delta = 0.5\,t$, the position and the shape of the magnetic phases change slightly as shown in Fig. 5.7 (c). The AFM (D) and AFM spiral (F) phases remain mostly unchanged. The area of the 2×2 pattern (H) becomes slightly smaller, being replaced by row-wise AFMs (E) for $J^{\mathrm{tb}} < 2.2\,t$. The x/y-row-wise spin spiral phase (B) grows considerably and within it, the 2q-spin-spiral phase (H) moves towards larger J^{tb} and also expands. As large parts of the latter follow an ↑↑↓↓-pattern, this stands in contrast to our results from a very similar Hamiltonian in 1D (Chapter 4), where increased superconductivity causes this phase to vanish. The spin spiral phase (C) moves towards larger J remaining at the transition between the FM (A) and the x/y-row-wise spin spirals (B).

5.2.2 Non-Vanishing Rashba Spin-Orbit Coupling

Skyrmion lattices can be stabilized by an external magnetic field perpendicular to the lattice [99, 102, 182]. We therefore add RSO coupling $\alpha = 0.2\,t$ and a small magnetic field $B_z = 0.02\,t$ and succeed in finding a parameter region with skyrmion lattices. The magnetic field breaks the rotational symmetry of the Hamiltonian. Fig. 5.8 shows the skyrmion number with respect to the magnetic coupling strength J^{tb} and the chemical potential μ for superconducting order parameters $\Delta = 0$ and $\Delta = 0.5\,t$. An extended large skyrmionic phase

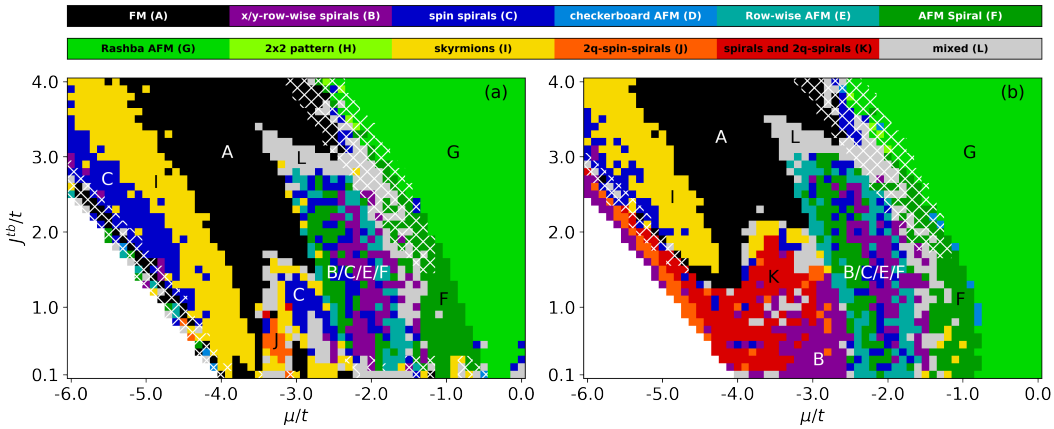

Figure 5.9: **Magnetic ground states** in systems with Rashba spin-orbit coupling $\alpha = 0.2\,t$ and an additional out-of-plane magnetic field $B_z = 0.02\,t$ and **(a)** $\Delta = 0$, **(b)** $\Delta = 0.5\,t$ with respect to μ and J^{tb}. The color white denotes regions with largely unoccupied bands. The hatched area leaves the validity regime of the model (see Fig. 5.3).

emerges, which gradually moves to larger J^{tb} when the superconducting order parameter Δ is increased.

The effect of RSO coupling and a magnetic field on the other phases is displayed in Fig. 5.9. Besides the appearance of a new skyrmionic and spin spiral phase for low μ within the FM phase, the overall shape of the phases remains largely unchanged, but the magnetic structures within the phases change. The previous checkerboard AFM phase becomes a checkerboard AFM in superposition with a spin spiral with a characteristic angle of 0.124π, which we called *Rashba AFM* here. Most parts of the FM phase remain ferromagnetic, but towards lower μ, an additional skyrmionic and spin spiral phase occurs. The inner parts of the row-wise AFM phase is replaced by spin spirals, only some of which are AFM spirals. The 2×2 pattern does not occur anymore. For $\Delta = 0.5\,t$, the 2q-spin-spiral phase still exists, but the ANN fails to differentiate it from harmonic row-wise spin spirals.

5.3 Conclusions and Outlook

Our results show that a simple effective model for magnetic moments coupled to a superconducting substrate with Rashba spin-orbit coupling accommodates an unexpectedly rich phase diagram, helping with the search for exotic and non-collinear phases at magnetic surfaces, which can be effectively categorized by an ANN with a contrastive learning algorithm. The combination of the 2D tight-binding model with Monte Carlo simulations permits us to comprehensively categorize the magnetic ground states in the SC and non-SC regimes. In addition to the collinear FM and AFM configurations as well as harmonic non-collinear states known from one-dimensional models, 2D systems accommodate multi-q collinear structures and non-trivial non-collinear configurations like Rashba-AFM or 2q-spin-spirals. An interesting property of an ultrathin film on a square lattice is the appearance of multi-spin interactions that have been predicted to exist in itinerant magnets but are only important in few experimental studies so far like the nanoskyrmion lattice in Fe/Ir(111) [34]. Our phase diagrams assist researchers working with ultrathin magnetic films by showing them what types of magnetic ordering they can expect in their system or, vice versa, to estimate model parameters from the observed magnetic ordering. Generally, superconductivity decreases the area of the FM phase in favor of non-collinear structures, and Rashba coupling favors non-collinearity. Given that chiral structures are promising candidates to induce non-trivial electronic topological states, one could further explore the electronic properties of the presented magnetic systems with the described self-consistent model. This includes skyrmionic, multi-Q, and spiral magnetism in combination with a non-vanishing superconducting order parameter and potentially topological insulators [35, 183–185]. This finding prompts to look further into the electronic topological properties of the described system in external magnetic fields and for different anisotropy types. Specifically, an investigation of the electronic topology of a magnetic island with open boundary conditions instead of periodic boundaries could reveal whether skyrmions and Majorana modes can occur naturally in the same sample without a preset magnetization [185]. The presented method of finding magnetic ground states of tight-binding models

can also be applied to more complex systems. One possible direction is to create a model of a complex artificial array of magnetic atoms on a superconducting surface [30], and find the dependence of magnetic ground states on the symmetries of this array by using the proposed method of reducing the system to a model containing only the magnetic moments, which is especially efficient when only a small fraction of the total system is magnetic.

Chapter 6

Precursors of Majoranas - Mn Atomic Chains on Superconducting Bulk Nb

In this chapter, we discuss the modeling of a Mn atomic chain on a superconducting bulk Nb substrate with a three-dimensional tight-binding model. The model is specifically crafted and adjusted to replicate STM experiments on this system, performed by Lucas Schneider and Phillip Beck. Large parts of this chapter closely follow our joint publication [3]

> Lucas Schneider, Philip Beck, Jannis Neuhaus-Steinmetz, Levente Rózsa, Thore Posske, Jens Wiebe, and Roland Wiesendanger
>
> *Precursors of Majorana modes and their length-dependent energy oscillations probed at both ends of atomic Shiba chains*
>
> Nature Nanotechnology **17**, pages 384-389 - Published 07 March 2022
>
> Reproduced with permission from Springer Nature,

although some additional theoretical calculations not covered in the original publication are provided here. By exploring this model, we aim to gain a deeper understanding of the experimental system at hand. First, we begin with a short summary of the experimental results in Sec. 6.1 to provide context for the calculations. Then, we introduce the tight-binding model in Sec. 6.2. In that section, we begin by replicating the main findings of the experiment. Thereafter, we explore the system beyond the experimental limitations, like investigating chains much longer than experimentally realized. Lastly, in Sec. 6.3 we summarize our findings and provide an outlook for future research.

Work Sharing

The experimental measurements in this chapter were done by Lucas Schneider and Phillip Beck. I performed the tight-binding calculations presented in Sec. 6.2. The original publication [3] also contains results on theoretical models created by Dr. Levente Rózsa and Dr. Thore Posske, which are not presented here.

6.1 Experimental Results

In this section, we summarize the results of experiments on Mn chains on superconducting bulk Nb to provide context for calculations on this system.
The experimental results are remarkable, because this is the first time that zero-bias peaks in a hard SC gap have been measured simultaneously on both ends of a defect-free adatom chain on the surface of an elemental superconductor. In previous experiments, such peaks have only been found on some chains in the system, i.e., not consistently on all similar chains, and only on one of the ends of the chains [16].
At the heart of the experiment lies the idea to design an effective one-band system from a single hybridizing YSR state in a bottom-up approach. To do so, microscopic insights into the low-energy band formations are exploited. Short Mn chains are constructed on Nb(110) in the $[1\bar{1}0]$ direction atom by atom up to 45 atoms in length by tip-assisted atom manipulation with an STM. While doing so, the $\mathrm{d}I/\mathrm{d}V$ spectrum is measured along and around the chain for each length, using STM and STS with a superconducting tip.

To understand the building blocks of this system, we start by discussing the states resulting from a single Mn atom on clean Nb(110). Fig. 6.1 (a) shows the density of states measured on the added Mn atom and on the bare Nb(110) substrate. There are multiple YSR states induced by the magnetic Mn atom inside the SC gap. The LDOS of the lowest energy YSR state (called δ-state from here on) is shown in Fig. 6.1 (c,d). The δ-state shows a strong spatial anisotropy and extends into the $[1\bar{1}0]$ direction. This anisotropy facilitates different hybridizations in different directions. The Mn chains are constructed

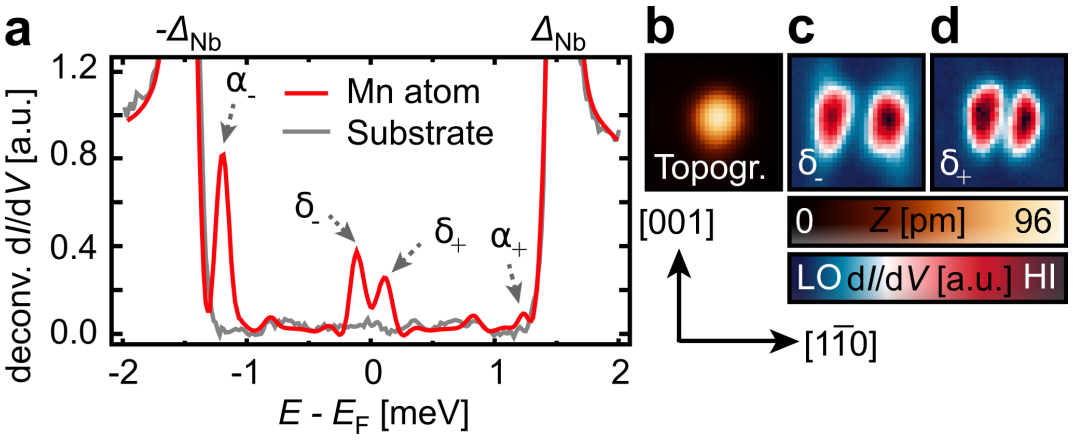

Figure 6.1: **Single Mn impurity on Nb(110). (a)** DOS of a single Mn atom on Nb(110) and DOS measured on bare Nb(110). **(b)** Topographic map of a single Mn atom on Nb(110). **(c,d)** LDOS maps of the δ-states at $E = \delta_-$ **(c)** and $E = \delta_+$ **(d)**.

in the [1$\bar{1}$0] direction, since this is expected to lead to dominant hybridization of the δ-YSR state with weak coupling of all the higher-energy YSR-states like the α-state in Fig. 6.1 (a), as the interatomic distance $d = 0.467$ nm of the chain atoms is large in this direction compared to other directions.

With this knowledge, Mn_N chains of N atoms are constructed along the [1$\bar{1}$0] direction (Fig. 6.2) by controlled lateral manipulation of the Mn atoms using the STM tip as a tool. The constructed chain's magnetic moments are ferromagnetically aligned along the [1$\bar{1}$0] direction. With the proximity-induced superconducting gap from the Nb substrate, this gives us all necessary ingredients for topological superconductivity in the presence of any non-vanishing RSO [186]. The Fermi wavevector is experimentally determined to be $k_F = (0.6 \pm 0.1)\pi/d$ by identifying a peak in the Fourier transformation of the LDOS map of the surface around a single Mn impurity at the energy of the δ-YSR state. The topography of the constructed Mn_{32} chain is shown in Fig. 6.2 (b), and Fig. 6.2 (c) shows the spatially resolved deconvoluted differential tunneling conductance (dI/dV) maps on and around the chain for multiple different energies centered on the energies of different in-gap states. The states at zero energy are well localized at the ends of the chain with an additional small LDOS oscillation in the interior of the chain. In contrast, the

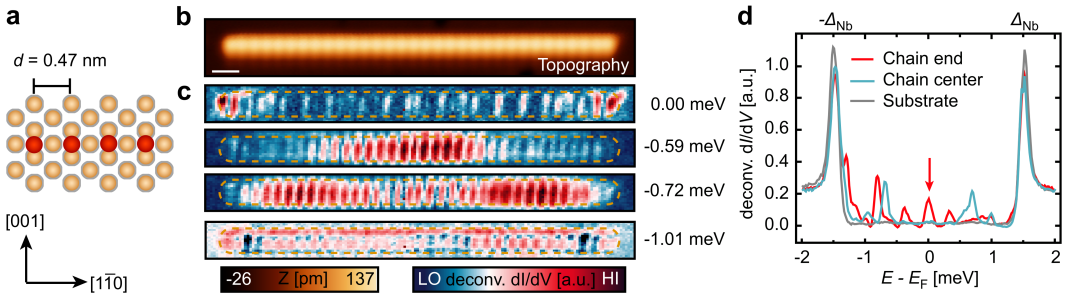

Figure 6.2: **In-gap states of Mn chains on Nb(110) along the** [1$\bar{1}$0]**-direction. (a)** Geometry of the experimentally assembled Mn atoms (red) on top of the atoms of the superconducting Nb substrate (brown). **(b)** Constant-current STM image (topography) of a Mn_{32} chain. The white scale bar corresponds to 1 nm. **(c)** Corresponding deconvoluted dI/dV maps at the indicated energies. The brown dashed lines mark the position of the chain. **(d)** Single deconvoluted dI/dV spectra measured on the chain's end, in the center, and on the Nb(110) substrate. The zero-energy peak is marked by the red arrow.

higher-energy states are distributed over the whole chain, presumably stemming from the α-YSR state. The spectra at the chain's end, the chain's center and on bare Nb(110) are shown in Fig. 6.2 (d). There is a narrow zero-energy peak localized at the ends of the chain. Peaks from finite energy states are distributed over the entire chain, as shown in Fig. 6.2 (c). Such clearly resolved zero-energy end states are typically considered as an indication for isolated Majorana modes (MMs) [13, 14, 16, 18, 45, 70, 71].

Since the chains were constructed atom by atom, all measurements could be repeated and tracked for each chain length N to probe the robustness of the zero-energy end state. From this, in Fig. 6.3 (a-f), the dI/dV along the chain (called dI/dV line profile from here on) is shown for $N = 14, 15, 16$. Similar zero-energy end states were found for $N = 14$ and $N = 16$, clearly separated from higher-energy states by a large gap $\Delta_{\mathrm{FS}} = 400$ µeV. But for $N = 15$, two states of similar strong localization, split by $E_{\mathrm{hyp}} = 300$ µeV symmetrically around E_{F}, are found instead. The observation that both ends of the chain are affected symmetrically by the addition of single atoms on one end shows that the energies of the two end modes on both sides are intertwined, and thus that the end modes are a single coherent quantum state of the chain. To further

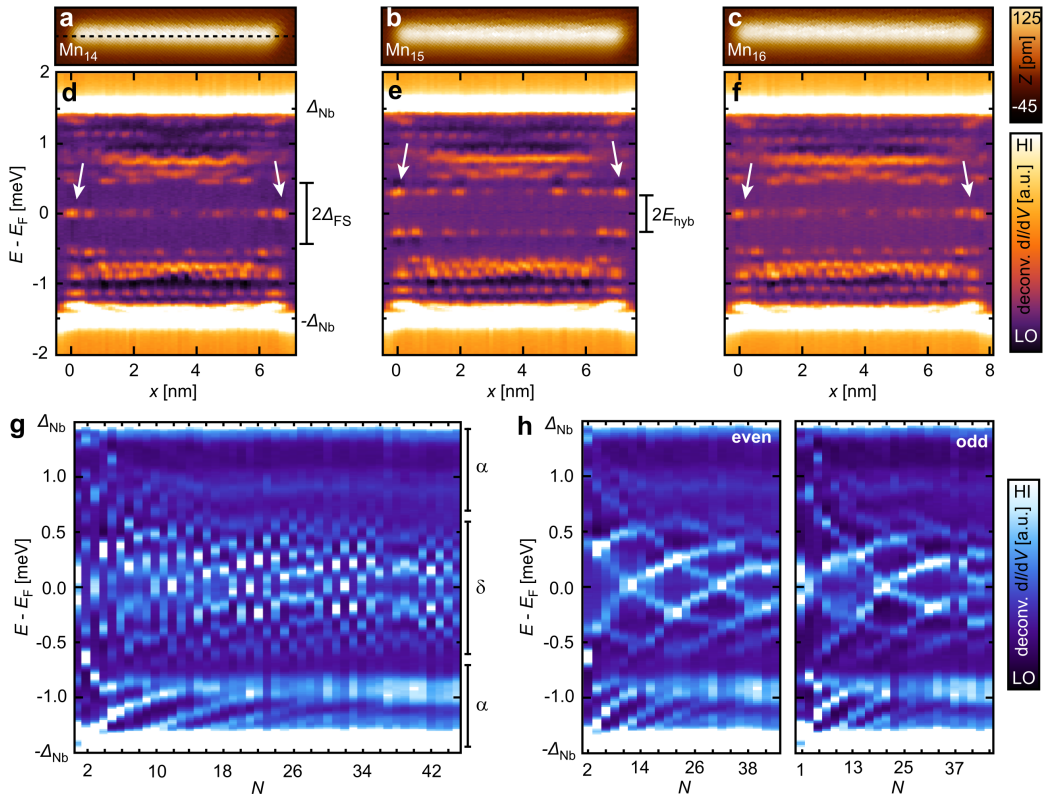

Figure 6.3: **Chain length dependence of in-gap states. (a-c)** STM topography images of Mn_N chains with $N = 14$ **(a)**, $N = 15$ **(b)**, and $N = 16$ **(c)**. **(d-f)** Corresponding deconvoluted dI/dV line profiles acquired along the longitudinal axis through the center of the three chains (as indicated by the dashed line in (a)). The edge states are marked with white arrows. **(g)** Sequence of dI/dV spectra measured on one end of the Mn_N chains for different values of N. The spectral features associated with bands from hybridizing α- and δ-states are marked on the right side. **(h)** Data set from (g) with even and odd length chains plotted into separate panels.

investigate this energy splitting, Fig. 6.3 (g) shows the deconvoluted dI/dV signal at the end of another, structurally identical chain with varying chain length N, where Mn atoms were added to one end of the chain and the dI/dV signal was measured at the opposite end of the chain. The same deconvoluted dI/dV is shown in Fig. 6.3 (h) but split into two images, one showing only even and the other only odd length chains. The energy of the state closest to E_F is modulated by a period of $\Delta N \approx 2$, but not exactly 2. This trend

continues up to the longest constructed chains of $N = 45$. Due to remaining oxygen impurities on the surface, the maximum length of ordered magnetic chains is limited to 20-25 nm. The sub-gap energies appear to change as a continuous function of N. For certain chain lengths ($N = 13, 31, 32, 42$), the energy of the end state is tuned to zero within the experimental peak width $\Delta E = 50$ μeV. In contrast, the α-states evolve into a completely narrow band, irrelevant to the topological properties. The modulation of $\Delta N \approx 2$ lets us suspect a Fermi wavevector of $k_F \approx 0.5\pi/d$, but importantly not exactly $0.5\pi/d$, which is inline with the experimentally determined Fermi wavevector discussed above. As shown in the following Sec. 6.2, these oscillating energy modes develop into isolated Majorana modes with increasing chain length N. Thus, we can interpret them as precursors of Majorana modes (PMMs) with a residual MM coupling due to finite length. In this section, we also show though that the topological protection for these end modes is weak due to a small bulk topological gap.

Next, we discuss the exclusion of other topologically trivial explanations. First, disorder is frequently discussed as a source of zero-energy states [75, 187–189]. This can be ruled out by the geometrically perfect structure of our chains. Second, generally speaking, end states can be caused by zero-dimensional features induced by local defects or localized YSR states [116–118, 190]. In our case, both ends change equally when perturbing only one end of the chain. Thus, the end state must be a collective mode of the 1D structure. The observation of this correlation is a key advantage over previous experiments, where only one end was probed [13, 14, 16, 45, 70–72]. Third, it is possible that the localization of the wavefunction closest to E_F is less pronounced than the experiment suggests. Both YSR states are predominantly located in the SC host. The measurement signal of the LDOS above the Mn chain could be suppressed in the interior of the chain and amplified at the ends of the chain [45]. In this case, the topological phase would still be non-trivial in the infinite case, though. A trivial band structure would only be compatible with the experimental data in the presence of additional low-energy bands, but experimentally all features from additional bands are well separated. This results in strong evidence that our chains indeed realize an effective one-band model in the low-energy limit.

6.2 Tight-Binding Model for Mn Chains on Nb(110)

To improve our understanding of the experimental results described above, we create a tight-binding toy model that replicates the low energy band structure and geometry of the experiment. We construct a one-dimensional ferromagnetic chain on top of two layers of a superconducting substrate, using the *Kwant* code. The Bogoliubov-de Gennes Hamiltonian of the chain reads

$$\begin{aligned} H_{\text{chain}} = &\sum_i \vec{c}_i^{\,\dagger}(-J_{\text{c}}\tau_0\sigma_z - \mu_{\text{c}}\tau_z\sigma_0 + \Delta_{\text{c}}\tau_x\sigma_0)\vec{c}_i \\ &+ \sum_{\langle i,j\rangle} \vec{c}_i^{\,\dagger}(-t_{\text{c}}\tau_z\sigma_0 + \frac{\text{i}}{2}\alpha_{\text{c}}\tau_z\sigma_y)\vec{c}_j + \text{h.c.} \end{aligned} \tag{6.1}$$

with the magnetic interaction strength J between a magnetic moment on a given site and the spin of a conducting electron, the chemical potential μ, the hopping amplitude t, the superconducting order parameter Δ, and the Nambu spinor $\vec{c}_j = (c_{j,\uparrow}, c_{j,\downarrow}, c_{j,\downarrow}^\dagger, -c_{j,\uparrow}^\dagger)$ [136]. Here, $c_{i,\sigma}^\dagger$ and $c_{i,\sigma}$ are creation and annihilation operators of fermionic states with spin σ at site i. The Pauli matrices σ and τ are connected by a Kronecker product and operate in spin and particle-hole space, respectively. Summation over nearest neighbor sites is indicated by $\langle i, j\rangle$. The two layers of a substrate with 350×15 sites in a cubic lattice structure are represented by

$$H_{\text{substrate}} = \sum_i \vec{c}_i^{\,\dagger}(-\mu_{\text{s}}\tau_z\sigma_0 + \Delta_{\text{s}}\tau_x\sigma_0)\vec{c}_i + \sum_{\langle i,j\rangle} \vec{c}_i^{\,\dagger}(-t_{\text{s}}\tau_z\sigma_0)\vec{c}_j + \text{h.c.}, \tag{6.2}$$

and the hopping between the chain and the substrate

$$H_{\text{hop}} = \sum_{\langle i_{\text{c}}, j_{\text{s}}\rangle} \vec{c}_i^{\,\dagger}(-t_{\text{cs}}\tau_z\sigma_0)\vec{c}_j + \text{h.c.}, \tag{6.3}$$

with the hopping parameter between chain and substrate t_{cs}. The parameter indices c and s denote whether a parameter corresponds to the chain c or

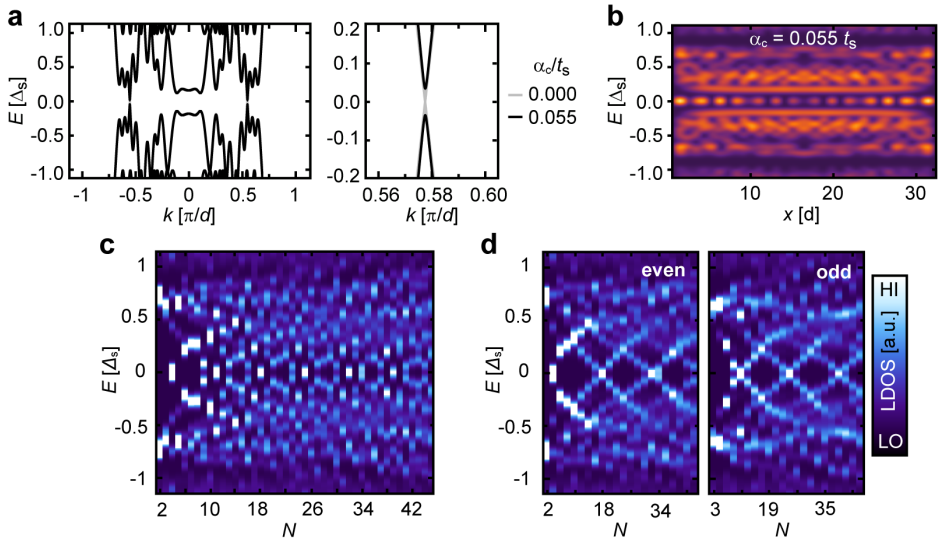

Figure 6.4: **Even-odd modulation in a magnetic chain on a substrate.** **(a)** Band structure of an infinite chain on a substrate that is infinite in the direction of the chain, with and without RSO coupling α_c in the chain as indicated on the right. **(b)** LDOS along a chain of 32 sites using the parameters from (a) and $\alpha_c = 0.055\,t_s$. **(c)** LDOS on the first chain site in Mn_N chains of different number of sites N using the parameters from (b). **(d)** Dataset from (c) with chains of odd- and even-N plotted in separate panels.

the substrate s. The complete Hamiltonian of our system is $H = H_{\text{chain}} + H_{\text{substrate}} + H_{\text{hop}}$.

To calculate the energy-dependent LDOS at site x around the Fermi edge, we calculate the 200 eigenvalues closest to $E_F = 0$ and their eigenvectors with a sparse matrix solver. Then we sum over all pairs of eigenvalues E_n and eigenvectors ψ_n

$$\text{LDOS}(E, x) \approx \sum_n |\psi_n(x)|^2 \left(\frac{-\partial f(E - E_n, T = 320\text{ mK})}{\partial E} \right), \tag{6.4}$$

with the Fermi-Dirac function $f(E, T)$ simulating the experimental thermal broadening at $T = 320$ mK [191]. Including both the particle and the hole component of the eigenvectors is justified by the particle-hole mixing value of $P(A, B) \approx 0.5$ in the experiment for the δ-YSR state, i.e., the $\mathrm{d}I/\mathrm{d}V$ amplitude below and above the Fermi edge is almost identical for the δ-YSR state in the

experiment.

Reproducing the Even-Odd Effect

We begin by reproducing the even-odd modulation of the sub-gap states, which results in a band structure with $k_F = 0.57\pi/d$ for $\alpha_\mathrm{c} = 0$. For this, we use the following set of parameters

$$\begin{aligned} &\mu_\mathrm{c} = -0.55\,t_\mathrm{s},\ \Delta_\mathrm{c} = 0,\ J_\mathrm{c} = 0.7205\,t_\mathrm{s},\ t_\mathrm{c} = 0.55\,t_\mathrm{s}, \\ &\mu_\mathrm{s} = -2\,t_\mathrm{s},\ \Delta_\mathrm{s} = 0.13\,t_\mathrm{s},\ t_\mathrm{cs} = 0.7\,t_\mathrm{s}. \end{aligned} \tag{6.5}$$

Calculating the topological invariant of the system [5], we find that the system is non-trivial for any non-vanishing RSO coupling α_c. By adding an explicit RSO term $\alpha_\mathrm{c} = 0.55\,t_\mathrm{s} = 0.42\,\Delta_\mathrm{s}$ in the chain, the band structure becomes gapped (Fig. 6.4 (a)). We calculate the band structure by taking a vertical slice as a unit cell, employing periodic boundaries in the chain direction and changing to k-space with a Fourier transformation. As shown in Fig. 6.4 (b), we find localized PMMs in a chain of $N = 32$. As in the experiment, these PMMs show a strong energy splitting with varying chain length as shown in Fig. 6.4 (c,d), which is modulated by a period of $\Delta N \approx 2$ as in the experiment.

Difference in Localization between One- and Three-Dimensional Models

The good localization of the PMMs despite strong, chain-length dependent energy splitting is counterintuitive. To gain a better understanding of this phenomenon, we compare our 3D model to a pure 1D model. When setting $t_\mathrm{cs} = 0$, we get an effective 1D model, as the chain is decoupled from the substrate. To account for the lack of proximity-induced superconductivity, we set $\Delta_\mathrm{c} = \Delta_\mathrm{s} = 0.13\,t_\mathrm{s}$ only in the 1D model. The other parameters remain the same as above. To quantify the localization of the low-energy modes, we introduce the ratio of the LDOS on the first site and the average LDOS in the

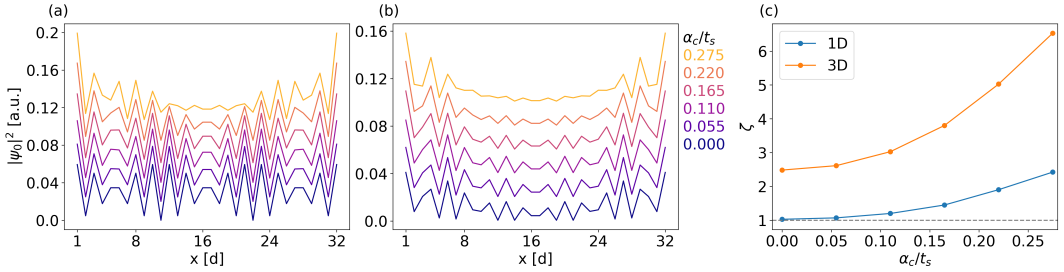

Figure 6.5: **Localization for the 1D and 3D model with increasing RSO. (a,b)** Wavefunctions of the lowest energy state in the **(a)** 1D model and **(b)** 3D model for multiple different α_c. **(c)** Localization ζ with respect to the RSO coupling strength α_c. The parameters for the tight-binding models are $J_c = 0.7205\ t_s$, $t_c = 0.55\ t_s$, $\mu_c = -0.55\ t_s$, $\mu_s = -2\ t_s$, and $\Delta_s = 0.13\ t_s$. The effective 1D model uses $t_{cs} = 0$ and $\Delta_c = 0.13\ t_s$ to account for the lack of proximity-induced superconductivity due to vanishing interaction with the superconducting substrate. The 3D model uses $t_{cs} = 0.7\ t_s$.

chain's bulk,

$$\zeta = \frac{\mathrm{LDOS}(E = 0,\ x = 1)}{2\mathrm{L\bar{D}OS}(E = 0,\ 8 < x < 25)} \tag{6.6}$$

of a chain with $N = 32$. The LDOS is symmetric. Thus, it is equivalent to using the last site of the chain instead of the first one. Fig. 6.5 shows the wavefunctions of the low-energy modes for the effective 1D model ($t_{cs} = 0$) and the 3D model ($t_{cs} = 0.7\,t_s$) and how their localization ζ scales with respect to increased RSO coupling constant α_c. The localization for chains coupled to the substrate is consistently better than for those that are purely 1D. Similar findings were reported using a model for Fe chains on Pb [67]. For the 3D model, some localization even happens for vanishing RSO $\alpha_c = 0$. The stronger localization for the 3D model can be explained by the broken inversion symmetry at the surface [192].

Chain Length Dependence and Influence of RSO on Majorana Splitting

It is important to note that the energy scale of the topological protection of MMs in an infinitely long chain is only of the size of the bulk topological gap Δ_p, which is very small compared to the bulk substrate energy gap Δ_s in this system

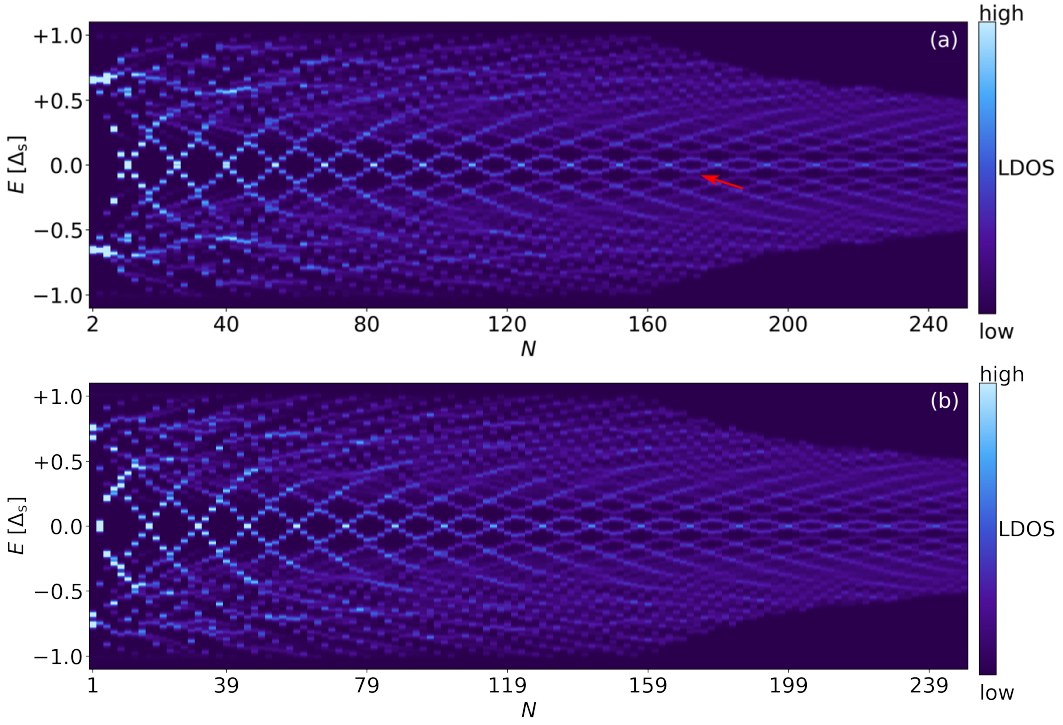

Figure 6.6: **LDOS of very long chains** for **(a)** even length chains and **(b)** odd length chains, using the parameters from Eq. (6.5) and $\alpha_c = 0.055\, t_s$. The temperature for the Fermi-Dirac function has been halved to $T = 160$ mK to increase visibility. The red arrow marks the apparent avoided crossing. In the calculations, only the 200 eigenvalues closest to the Fermi energy $E_F = 0$ were considered to save computation time. This is the cause for the empty areas for $N > 160$.

($\Delta_p = 0.0048\, t_s = 0.037\, \Delta_s$). Most importantly, it is smaller than the observed energy splitting E_{hyp} of the PMMs, which is smaller than the finite-size gap Δ_{FS}. In this case, the p-wave pairing Δ_p manifests as an apparent avoided crossing of the lowest- and second-lowest-energy states (see arrows in Fig. 6.6). These avoided crossings are too small to be detected within the experimental energy resolution. It has been shown that the long-range interactions of MMs are inversely related to Δ_p [193], i.e., larger bulk topological gaps lead to a faster exponential decay of the Majorana wavefunction. Our results imply that the observation of a well-localized zero-energy end state in a finite-size topological superconductor does not directly imply that the corresponding MMs are non-

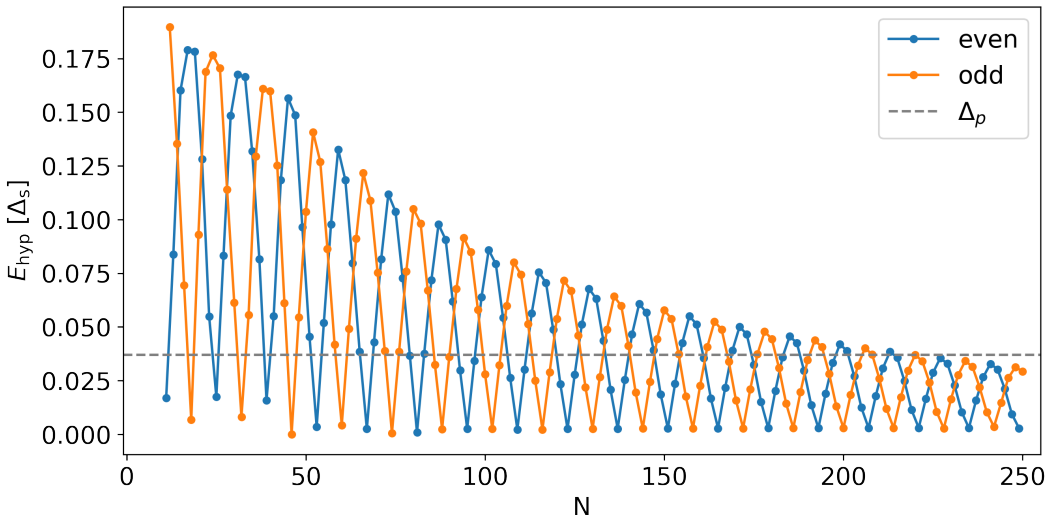

Figure 6.7: **Energy splitting E_{hyp} in long chains.** Same parameters as in Fig. 6.4. The energy splitting E_{hyp} is plotted with respect to the chain length and compared to the topological gap Δ_p.

interacting under the influence of small perturbations. As shown in Fig. 6.7, we expect the energy oscillation of the end modes to converge to energies below Δ_p only for $N > 227$ (~ 106 nm), which could not be experimentally realized due to remaining oxygen on the Nb(110) surface. It is important to note, however, that this convergence length is highly dependent on α_c, as an increase in α_c causes the convergence to speed up and increase Δ_p at the same time. For example, for $\alpha_c = 0.11\, t_s$, E_{hyp} converges to below Δ_p at $N \approx 100$. As α_c cannot be directly measured in this experiment, it is difficult to make definitive conclusions on the critical chain length, but we can rule out the case of $\alpha_c = 0$, since previous studies on Mn/Nb(110) found significant RSO coupling with observable effects in this system [19, 194]. Thus, isolated Majorana modes are expected in long chains.

The effect of increasing RSO coupling α_c in the chain is shown for chain length up to $N = 150$ in Fig. 6.8. For vanishing $\alpha_c = 0$, only conventional bulk states are present. The topological index is not well defined in this case, as the system is entirely gapless. For increasing α_c, the lowest energy states separate more and more clearly from the higher energy states. This separation

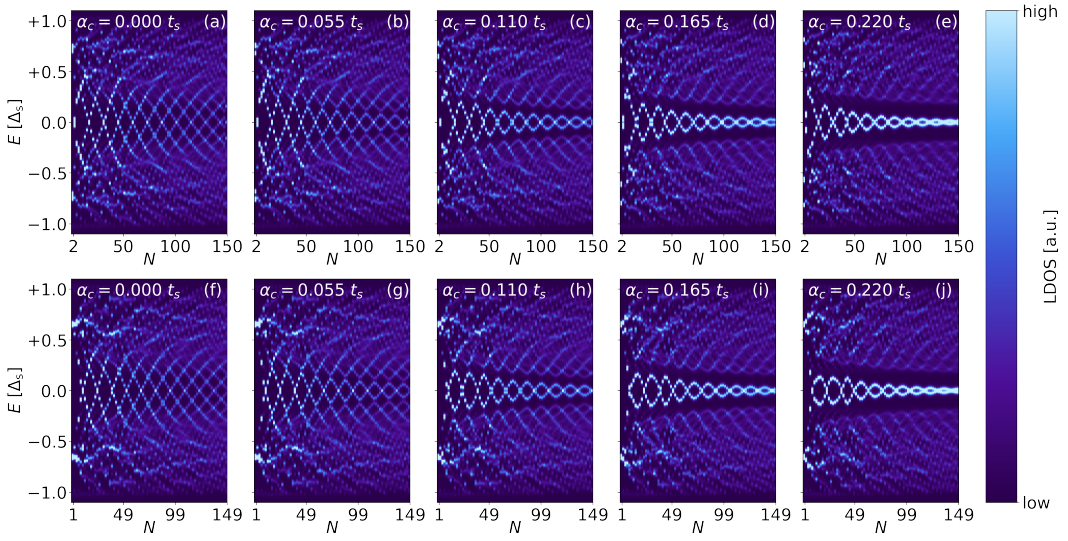

Figure 6.8: **Influence of RSO coupling**. Same parameters as in Fig. 6.4 besides changes in α_c as noted in the panels. **(a-e)** even and **(f-j)** odd length chains. The temperature for the broadening reduced to $T = 160$ mK to increase visibility.

is already visible for very small values of α_c, in agreement with the bulk-boundary correspondence [195]. Larger values for α_c lead to an increase in the topological gap Δ_p and faster convergence to zero energy for the lowest-energy states. This inverse correlation between Δ_p and the convergence length is expected [193]. Larger superconducting gaps Δ_p lead to faster convergence of the lowest-energy states towards zero energy.

Lastly, we investigate the overlap of the Majorana modes. For this, we transform the wavefunction into the standard Majorana basis

$$\gamma_{+,j} = \frac{1}{\sqrt{2}}\left(c_j^\dagger + c_j\right) \quad \text{and} \quad \gamma_{-,j} = \frac{1}{i\sqrt{2}}\left(c_j^\dagger - c_j\right). \tag{6.7}$$

The absolute value of the wavefunction and the Majorana decomposition of the lowest energy state along the chain are shown in Fig. 6.9 for multiple chain lengths. For very short chains with an energy peak close to zero ($N = 32$), we find strongly delocalized Majorana modes with peaks at both ends of the chain. Similarly, there is still a strong overlap of the Majorana wavefunctions for $N = 100$. This strong overlap is the cause for the weak protection of

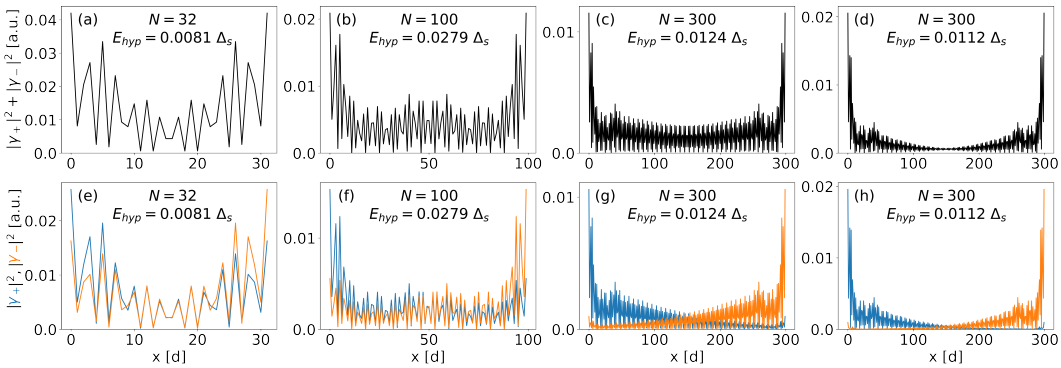

Figure 6.9: **Majorana overlap.** Upper row: Absolute square of the lowest-energy (E_{hyp}) wavefunction along finite chains of length 32, 100, and 300. Lower row: Separation of the wavefunction into the standard Majorana basis γ_+ (blue) and γ_- (orange). **(a-c, e-g)** Same parameters as in Fig. 6.4. In **(d)** and **(h)** the RSO coupling in the chain α_{c} has been doubled.

the Majorana modes against changes in chain length. For long chains ($N = 300$), the two Majorana wavefunctions can be well separated into two isolated Majorana modes. Finally, in Fig. 6.9 (d,h) a larger α_{c} is used (double compared to the previous data), which causes the Majorana wavefunctions to decay much faster and lead to much more isolated Majorana modes.

6.3 Conclusions and Outlook

In this chapter, the first simultaneous measurement of zero-bias peaks in a hard SC gap on both ends of defect-free chains has been analyzed. The experimental data is well aligned with the theoretical models and strongly indicates the presence of hybridizing Majorana modes in Mn chains on Nb(110) in the $[1\bar{1}0]$ direction. The theoretical modeling allows us to gain insight into what happens beyond the maximal chain length achieved in the experiment and strongly indicates that these precursors of Majorana modes will eventually converge to well isolated Majorana modes for sufficient chain lengths. Despite that, only a small topological gap is predicted for the infinite system, which would lead to only weakly protected Majorana modes even in the limit of very long chains with isolated Majorana modes. Our calculations show that enhancing the

RSO coupling would lead to further improvements in the localization, reduced interactions of the MMs, and an increased topological gap Δ_p. Experimentally, this could be achieved in numerous ways. A different superconducting host might yield larger spin-orbit coupling in the chains, heavy-metal interlayers are known to enhance spin-orbit coupling, and there are also proposals for synthetic spin-orbit interactions [8, 31, 196, 197]. The presented results mark a milestone in the quest for the experimental realization of isolated Majorana zero modes, but also demonstrate the importance of a large topological gap Δ_p for realizing strongly protected Majorana modes, which adds a constraint on future experiments.

Chapter 7

Machida-Shibata States in Ag Corrals on a Ag Island with Proximity-Induced Superconductivity from Bulk Nb

In this chapter, we focus on tight-binding models that assist the understanding of experimental findings on Ag corrals on Ag islands on bulk Nb [4]. Parts of the material presented in this section are published in the article [4]:

> Lucas Schneider, Khai Thât-Tôn, Ioannis Ioannidis, Jannis Neuhaus-Steinmetz, Thore Posske, Roland Wiesendanger, and Jens Wiebe
>
> *Proximity superconductivity in atom-by-atom crafted quantum dots*
>
> Nature **621**, pages 60–65 - Published 16 August 2023
>
> Reproduced with permission from Springer Nature.

We begin by briefly summarizing the experimental findings in Sec. 7.1. Then, in Sec. 7.2, we focus on a simple tight-binding model with a single impurity to qualitatively reproduce the central experimental finding. After that, in Sec. 7.3, we move to a 3D model that correctly resembles the geometry of the experiment. Lastly, we summarize our results and provide an outlook for future research in Sec. 7.4.

Work Sharing

The experimental measurements in this chapter were done by Lucas Schneider and Khai Thât-Tôn. I performed the tight-binding calculations presented in

this chapter. The original publication [4] also contains calculations done by Ioannis Ioannidis and Dr. Thore Posske, which are not shown here.

7.1 Experimental Results

Here, we summarize the experimental results to provide context for the calculations done in the following sections. In the experiment, thin Ag(111) islands with a thickness of 12 nm are grown on bulk Nb(110) as depicted in Fig. 7.1 (a). On top of these islands, rectangular walls made out of Ag adatoms are constructed using the tip of an STM as a tool as depicted in Fig. 7.1 (c) and (d). The system is investigated with scanning tunneling microscopy and scanning tunneling spectroscopy (see Sec. 3.8). For the measurement, a superconducting Nb tip is used to enhance the energy resolution. This causes a shift in spectral features to higher energies of the superconducting gap Δ_{tip} of the tip. Thus, states at the sample's Fermi energy E_{F} are found at a bias voltage $e{\cdot}V = \pm\Delta_{\mathrm{tip}}$. The islands are about $d_{\mathrm{Ag}} = 12$ nm thick and the proximity to the superconducting Nb(110) opens a SC gap of $2\Delta_{\mathrm{s}} = 2.7$ meV in the bulk Ag(111). On top of the Ag(111) islands, surface electrons are scattered, forming a visible wavy pattern with a wavelength of a few lattice constants. These surface electrons are laterally confined by the wall of Ag atoms to a corral mode, which we refer to as a *quantum dot* (QD), here. Within these walls, spin degenerate eigenmodes of energy E are found, which can be pitched by adjusting the size of the Ag box. In this experiment the size adjustment is done by keeping the width $L_y = 9.1$ nm fixed while tuning the length L_x by pushing one of the walls inwards using the STM tip as depicted in Fig. 7.1 (c,d). The eigenmodes are mapped in Fig. 7.1 (e) by measuring the differential tunneling conductance $\frac{\mathrm{d}I}{\mathrm{d}V}(x, y, E)$ at particular bias voltages $e \cdot V = E$. The resulting patterns closely resemble the eigenmodes of a 2D rectangular box potential with infinite walls. As L_x is changed, the confinement conditions of the eigenmodes change, causing a shift in the eigenenergies of the QD. When shortening the box from 24 nm to 16.4 nm, individual states are shifted to higher energies, and the linewidth Γ of the eigenmodes, and thus their coupling $V_{\mathrm{c}} \propto \sqrt{\Gamma}$ to the bulk SC electrons

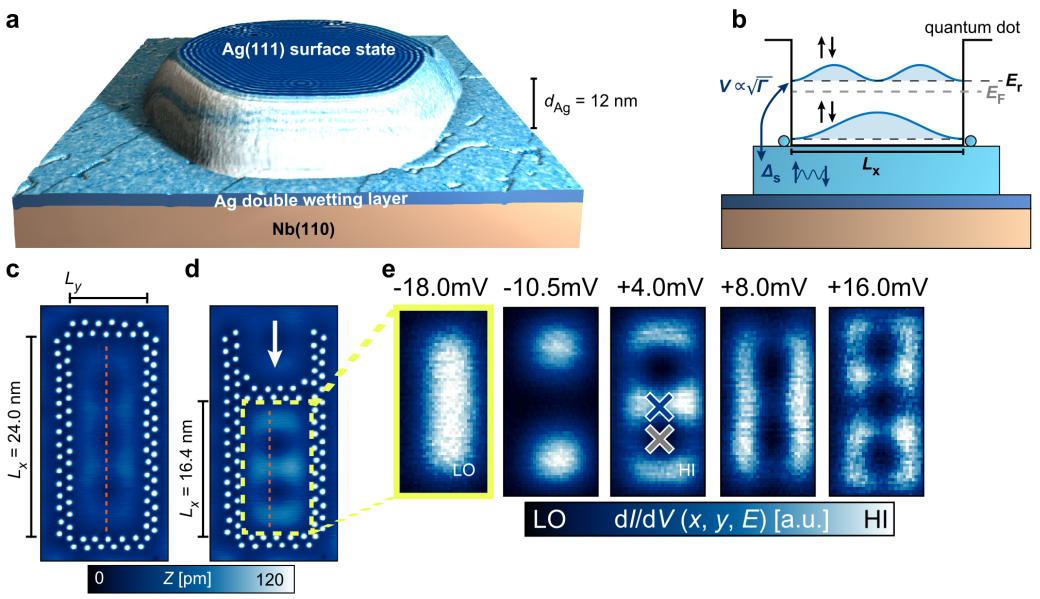

Figure 7.1: **Experimental setup.** **(a)** 3D rendering of the constant-current STM topography of a Ag island with a thickness of 12 nm, where the simultaneously measured $\mathrm{d}I/\mathrm{d}V$ signal is used as the texture of the model. **(b)** Sketch of the experimental setup with the QD walls laterally confining the surface-state electrons into QD eigenmode energies E_r. The eigenmodes couple to the SC substrate Δ_s with a coupling strength $V \propto \sqrt{\Gamma}$. **(c)** Constant-current STM image of a rectangular QD with side lengths L_x and L_y consisting of 44 atoms. **(d)** Constant-current STM image of the same structure with one of the walls moved as indicated by the arrow. **(e)** Constant-height $\mathrm{d}I/\mathrm{d}V$ maps at bias voltages indicated in the respective panels, measured in the interior of the QD in panel (d) (area marked by the dashed yellow line). All panels are 15×7.5 nm^2 in size.

increases. This is a well-known effect caused by an increase in surface-bulk scattering because of the smaller corral [86, 198]. By further tuning L_x, these effects are used to continuously push the QD eigenmodes with different couplings V_c through E_F. When measuring the $\mathrm{d}I/\mathrm{d}V$ spectrum, as shown in Fig. 7.2 (a), at the spatial position of a minima of a low energy eigenmode, i.e., an eigenmode close to E_F (gray cross in Fig. 7.1 (e)), sharp peaks are observed at bias voltages at $e \cdot V = \pm(\Delta_\mathrm{s} + \Delta_\mathrm{tip})$, and an absence of conductance at lower energies confirms that the bulk gap of Ag(111) is fully developed. When

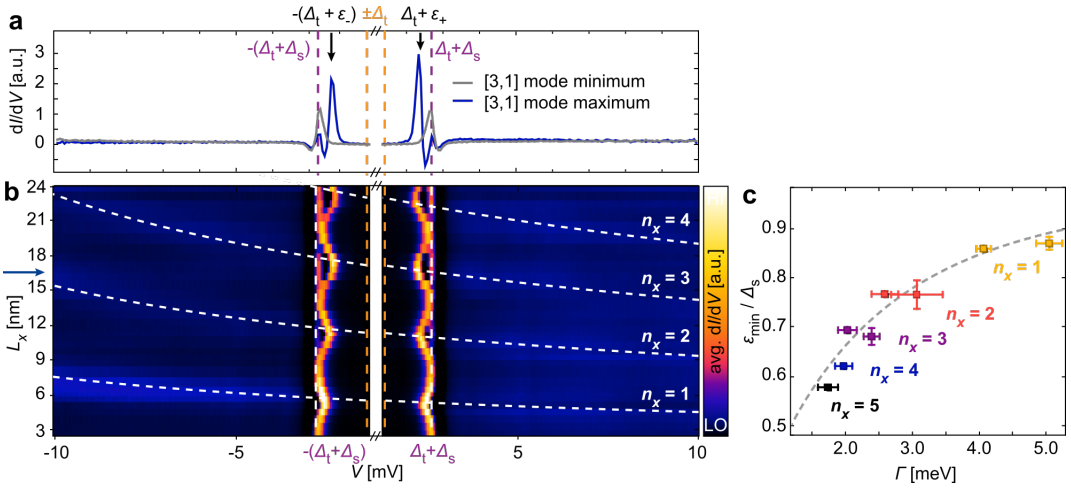

Figure 7.2: **In-gap states of near-zero-energy pitched QD eigenmodes.** **(a)** $\mathrm{d}I/\mathrm{d}V$ spectra measured at two different positions (gray and blue crosses in Fig. 7.1 (e). The values of the tip's superconducting gap $\pm\Delta_t$ and the sum $(\Delta_t + \Delta_\mathrm{s})$ with the proximity-induced Ag bulk gap Δ_s are marked by dashed orange and purple lines, respectively. In-gap states with energies $\pm(\Delta_t + \epsilon_\pm)$ are marked by black arrows. **(b)** Evolution of averaged $\mathrm{d}I/\mathrm{d}V$ spectra from $\mathrm{d}I/\mathrm{d}V$ line profiles measured along the central vertical axis (dashed orange line in Fig. 7.1 (c,d)) of differently sized QDs as a function of L_x. The dashed white lines mark the evolution of eigenmodes with $n_y = 1$ and $n_x = \{1, 2, 3, 4\}$ obtained from fitting the $\mathrm{d}I/\mathrm{d}V$ spectra at energies outside the gap [4]. The blue arrow marks the length of the QD used in (a). **(c)** Linewidths Γ of different QD eigenmodes extracted from fitting data from different QDs to Lorentzian peaks at energies outside the gap [4], which are compared with the minimal energies of in-gap states found when $E_r \approx 0$ (error bars are the standard deviations extracted from fitting the data). The dashed gray line shows the expected theoretical relation for a spin-degenerate level coupled to a SC bath [89].

measuring the $\mathrm{d}I/\mathrm{d}V$ spectrum on a maximum of the QD eigenmode closest to E_F (blue cross in Fig. 7.1 (e)), a pair of sharp electronic states is found at particle-hole symmetric energies $\pm(\Delta_\mathrm{tip} + \epsilon_\pm)$ between the coherence peaks. Fig. 7.2 (b) shows the spectra of eigenmodes with respect to L_x. Eigenmodes with quantum numbers $[n_x, 1]$ follow well-known L_x^{-2} behavior outside of the superconducting gap. The peaks at $\pm(\Delta_\mathrm{s} + \Delta_\mathrm{tip})$ remain the same for all L_x. In-gap states of varying energies $\pm(\Delta_\mathrm{tip} + \epsilon_\pm)$ appear whenever a QD eigenmode

energy E_r approaches E_F. We observe the lowest $\epsilon_\pm$ (i.e. in-gap state furthest into the gap) when E_r would cross E_F if extrapolated from outside the gap. We take this minimum value ϵ_min and compare it with the estimated energetic broadening Γ outside of the gap in Fig. 7.2 (c), which shows that the Γ of the eigenmodes closest to E_F decreases with increased QD size, as n_x relates to the QD size. As one of the main experimental results, this experiment shows a clear correlation between ϵ_min and $\Gamma \propto V_\mathrm{c}^2$. Thus, for increased couplings Γ of a zero-energy eigenmode to the substrate SC, ϵ_min is shifted towards the gap edge Δ_s.

The observation of these in-gap states is surprising. Usually one would expect in-gap states to either stem from magnetic atoms or unconventional superconductivity. Ag is a non-magnetic material, Nb is a conventional superconductor, and the proximity effect induced in a normal metal with negligible spin-orbit coupling is not expected to cause unconventional pairing. But theoretically, it has been shown in 1972 by Machida and Shibata that there is always a sub-gap solution for a spin-degenerate level coupled to a superconducting bath due to resonance scattering [89, 119]. Machida and Shibata used the Hamiltonian

$$H = \sum_{\vec{k},\sigma} \epsilon_{\vec{k}} c^\dagger_{\vec{k},\sigma} c_{\vec{k},\sigma} + \sum_{\vec{k},\sigma} V_\mathrm{c} (c^\dagger_{\vec{k},\sigma} d_\sigma + d^\dagger_\sigma c_{\vec{k},\sigma}) + \sum_\sigma E_r d^\dagger_\sigma d_\sigma - \Delta_\mathrm{s} \sum_k (c^\dagger_{\vec{k},\uparrow} c^\dagger_{-\vec{k},\downarrow} + c_{-\vec{k},\downarrow} c_{\vec{k},\uparrow}), \tag{7.1}$$

where $c_{\vec{k},\sigma}(c^\dagger_{\vec{k},\sigma})$ and $d_\sigma(d^\dagger_\sigma)$ are the annihilation(creation) operators of the superconducting bath electrons and the localized level with spin σ, respectively. $\epsilon_{\vec{k}}$ denotes the normal electronic dispersion of the superconductor, $V_\mathrm{c} \propto \sqrt{\Gamma}$ is the coupling strength of the localized level to the bath, and Δ_s is the order parameter of the s-wave superconductivity in the bath. They showed that there is always an Andreev bound state at in-gap energies for non-vanishing V_c. In the following, we refer to this special kind of Andreev bound states as Machida-Shibata states (MSSs). MSSs have not been observed previously, mostly because they are expected to be found very close to the coherence peaks, rendering it impossible to be experimentally detected. In the system at hand though, the coupling of the surface is so small that the MSSs move far enough into the gap to be distinguishable from the coherence peaks.

For the particle-hole-mixing, we find that maximal particle-hole mixing is achieved exactly when $\epsilon_{\pm} = \epsilon_{\min}$. This further supports that $\epsilon_{\min}$ can be interpreted as proximity-induced superconducting pairing Δ_{ind} in the QD resonance level. Moving away from $\epsilon_{\min}$ by either increasing or decreasing L_x lowers particle-hole mixing.

In Ag on Ag(111) on Nb(110), we find a negligible electron-electron interaction energy U, $U \ll \Delta_{\text{s}} \sim \Gamma \ll \delta E_r$ with δE_r being the energy separation of the QD eigenmodes, due to electron-electron interactions being largely suppressed by screening in metallic QDs. Thus, the QD can be described by spin-degenerate single-particle eigenmodes and we can reasonably model the system with a spin-degenerate single-particle tight-binding model.

7.2 Replicating Machida-Shibata States with a Single Quantum Dot

In this section, we gain a first understanding of the experiment by qualitatively reproducing non-magnetic in-gap states in a geometrically simplified tight-binding model. We model a triangular monolayer SC with 20×20 atoms and a single quantum dot (or adatom) connected to three surface atoms in the middle, like for a hollow-site adsorption. This quantum dot represents a surface state inside of the corral. It is coupled to the SC layer with a hopping term t_{QD} that is weaker than the intralayer hopping t, and its chemical potential μ_{QD} is varied, representing the change in eigenenergies of the particle-in-a-box state by changing the size of the box. For the monolayer, we use a chemical potential of $\mu = 0$. For the quantum dot, we scan the chemical potential μ_{QD} through energies close to the Fermi energy $E_{\text{F}} = 0$. We use a gap of $\Delta = 0.5\,t$, which is significantly larger than in the experiments to account for the limited energy resolution caused by the small bulk. The employed Hamiltonians are

$$H_{\text{surface}} = \sum_i \vec{c}_i^{\,\dagger}(-\mu\tau_z\sigma_0 + \Delta\tau_x\sigma_0)\vec{c}_i + \sum_{i,j} \vec{c}_i^{\,\dagger}(t\tau_z\sigma_0)\vec{c}_{i+1} + \text{h.c} \tag{7.2}$$

for the surface and

$$H_{\mathrm{QD}} = \vec{c}^{\dagger}_{\mathrm{QD}}(-\mu_{\mathrm{QD}}\tau_z\sigma_0)\vec{c}_{\mathrm{QD}} + \sum_{i\in\text{QD's n.n.}} \vec{c}_i^{\,\dagger}(t_{\mathrm{QD}}\tau_z\sigma_0)\vec{c}_{\mathrm{QD}} + \mathrm{h.c} \tag{7.3}$$

for the quantum dot and its coupling to the SC monolayer with the basis $\vec{c}_i = (c_{i,\uparrow}, c_{i,\downarrow}, c^{\dagger}_{i,\downarrow}, c^{\dagger}_{i,\uparrow})^T$, and the Pauli matrices τ and σ connecting particle-hole and spin space, respectively. The sum in Eq. (7.3) runs over the nearest neighbors of the QD in the surface.

In Fig. 7.3, the spectrum with respect to the chemical potential of the quantum dot μ_{QD} is shown for different coupling strengths t_{QD}. For $t_{\mathrm{QD}} = 0.3\,t$, we find a good agreement with the experimental results. This demonstrates that in-gap states can indeed be found without magnetic adatoms as predicted by Machida and Shibata [89]. We observe an anti-crossing behavior close to $\mu_{\mathrm{QD}} = E_{\mathrm{F}}$ and find a proximity-induced gap in the QD state. Like in the experiment, we find maximal particle-hole mixing when $E = E_{\mathrm{min}}$. The multiple states experimentally found in a single corral cannot be represented by a single QD, as it does not have multiple eigenmodes like the particle-in-a-box states found in the experiment. For strong coupling, the in-gap state is energetically very close to the coherence peak of the superconducting bulk.

While this model is extremely simplified compared to the experiments, it still demonstrates that sharp in-gap states can be produced by non-magnetic adatoms. Similar findings have been made by Machida and Shibata [89], who predicted these kinds of in-gap states but also predicted that they are invisible in experimental settings due to large couplings to the bulk causing them to be too close to the SC peaks to be measurable.

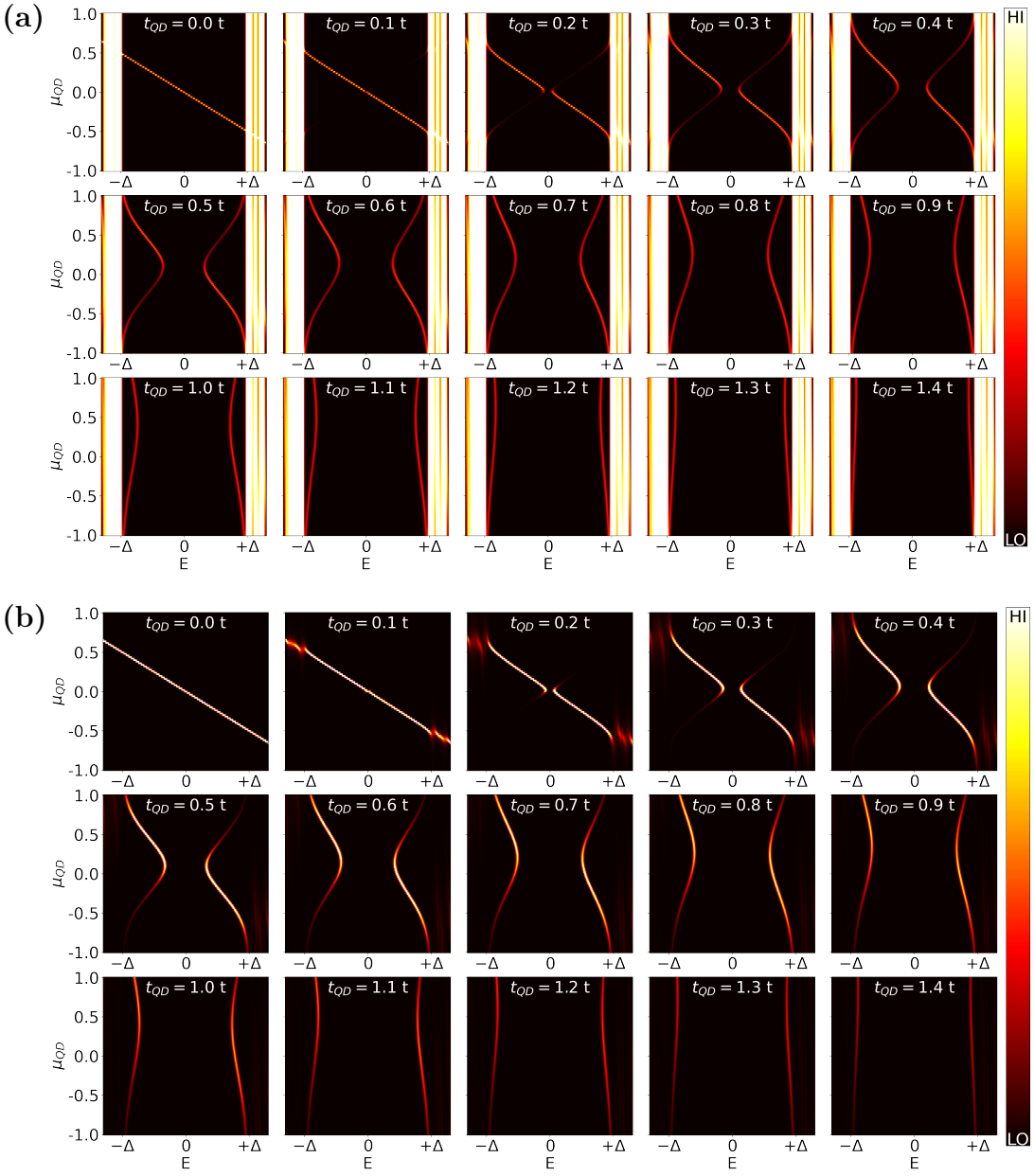

Figure 7.3: **Energy spectrum of a single quantum dot.** The color denotes the density of states with respect to the energy E and the chemical potential of the QD μ_{QD} for different coupling strength between the QD and the surface t_{QD} as denoted at the top of each panel. The DOS is summed over **(a)** all sites of the system and **(b)** only considering the QD. The color intensity in (b) is five times higher than in (a) for better readability. The DOS is also calculated only considering electronic states, i.e., discarding hole states.

7.3 Geometrically Correct Model for Ag on Ag

Next, we introduce a geometrically correct model of the experiment at hand. We employ a 3D tight-binding model following the sketch in Fig. 7.4 (a). We have one superconducting triangular lattice layer (dark gray), modeling the SC substrate with 150×150 sites and a lattice constant of $a = 0.25$ nm. On top of that, another triangular lattice of normal conducting sites with no intrinsic superconducting pairing (light gray) is placed, representing the Ag(111) surface states, also with 150×150 sites, with each atom being placed on hollow-sites of the underlying layer. On top of the surface layer, a rectangle of non-magnetic adatoms (dark blue) is arranged, representing the Ag adatoms of the experimental setup. The dimensions of the box are described by $L_x \times L_y$ and the adatoms are chosen to occupy the nearest hollow-adsorption sites along the rim of the rectangle. The SC layer is weakly coupled to the surface layer by a hopping term $t_{\text{sc-ss}}$ (blue lines). Other than that, all nearest neighbors are coupled by the same hopping strength, including the hopping between the adatoms and the surface layer.
Our tight-binding model is described by the Hamiltonian

$$H = H_{\text{sc}} + H_{\text{ss}} + H_{\text{ad}} + H_{\text{sc-ss}} + H_{\text{ad-ss}} \tag{7.4}$$

with

$$H_{\text{sc}} = \sum_{i_{\text{sc}}} c_i^\dagger(-\mu_{\text{sc}}\tau_z\sigma_0 + \Delta_{\text{sc}}\tau_x\sigma_0)c_i + \sum_{\langle i_{\text{sc}}, j_{\text{sc}}\rangle} \left(c_i^\dagger(-t_{\text{sc}}\tau_z\sigma_0)c_j + \text{h.c.}\right) \tag{7.5}$$

for the SC layer,

$$H_{\text{ss}} = \sum_{i_{\text{surface}}} c_i^\dagger(-\mu_{\text{ss}}\tau_z\sigma_0)c_i + \sum_{\langle i_{\text{ss}}, j_{\text{ss}}\rangle} \left(c_i^\dagger(-t_{\text{ss}}\tau_z\sigma_0)c_j + \text{h.c.}\right) \tag{7.6}$$

for the surface state layer,

$$H_{\text{sc-ss}} = \sum_{\langle i_{\text{sc}}, j_{\text{ss}}\rangle} c_i^\dagger(-t_{\text{sc-ss}}\tau_z\sigma_0)c_j + \text{h.c.} \tag{7.7}$$

for the coupling between the SC and the surface state layer,

$$H_{\text{ad}} = \sum_{i_{\text{ad}}} c_i^\dagger(-\mu_{\text{ad}}\tau_z\sigma_0)c_i \tag{7.8}$$

for the onsite potential of the adatoms, and

$$H_{\text{ad-ss}} = \sum_{\langle i_{\text{ad}}, j_{\text{ss}}\rangle} c_i^\dagger(-t_{\text{ss}}\tau_z\sigma_0)c_j + \text{h.c.} \tag{7.9}$$

for the coupling between the adatoms and the surface. The employed basis is the Nambu spinor $\vec{c_i} = (c_{i,\uparrow}, c_{i,\downarrow}, c_{i,\downarrow}^\dagger, c_{i,\uparrow}^\dagger)^T$, where $c_{i,\sigma}^\dagger$ and $c_{i,\sigma}$ are creation and annihilation operators of fermionic states with spin σ at site i. Summation over nearest neighbor sites is indicated by $\langle i, j\rangle$. The variables of the system are the chemical potential μ, the hopping strength t, and the superconducting order parameter Δ with the indices sc, ss, and ad to denote the respective layer. Attached to an index i, these indices denote the summation over the sites of the respective layer. The Pauli matrices τ_m and σ_m operate in particle-hole- and spin-space, respectively, and are connected by a Kronecker product. The Hamiltonian is built using *kwant* [172].

To calculate the energy-dependent local density of states $\text{LDOS}(E, x)$ around the Fermi edge, we calculate the 2200 eigenvalues and eigenvectors of H closest to the Fermi edge with a sparse matrix solver. To simulate thermal broadening present in the experiment, we sum over the pairs of eigenvalues E_n and eigenvectors Ψ_n

$$\text{LDOS}(E, x) = \sum_n |\Psi_n(x)|^2 e^{-(E-E_n)^2/(\delta E_{\text{thermal}})^2} \tag{7.10}$$

with $\delta E_{\text{thermal}} = 0.025\,\Delta_{\text{sc}}$. From this, we calculate the DOS of the surface state by summing over the surface layer sites within the rectangle which are at least three sites away from the rectangle.

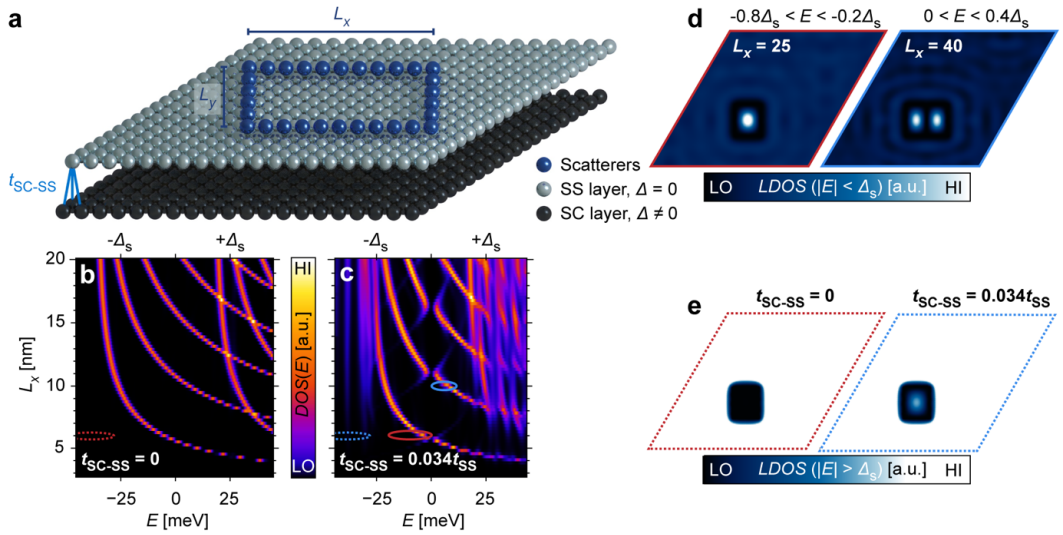

Figure 7.4: **Tight-binding modeling of proximity-induced pairing in QDs.** **(a)** Sketch of the geometry of the tight-binding model for Ag corrals on Ag islands on superconducting Nb. Each sphere represents one atomic site. While the SC layer features finite SC pairing terms, the surface state layer is a normal metal. Pairing in the surface state layer is proximity-induced via coupling $t_{\text{sc-ss}}$ between the layers (indicated by blue lines). The QD is built by scattering sites on the surface aligned in a rectangular geometry of length L_x and width L_y. **(b,c)** Evolution of the energy-dependent DOS evaluated within the QD for varying length L_x and fixed width L_y of 7.5 nm (30 sites) for (b) zero coupling to the SC layer and (c) finite coupling $t_{\text{sc-ss}} = 0.034\, t_{\text{ss}}$ to the SC layer. **(d)** Spatially resolved LDOS patterns in the surface state layer evaluated at in-gap energies and integrated over the energy ranges as indicated above the two panels for QDs of 25×30 (6.25×7.5 nm^2) in the left panel and 40×30 sites (10.0×7.5 nm^2) in the right panel (again $t_{\text{sc-ss}} = 0.034\, t_{\text{ss}}$). The frame colors of the panels correspond to the solid ellipses in panel (c), highlighting which of these eigenstates are shown. **(e)** Spatially resolved LDOS at energies outside the superconducting gap (integrated from $-2.00\,\Delta_s$ to $-1.12\,\Delta_s$) for zero coupling (left panel) and finite coupling (right panel) to the SC layer. The frame colors of the panels correspond to dashed ellipses in panels (b) and (c).

Adjusting Parameters

We need to find a set of parameters that reproduces the experimental data. First, we set $t_{\text{ss}} = 1$ as our unit of energy without loss of generality. Later, we estimate the value of t_{ss} in eV from the experimental data to make it more acces-

sible. In the experiment, a Fermi wavevector of $k_F \sim 0.5\pi/\text{nm}$ has been found with a Fourier transformation of a spectroscopic line profile on the Ag(111) island. Using periodic boundaries in H_{ss}, we can calculate the respective band structure of the surface layer. We adjust μ_{ss} to reproduce the Fermi wavevector of the experiment as a starting point for μ_{ss}. Then we use a finite-size model with a single adatom as a disturbance. In that model, we adjust μ_{ss} to reproduce the same surface wavelength as in the experiment, using experimental data of a single Ag adatom on Ag(111). This results in $\mu_{\text{ss}} = -5.95\, t_{\text{ss}}$.
To relate t_{ss} to natural units of energy, we calculate the band structure again. In the experiment, a band bottom of -55 meV has been found, which corresponds to the band bottom of $0.05\, t_{\text{ss}}$ in our model. Thus, we can estimate $t_{\text{ss}} = 1.1$ eV and $\mu_{\text{ss}} = -6.545$ eV.
For μ_{ad} we choose a value that is multiple t_{ss} away from μ_{ss}. We find that the specific value of μ_{ad} bears very little difference as long as it is different enough from μ_{ss} to be a disturbance. We choose $\mu_{\text{ss}} = -0.11$ eV.
For the superconducting order parameter, we choose $\Delta_{\text{sc}} = 25$ meV, which is roughly 10 times larger than in the experiment. This is done to account for the limited energy resolution caused by the limited size of the bulk in the tight-binding model, which results in a limited number of eigenvalues. If the gap was not chosen larger than in the experiment, one would need a much larger tight-binding system to resolve the gap. As our system already requires us to solve matrices of roughly 180000×180000 in size, it would not be reasonable to further increase the system size by another order of magnitude. For the SC layer, we choose to use the same values for t and μ as in the surface state layer. Summarizing the above, the full list of parameters is

$$\begin{aligned} t_{\text{sc}} = t_{\text{ss}} = 1.1 \text{ eV}, \quad \mu_{\text{ad}} = -0.11 \text{ eV}, \\ \mu_{\text{sc}} = \mu_{\text{ss}} = -6.545 \text{ eV}, \quad \Delta_{\text{sc}} = 25 \text{ meV}. \end{aligned} \tag{7.11}$$

Discussion of the Results

The energy-dependent DOS evaluated inside of the QD for varying L_x with a fixed $L_y = 30$ sites (≈ 7.5 nm) is shown in Fig. 7.4 (b), where we set the

coupling to the SC layer to zero in order to clearly resolve the QD's eigenmodes. The eigenmodes follow the well-known L_x^{-2} trend through the Fermi energy E_F as a function of the length of the QD. When a small coupling to the SC layer is added (Fig. 7.4 (c)), the eigenmodes acquire particle-hole mixing and show an anticrossing behavior close to E_F. This shows that the QD's eigenmodes acquire superconducting pairing with an induced superconducting gap. Within the 3D tight-binding model, we are additionally able to depict the spatial distribution of the QD's eigenstates. Two examples for the LDOS in QDs of different lengths ($L_x = 25$ sites and $L_x = 40$ sites, corresponding to 6.25 nm and 10.0 nm, respectively) are shown in Fig. 7.4 (d), where the energy is integrated over an energy window centered around the respective eigenenergies of the QD's eigenmodes as indicated above the panels. Here, the eigenmodes of the QD are clearly visible.

It can also be shown that level broadening manifests in the tight-binding model. When the coupling to the SC layer is set to zero $t_\mathrm{sc\text{-}ss} = 0$, the $[n_x, n_y] = [1, 1]$ eigenmode in a corral of 25×30 sites only has a non-zero spectral density at in-gap energies (Fig. 7.4 (b)), but not at energies outside of the gap. Fig. 7.4 (e) shows the integrated LDOS outside of the SC gap integrated from $-2.00\,\Delta_\mathrm{s}$ to $-1.12\,\Delta_\mathrm{s}$ for $t_\mathrm{sc\text{-}ss} = 0$ and $t_\mathrm{sc\text{-}ss} = 0.034\,t_\mathrm{ss}$. For zero coupling, this integrated LDOS is zero inside of the QD, showing that the states are energetically sharp. For non-zero coupling (Fig. 7.4 (e), right panel), this LDOS is non-zero and shows the same shape inside the QD as in the case of integrating over energies close to the eigenenergy (Fig. 7.4 (d), left panel). This shows that the energy of the QD eigenmodes is broadened by the coupling to the superconducting host, which is in agreement with the interpretation of the experimental results that the original eigenmode is broadened by finite coupling to a host (Fig. 7.2 (c) showing the coexistence of sharp MSSs and the broader resonance level outside of the gap).

7.4 Conclusions and Outlook

The experimental observations of MSSs invalidate the idea that an appearance of sharp in-gap states in STM experiments on superconductors must stem from either magnetic impurities [119, 190] or unconventional SC pairing [199, 200]. The sharp linewidth Γ found here can be understood as a consequence of negligible scattering into the gapped bulk states. The energy of MSSs depend on the ratio of Γ and Δ_s. For single-atomic impurities in experiments, this ratio is $\Gamma/\Delta_\mathrm{s} \gg 1$, which causes the bound states to be very close to the coherence peaks of the bulk SC, which makes them hardly detectable. The linewidth of the eigenmodes studied here are of similar magnitude as the SC gap, causing low-energy states to be well split off from the coherence peaks, marking the first experimental confirmation of these spin-degenerate Andreev bound states 50 years after they have been predicted by Machida and Shibata [89]. The strongest coupling is observed for the narrowest QD, when scattering of the walls is maximal, which has previously been speculated [78, 79]. As Γ can be controlled by tuning L_x, the induced gap Δ_ind is tunable as well. The experimentally observed peaks behave like Bogoliubov excitations, carrying a fractional charge which lays the groundwork for potentially studying quasiparticles with fractional charge on the atomic scale. The concept of impurity-supported proximity-induced Cooper pairing could be helpful to induce superconductivity into arbitrary surface states, potentially combined with non-trivial topology, creating a potential pathway to unconventional SCs and Majorana bound states [201]. Building patterns in the surface states of (111) noble-metal surfaces by precise positioning of scattering centers has evolved to one of the most promising platforms in the direction of artificial lattices. These systems have shown to host Dirac fermions [202, 203], flat bands [158, 204, 205], wave-functions in fractal geometries [206] and topological non-trivial states [205, 207]. Our results facilitate studying interactions of these exotic phenomena with SC pairing in a simple and tunable platform. Additionally, it would be interesting to move to a platform with reduced screening, potentially enabling atomic-scale studies of the crossover from spin-degenerate to spinful QDs coupled to superconductors.

Chapter 8

Conclusions and Outlook

In this thesis, we studied various magnetic systems on top of superconductors in one- and two-dimensional systems. Additionally, we provided theoretical support to experiments which discovered precursors of Majorana zero modes in chains on clean superconductors and Machida Shiba states. In the following, we go through these projects individually, highlighting the most important results and providing outlooks for future research.

We numerically determine the magnetic ground states of a tight-binding model for one-dimensional chains with magnetism and proximity-induced s-wave superconductivity, which are typical ingredients for the experimental realization of Majorana zero modes [8]. We do so without any limiting *a priori* assumptions about the magnetic states and find a much richer magnetic phase space than in previous results [24, 25, 27, 28], identifying complex collinear and non-collinear states. Analyzing the topological electronic phases, we find that the model can only host Majorana zero modes self-consistently in the harmonic spiral regime, which is smaller than previously believed for small and medium values of the superconducting order parameter. Additionally, we find that the length of the chain can crucially influence the magnetic ground state due to finite-size effects, potentially determining whether the system hosts Majorana zero modes. This effect is most prominent on chain lengths on the order of tens of atoms, i.e., the chain length typically used in experiments on atomic spin chains on superconductors [3].

Furthermore, we present a new approximative and computationally efficient method to identify the magnetic ground states of tight-binding models by fitting a potentially complex classical spin model. This method is not only orders of magnitudes more efficient than performing the Monte-Carlo simulations di-

rectly in the tight-binding model, but also grants insights into the driving magnetic forces by producing a classical model for the system's magnetism. Using this method, we reproduce the previous results in order to demonstrate its effectiveness and reliability.

We proceed to apply this new method to a two-dimensional square lattice with periodic boundary conditions. We fully characterize the magnetic phase diagram of a 2D model featuring superconductivity, Rashba spin-orbit coupling, magnetism, and an external magnetic field. In doing so, we find a surprisingly rich phase diagram that features 2q-spin-spirals, skyrmions, superpositions of an AFM with a spiral of characteristic angle for RSO coupling, and a 2×2-pattern next to the usual ferromagnetic, checkerboard anti-ferromagnetic, row-wise anti-ferromagnetic, spin-spiral, and anti-ferromagnetic-spin spiral states. Since chiral structures are promising candidates for non-trivial electronic topological states [35, 183–185], it would be interesting to analyze the electronic topological structure of this system in future research.

Our results on the magnetic ground states of one- and two-dimensional systems facilitate experiments on spin-polarized tunneling spectroscopy, since knowledge about the structure of expectable magnetic states helps in identifying magnetic states experimentally. Our new method of identifying the magnetic ground states of tight-binding models allows us to explore the magnetism of highly complex tight-binding models. As long as the complete eigenvalue problem of the tight-binding system can be solved within reasonable computation times, this method can be used to approximate the magnetic ground state, capturing complex magnetic behaviors that might be lost in more limited approximations. The method is especially efficient when only a portion of the system is magnetic. This invites future researchers to apply it to magnetic chains, islands or complex adatom arrays on superconducting substrates, using three-dimensional tight-binding models that resemble actual experimental setups that might potentially host Majorana zero modes.

We create a tight-binding model in support of the first experiment that shows the simultaneous measurement of zero-bias peaks in a hard SC gap on both ends of defect-free chains, marking a major milestone in the quest for Majorana zero modes. With our calculations, we show that the hybridizing

low-energy states are expected to evolve into isolated Majorana zero modes for long chains. We could also identify a critical chain length and show that it is heavily influenced by the precise value of the Rashba spin-orbit coupling, suggesting that enhancing the RSO coupling would lead to further improvements in the localization, reduced interactions of the MMs and an increase in the topological gap Δ_p. There are numerous ways to achieve this experimentally, for example, with a different SC host, heavy-metal interlayers, or synthetic spin-orbit interactions [8, 31, 196, 197], prompting further experiments into this direction.

In support of another experiment that was the first measurement of what we call *Machida-Shibata states* and proof of a 50 years old theoretical prediction of spin-degenerate Andreev bound state by Machida and Shibata [89], we replicate the experimental results in a geometrically correct tight-binding model. Moreover, this is the first time that energetically sharp non-magnetic in-gap states in the gap of an s-wave superconductor have been measured. Within our model, we could show that the quantum dot's eigenmodes acquire superconducting pairing with an induced superconducting gap. The concept of impurity-supported proximity-induced Cooper pairing could be helpful to induce superconductivity into arbitrary surface states, possibly combined with non-trivial topology, creating a potential pathway to unconventional superconductors and Majorana bound states [30, 78, 208, 209].

Bibliography

[1] J. Neuhaus-Steinmetz, E. Y. Vedmedenko, T. Posske, and R. Wiesendanger, Complex magnetic ground states and topological electronic phases of atomic spin chains on superconductors, Phys. Rev. B **105**, 165415 (2022).

[2] J. Neuhaus-Steinmetz, T. Matthies, E. Y. Vedmedenko, T. Posske, and R. Wiesendanger, Large diversity of magnetic phases in two-dimensional magnets with spin-orbit coupling and superconductivity, Phys. Rev. B **110**, 155427 (2024).

[3] L. Schneider, P. Beck, J. Neuhaus-Steinmetz, L. Rózsa, T. Posske, J. Wiebe, and R. Wiesendanger, Precursors of Majorana modes and their length-dependent energy oscillations probed at both ends of atomic Shiba chains, Nat. Nanotechnol. **17**, 384–389 (2022).

[4] L. Schneider, K. T. Ton, I. Ioannidis, J. Neuhaus-Steinmetz, T. Posske, R. Wiesendanger, and J. Wiebe, Proximity superconductivity in atom-by-atom crafted quantum dots, Nature **621**, 60–65 (2023).

[5] A. Y. Kitaev, Unpaired Majorana fermions in quantum wires, Physics-Uspekhi **44**, 131–136 (2001).

[6] A. Kitaev, Fault-tolerant quantum computation by anyons, Annals of Physics **303**, 2–30 (2003).

[7] A. Stern, Non-Abelian states of matter, Nature **464**, 187–193 (2010).

[8] S. Nadj-Perge, I. K. Drozdov, B. A. Bernevig, and A. Yazdani, Proposal for realizing Majorana fermions in chains of magnetic atoms on a superconductor, Phys. Rev. B **88**, 020407(R) (2013).

[9] Y. Oreg, G. Refael, and F. von Oppen, Helical Liquids and Majorana Bound States in Quantum Wires, Phys. Rev. Lett. **105**, 177002 (2010).

[10] R. M. Lutchyn, J. D. Sau, and S. Das Sarma, Majorana Fermions and a Topological Phase Transition in Semiconductor-Superconductor Heterostructures, Phys. Rev. Lett. **105**, 077001 (2010).

[11] A. Kitaev, Periodic table for topological insulators and superconductors, in *AIP Conf. Proc.*, Vol. 1134 (AIP, 2009) pp. 22–30.

[12] S. Ryu, A. P. Schnyder, A. Furusaki, and A. W. Ludwig, Topological insulators and superconductors: Tenfold way and dimensional hierarchy, New J. Phys. **12**, 065010 (2010).

[13] V. Mourik, K. Zuo, S. M. Frolov, S. R. Plissard, E. P. A. M. Bakkers, and L. P. Kouwenhoven, Signatures of Majorana Fermions in Hybrid Superconductor-Semiconductor Nanowire Devices, Science **336**, 1003–1007 (2012).

[14] A. Das, Y. Ronen, Y. Most, Y. Oreg, M. Heiblum, and H. Shtrikman, Zero-bias peaks and splitting in an Al-InAs nanowire topological superconductor as a signature of Majorana fermions, Nat. Phys. **8**, 887–895 (2012).

[15] H. Zhang, C.-X. Liu, S. Gazibegovic, D. Xu, J. A. Logan, G. Wang, N. van Loo, J. D. S. Bommer, M. W. A. de Moor, D. Car, R. L. M. Op het Veld, P. J. van Veldhoven, S. Koelling, M. A. Verheijen, M. Pendharkar, D. J. Pennachio, B. Shojaei, J. S. Lee, C. J. Palmstrøm, E. P. A. M. Bakkers, S. Das Sarma, and L. P. Kouwenhoven, Retraction Note: Quantized Majorana conductance, Nature **591**, E30–E30 (2021).

[16] S. Nadj-Perge, I. K. Drozdov, J. Li, H. Chen, S. Jeon, J. Seo, A. H. MacDonald, B. A. Bernevig, and A. Yazdani, Observation of Majorana fermions in ferromagnetic atomic chains on a superconductor, Science **346**, 602–607 (2014).

[17] H. Kim, A. Palacio-Morales, T. Posske, L. Rózsa, K. Palotás, L. Szunyogh, M. Thorwart, and R. Wiesendanger, Toward tailoring Majorana

bound states in artificially constructed magnetic atom chains on elemental superconductors, Science Advances **4**, eaar5251 (2018).

[18] L. Schneider, S. Brinker, M. Steinbrecher, J. Hermenau, T. Posske, M. dos Santos Dias, S. Lounis, R. Wiesendanger, and J. Wiebe, Controlling in-gap end states by linking nonmagnetic atoms and artificially-constructed spin chains on superconductors, Nat. Commun. **11**, 4707 (2020).

[19] L. Schneider, P. Beck, T. Posske, D. Crawford, E. Mascot, S. Rachel, R. Wiesendanger, and J. Wiebe, Topological Shiba bands in artificial spin chains on superconductors, Nat. Phys. **17**, 943–948 (2021).

[20] J. F. Steiner, C. Mora, K. J. Franke, and F. von Oppen, Quantum Magnetism and Topological Superconductivity in Yu-Shiba-Rusinov Chains, Phys. Rev. Lett. **128**, 036801 (2022).

[21] O. Kashuba, B. Sothmann, P. Burset, and B. Trauzettel, Majorana STM as a perfect detector of odd-frequency superconductivity, Phys. Rev. B **95**, 174516 (2017).

[22] J. Linder and A. V. Balatsky, Odd-frequency superconductivity, Rev. Mod. Phys. **91**, 045005 (2019).

[23] D. Kuzmanovski, R. S. Souto, and A. V. Balatsky, Odd-frequency superconductivity near a magnetic impurity in a conventional superconductor, Phys. Rev. B **101**, 094505 (2020).

[24] J. Klinovaja, P. Stano, A. Yazdani, and D. Loss, Topological Superconductivity and Majorana Fermions in RKKY Systems, Phys. Rev. Lett. **111**, 186805 (2013).

[25] M. M. Vazifeh and M. Franz, Self-Organized Topological State with Majorana Fermions, Phys. Rev. Lett. **111**, 206802 (2013).

[26] A. Heimes, D. Mendler, and P. Kotetes, Interplay of topological phases in magnetic adatom-chains on top of a Rashba superconducting surface, New Journal of Physics **17**, 023051 (2015).

[27] W. Hu, R. T. Scalettar, and R. R. P. Singh, Interplay of magnetic order, pairing, and phase separation in a one-dimensional spin-fermion model, Phys. Rev. B **92**, 115133 (2015).

[28] S. Minami and H. Kawamura, Low-Temperature Magnetic Properties of the Kondo Lattice Model in One Dimension, J. Phys. Soc. Japan **84**, 044702 (2015).

[29] B. Braunecker, P. Simon, and D. Loss, Nuclear Magnetism and Electronic Order in ^{13}C Nanotubes, Phys. Rev. Lett. **102**, 116403 (2009).

[30] B. Braunecker and P. Simon, Interplay between Classical Magnetic Moments and Superconductivity in Quantum One-Dimensional Conductors: Toward a Self-Sustained Topological Majorana Phase, Phys. Rev. Lett. **111**, 147202 (2013).

[31] B. Braunecker, G. I. Japaridze, J. Klinovaja, and D. Loss, Spin-selective Peierls transition in interacting one-dimensional conductors with spin-orbit interaction, Phys. Rev. B **82**, 045127 (2010).

[32] B. Braunecker, P. Simon, and D. Loss, Nuclear magnetism and electron order in interacting one-dimensional conductors, Phys. Rev. B **80**, 165119 (2009).

[33] P. Kurz, G. Bihlmayer, K. Hirai, and S. Blügel, Three-Dimensional Spin Structure on a Two-Dimensional Lattice: Mn/Cu(111), Phys. Rev. Lett. **86**, 1106–1109 (2001).

[34] S. Heinze, K. von Bergmann, M. Menzel, J. Brede, A. Kubetzka, R. Wiesendanger, G. Bihlmayer, and S. Blügel, Spontaneous atomic-scale magnetic skyrmion lattice in two dimensions, Nat. Phys. **7**, 713–718 (2011).

[35] J. Bedow, E. Mascot, T. Posske, G. S. Uhrig, R. Wiesendanger, S. Rachel, and D. K. Morr, Topological superconductivity induced by a triple-q magnetic structure, Phys. Rev. B **102**, 180504(R) (2020).

[36] T. Kurumaji, M. Gen, S. Kitou, K. Ikeuchi, H. Sagayama, H. Nakao, T. R. Yokoo, and T.-h. Arima, Canted antiferromagnetism in a spin-orbit coupled $S_{\text{eff}} = 3/2$ triangular-lattice magnet DyAuGe, Nature Communications **16**, 2176 (2025).

[37] N. Romming, C. Hanneken, M. Menzel, J. E. Bickel, B. Wolter, K. von Bergmann, A. Kubetzka, and R. Wiesendanger, Writing and Deleting Single Magnetic Skyrmions, Science **341**, 636–639 (2013).

[38] Y.-T. Shao, S. Das, Z. Hong, R. Xu, S. Chandrika, F. Gómez-Ortiz, P. García-Fernández, L.-Q. Chen, H. Y. Hwang, J. Junquera, L. W. Martin, R. Ramesh, and D. A. Muller, Emergent chirality in a polar meron to skyrmion phase transition, Nat. Commun. **14**, 1355 (2023).

[39] L. Šmejkal, J. Sinova, and T. Jungwirth, Emerging Research Landscape of Altermagnetism, Phys. Rev. X **12**, 040501 (2022).

[40] A. Fert, V. Cros, and J. Sampaio, Skyrmions on the track, Nat. Nanotechnol. **8**, 152–156 (2013).

[41] P. Grünberg, R. Schreiber, Y. Pang, M. B. Brodsky, and H. Sowers, Layered Magnetic Structures: Evidence for Antiferromagnetic Coupling of Fe Layers across Cr Interlayers, Phys. Rev. Lett. **57**, 2442–2445 (1986).

[42] C. Back, V. Cros, H. Ebert, K. Everschor-Sitte, A. Fert, M. Garst, T. Ma, S. Mankovsky, T. L. Monchesky, M. Mostovoy, N. Nagaosa, S. S. P. Parkin, C. Pfleiderer, N. Reyren, A. Rosch, Y. Taguchi, Y. Tokura, K. von Bergmann, and J. Zang, The 2020 skyrmionics roadmap, J. of Phys. D **53**, 363001 (2020).

[43] E. Y. Vedmedenko, Dynamics of Bound Monopoles in Artificial Spin Ice: How to Store Energy in Dirac Strings, Phys. Rev. Lett. **116**, 077202 (2016).

[44] A. Kitaev, Anyons in an exactly solved model and beyond, Annals of Physics **321**, 2–111 (2006).

[45] B. E. Feldman, M. T. Randeria, J. Li, S. Jeon, Y. Xie, Z. Wang, I. K. Drozdov, B. Andrei Bernevig, and A. Yazdani, High-resolution studies of the Majorana atomic chain platform, Nat. Phys. **13**, 286–291 (2017).

[46] C. Mier, J. Hwang, J. Kim, Y. Bae, F. Nabeshima, Y. Imai, A. Maeda, N. Lorente, A. Heinrich, and D.-J. Choi, Atomic manipulation of in-gap states in the $\beta-Bi_2Pd$ superconductor, Phys. Rev. B **104**, 045406 (2021).

[47] A. Palacio-Morales, E. Mascot, S. Cocklin, H. Kim, S. Rachel, D. K. Morr, and R. Wiesendanger, Atomic-scale interface engineering of Majorana edge modes in a 2D magnet-superconductor hybrid system, Sci. Adv. **5**, eaav6600 (2019).

[48] M. O. Soldini, F. Küster, G. Wagner, S. Das, A. Aldarawsheh, R. Thomale, S. Lounis, S. S. P. Parkin, P. Sessi, and T. Neupert, Two-dimensional Shiba lattices as a possible platform for crystalline topological superconductivity, Nat. Phys. **19**, 1848–1854 (2023).

[49] I. Martin and C. D. Batista, Itinerant Electron-Driven Chiral Magnetic Ordering and Spontaneous Quantum Hall Effect in Triangular Lattice Models, Phys. Rev. Lett. **101**, 156402 (2008).

[50] K. Ido and T. Misawa, Many-body Chern insulator in the Kondo lattice model on a triangular lattice, Phys. Rev. B **109**, 245114 (2024).

[51] Y. Akagi and Y. Motome, Spin Chirality Ordering and Anomalous Hall Effect in the Ferromagnetic Kondo Lattice Model on a Triangular Lattice, J. Phys. Soc. Jpn. **79**, 083711 (2010).

[52] Y. Akagi, M. Udagawa, and Y. Motome, Hidden Multiple-Spin Interactions as an Origin of Spin Scalar Chiral Order in Frustrated Kondo Lattice Models, Phys. Rev. Lett. **108**, 096401 (2012).

[53] R. Wieser, E. Y. Vedmedenko, and R. Wiesendanger, Entropy driven phase transition in itinerant antiferromagnetic monolayers, Phys. Rev. B **77**, 064410 (2008).

[54] M. Kawaguchi, K. Tanabe, K. Yamada, T. Sawa, S. Hasegawa, M. Hayashi, and Y. Nakatani, Determination of the Dzyaloshinskii-Moriya interaction using pattern recognition and machine learning, npj Comput. Mater. **7**, 1–7 (2021).

[55] T. Matthies, A. F. Schäffer, T. Posske, R. Wiesendanger, and E. Y. Vedmedenko, Topological Characterization of Dynamic Chiral Magnetic Textures Using Machine Learning, Phys. Rev. Appl. **17**, 054022 (2022).

[56] F. A. Gómez Albarracín and H. D. Rosales, Machine learning techniques to construct detailed phase diagrams for skyrmion systems, Phys. Rev. B **105**, 214423 (2022).

[57] F. Albarracín, Unsupervised machine learning for the detection of exotic phases in skyrmion phase diagrams (2024), arXiv:2404.10943 .

[58] H. Y. Kwon, H. Yoon, S. Park, D. Lee, D. Shi, Y. Wu, J. Choi, and C. Won, Searching for the ground state of complex spin-ice systems using deep learning techniques, Sci. Rep. **12**, 15026 (2022).

[59] H. Yoon, C. Lee, D. Lee, S. Park, J. Choi, H. Kwon, and C. Won, Interpolation and extrapolation between the magnetic chiral states using autoencoder, Comput. Phys. Commun. **272**, 108244 (2022).

[60] S. Park, H. Yoon, D. Lee, J. Choi, H. Kwon, and C. Won, Optimization of physical quantities in the autoencoder latent space, Sci. Rep. **12**, 1–9 (2022).

[61] N. Käming, A. Dawid, K. Kottmann, M. Lewenstein, K. Sengstock, A. Dauphin, and C. Weitenberg, Unsupervised machine learning of topological phase transitions from experimental data, Mach. Learn. Sci. Tech. **2**, 035037 (2021).

[62] B. S. Rem, N. Käming, M. Tarnowski, L. Asteria, N. Fläschner, C. Becker, K. Sengstock, and C. Weitenberg, Identifying quantum phase transitions using artificial neural networks on experimental data, Nat. Phys. **15**, 917–920 (2019).

[63] T. Chen, S. Kornblith, M. Norouzi, and G. Hinton, A simple framework for contrastive learning of visual representations, in *International Conference on Machine Learning* (PMLR, 2020) pp. 1597–1607.

[64] M. Caron, I. Misra, J. Mairal, P. Goyal, P. Bojanowski, and A. Joulin, Unsupervised Learning of Visual Features by Contrasting Cluster Assignments, in *34th Conference on Neural Information Processing Systems, NeurIPS'20*, Vol. 33 (Curran Associates, Inc., 2020) pp. 9912–9924.

[65] X.-Q. Han, S.-S. Xu, Z. Feng, R.-Q. He, and Z.-Y. Lu, Framework for Contrastive Learning Phases of Matter Based on Visual Representations, Chin. Phys. Lett. **40**, 027501 (2023).

[66] Y. Li, P. Hu, Z. Liu, D. Peng, J. T. Zhou, and X. Peng, Contrastive clustering, in *Proceedings of the AAAI Conference on Artificial Intelligence*, Vol. 35 (2021) pp. 8547–8555.

[67] J. Li, H. Chen, I. K. Drozdov, A. Yazdani, B. A. Bernevig, and A. H. MacDonald, Topological superconductivity induced by ferromagnetic metal chains, Phys. Rev. B **90**, 235433 (2014).

[68] F. Pientka, L. I. Glazman, and F. von Oppen, Topological superconducting phase in helical Shiba chains, Phys. Rev. B **88**, 155420 (2013).

[69] M. Schecter, K. Flensberg, M. H. Christensen, B. M. Andersen, and J. Paaske, Self-organized topological superconductivity in a Yu-Shiba-Rusinov chain, Phys. Rev. B **93**, 140503 (2016).

[70] M. Ruby, F. Pientka, Y. Peng, F. von Oppen, B. W. Heinrich, and K. J. Franke, End States and Subgap Structure in Proximity-Coupled Chains of Magnetic Adatoms, Phys. Rev. Lett. **115**, 197204 (2015).

[71] R. Pawlak, M. Kisiel, J. Klinovaja, T. Meier, S. Kawai, T. Glatzel, D. Loss, and E. Meyer, Probing atomic structure and Majorana wavefunctions in mono-atomic Fe chains on superconducting Pb surface, npj Quantum Information **2**, 16035 (2016).

[72] S. M. Albrecht, A. P. Higginbotham, M. Madsen, F. Kuemmeth, T. S. Jespersen, J. Nygård, P. Krogstrup, and C. M. Marcus, Exponential protection of zero modes in Majorana islands, Nature **531**, 206–209 (2016).

[73] T. D. Stanescu, R. M. Lutchyn, and S. Das Sarma, Dimensional crossover in spin-orbit-coupled semiconductor nanowires with induced superconducting pairing, Phys. Rev. B **87**, 094518 (2013).

[74] E. J. H. Lee, X. Jiang, M. Houzet, R. Aguado, C. M. Lieber, and S. De Franceschi, Spin-resolved Andreev levels and parity crossings in hybrid superconductor-semiconductor nanostructures, Nature Nanotechnology **9**, 79–84 (2014).

[75] P. Yu, J. Chen, M. Gomanko, G. Badawy, E. P. A. M. Bakkers, K. Zuo, V. Mourik, and S. M. Frolov, Non-Majorana states yield nearly quantized conductance in proximatized nanowires, Nature Physics **17**, 482–488 (2021).

[76] P. G. de Gennes, Boundary Effects in Superconductors, Rev. Mod. Phys. **36**, 225–237 (1964).

[77] S. Hikino, S. Takahashi, M. Mori, and S. Maekawa, Proximity effects in a superconductor/ferromagnet junction, Journal of Physics and Chemistry of Solids **69**, 3257–3260 (2008), sNS2007.

[78] A. C. Potter and P. A. Lee, Topological superconductivity and Majorana fermions in metallic surface states, Phys. Rev. B **85**, 094516 (2012).

[79] S. Manna, P. Wei, Y. Xie, K. T. Law, P. A. Lee, and J. S. Moodera, Signature of a pair of Majorana zero modes in superconducting gold surface states, Proceedings of the National Academy of Sciences **117**, 8775–8782 (2020).

[80] T. Tomanic, M. Schackert, W. Wulfhekel, C. Sürgers, and H. v. Löhneysen, Two-band superconductivity of bulk and surface states in Ag thin films on Nb, Phys. Rev. B **94**, 220503 (2016).

[81] M. Chen, Y.-P. Jiang, J. Peng, H. Zhang, C.-Z. Chang, X. Feng, Z. Fu, F. Zheng, P. Zhang, L. Wang, K. He, X.-C. Ma, and Q.-K. Xue, Selective trapping of hexagonally warped topological surface states in a triangular quantum corral, Science Advances **5**, eaaw3988 (2019).

[82] J. Li, W.-D. Schneider, R. Berndt, and S. Crampin, Electron Confinement to Nanoscale Ag Islands on Ag(111): A Quantitative Study, Phys. Rev. Lett. **80**, 3332–3335 (1998).

[83] M. F. Crommie, C. P. Lutz, and D. M. Eigler, Confinement of Electrons to Quantum Corrals on a Metal Surface, Science **262**, 218–220 (1993).

[84] S. E. Freeney, S. T. P. B. andJacob W. Harteveld, and I. Swart, Coupling quantum corrals to form artificial molecules, SciPost Phys. **9**, 085 (2020).

[85] A. Eiguren, B. Hellsing, F. Reinert, G. Nicolay, E. V. Chulkov, V. M. Silkin, S. Hüfner, and P. M. Echenique, Role of Bulk and Surface Phonons in the Decay of Metal Surface States, Phys. Rev. Lett. **88**, 066805 (2002).

[86] S. Heers, P. Mavropoulos, S. Lounis, R. Zeller, and S. Blügel, Lifetime reduction of surface states at Cu, Ag, and Au(111) caused by impurity scattering, Phys. Rev. B **86**, 125444 (2012).

[87] S. E. Freeney, M. R. Slot, T. S. Gardenier, I. Swart, and D. Vanmaekelbergh, Electronic Quantum Materials Simulated with Artificial Model Lattices, ACS Nanoscience Au **2**, 198–224 (2022).

[88] A. A. Khajetoorians, D. Wegner, A. F. Otte, and I. Swart, Creating designer quantum states of matter atom-by-atom, Nature Reviews Physics **1**, 703–715 (2019).

[89] K. Machida and F. Shibata, Bound States Due to Resonance Scattering in Superconductor, Progress of Theoretical Physics **47**, 1817–1823 (1972).

[90] S. De Franceschi, L. Kouwenhoven, C. Schönenberger, and W. Wernsdorfer, Hybrid superconductor-quantum dot devices, Nature Nanotechnology **5**, 703–711 (2010).

[91] F. Bloch, Über die Quantenmechanik der Elektronen in Kristallgittern, Zeitschrift für Physik **52**, 555–600 (1929).

[92] J. C. Slater and G. F. Koster, Simplified LCAO Method for the Periodic Potential Problem, Phys. Rev. **94**, 1498–1524 (1954).

[93] G. H. Wannier, The Structure of Electronic Excitation Levels in Insulating Crystals, Phys. Rev. **52**, 191–197 (1937).

[94] W. P. Lima, F. R. V. Araújo, D. R. da Costa, S. H. R. Sena, and J. M. Pereira, Tight-binding Model in First and Second Quantization for Band Structure Calculations, Brazilian Journal of Physics **52**, 42 (2022).

[95] W. Heisenberg, Zur Theorie des Ferromagnetismus, Zeitschrift für Physik **49**, 619–636 (1928).

[96] M. E. Fisher, Magnetism in One-Dimensional Systems - The Heisenberg Model for Infinite Spin, American Journal of Physics **32**, 343–346 (1964).

[97] K. Millard and H. S. Leff, Infinite-Spin Limit of the Quantum Heisenberg Model, Journal of Mathematical Physics **12**, 1000–1005 (1971).

[98] I. Dzyaloshinsky, A thermodynamic theory of "weak" ferromagnetism of antiferromagnetics, Journal of Physics and Chemistry of Solids **4**, 241–255 (1958).

[99] A. Bogdanov and D. Yablonskiui, Thermodynamically stable "vortices" in magnetically ordered crystals. The mixed state of magnets, Sov. Phys. JETP **68**, 101 (1989).

[100] T. Skyrme, A unified field theory of mesons and baryons, Nuclear Physics **31**, 556–569 (1962).

[101] U. K. Rößler, A. N. Bogdanov, and C. Pfleiderer, Spontaneous skyrmion ground states in magnetic metals, Nature **442**, 797–801 (2006).

[102] S. Mühlbauer, B. Binz, F. Jonietz, C. Pfleiderer, A. Rosch, A. Neubauer, R. Georgii, and P. Böni, Skyrmion Lattice in a Chiral Magnet, Science **323**, 915–919 (2009).

[103] Creative Commons Attribution 3.0 International License, https://creativecommons.org/licenses/by/3.0/.

[104] The Nobel Prize in Physics 1913, NobelPrize.org Nobel Prize Outreach https://www.nobelprize.org/prizes/physics/1913/summary/, accessed: Thu. 13 Mar 2025.

[105] J. Bardeen, L. N. Cooper, and J. R. Schrieffer, Theory of Superconductivity, Phys. Rev. **108**, 1175–1204 (1957).

[106] The Nobel Prize in Physics 1972, NobelPrize.org Nobel Prize Outreach https://www.nobelprize.org/prizes/physics/1972/summary/, accessed: Thu. 13 Mar 2025.

[107] The Nobel Prize in Physics 2003, NobelPrize.org Nobel Prize Outreach https://www.nobelprize.org/prizes/physics/2003/summary/, accessed: Thu. 13 Mar 2025.

[108] C. Tresca, G. Profeta, G. Marini, G. B. Bachelet, A. Sanna, M. Calandra, and L. Boeri, Why mercury is a superconductor, Phys. Rev. B **106**, L180501 (2022).

[109] C. Kallin, Chiral p-wave order in Sr2RuO4, Reports on Progress in Physics **75**, 042501 (2012).

[110] L. Jiao, S. Howard, S. Ran, Z. Wang, J. O. Rodriguez, M. Sigrist, Z. Wang, N. P. Butch, and V. Madhavan, Chiral superconductivity in heavy-fermion metal UTe_2, Nature **579**, 523–527 (2020).

[111] E. F. Talantsev, K. Iida, T. Ohmura, T. Matsumoto, W. P. Crump, N. M. Strickland, S. C. Wimbush, and H. Ikuta, p-wave superconductivity in iron-based superconductors, Scientific Reports **9**, 14245 (2019).

[112] W. Zhu, R. Song, J. Huang, Q.-W. Wang, Y. Cao, R. Zhai, Q. Bian, Z. Shao, H. Jing, L. Zhu, Y. Hou, Y.-H. Gao, S. Li, F. Zheng, P. Zhang, M. Pan, J. Liu, G. Qu, Y. Gu, H. Zhang, Q. Dong, Y. Huang, X. Yuan, J. He, G. Li, T. Qian, G. Chen, S.-C. Li, M. Pan, and Q.-K. Xue, Intrinsic

surface p-wave superconductivity in layered $AuSn_4$, Nature Communications **14**, 7012 (2023).

[113] R. Holm and W. Meissner, Messungen mit Hilfe von flüssigem Helium. XIII, Zeitschrift für Physik **74**, 715–735 (1932).

[114] P. de Gennes and D. Saint-James, Elementary excitations in the vicinity of a normal metal-superconducting metal contact, Physics Letters **4**, 151–152 (1963).

[115] A. F. Andreev, The Thermal Conductivity of the Intermediate State in Superconductors, Zh. Eksperim. i Teor. Fiz. **Vol: 46** (1964).

[116] Y. Luh, Bound state in Superconductors with Paramagnetic Impurities, Acta Physica Sinica **21**, 75–91 (1965).

[117] H. Shiba, Classical Spins in Superconductors, Progress of Theoretical Physics **40**, 435–451 (1968).

[118] A. I. Rusinov, Superconcductivity near a Paramagnetic Impurity, Письма в ЖЭТФ **9**, 146 (1969).

[119] A. V. Balatsky, I. Vekhter, and J.-X. Zhu, Impurity-induced states in conventional and unconventional superconductors, Rev. Mod. Phys. **78**, 373–433 (2006).

[120] C. P. Moca, E. Demler, B. Jankó, and G. Zaránd, Spin-resolved spectra of Shiba multiplets from Mn impurities in MgB_2, Phys. Rev. B **77**, 174516 (2008).

[121] S. Jeon, Y. Xie, J. Li, Z. Wang, B. A. Bernevig, and A. Yazdani, Distinguishing a Majorana zero mode using spin-resolved measurements, Science **358**, 772–776 (2017).

[122] L. Cornils, A. Kamlapure, L. Zhou, S. Pradhan, A. A. Khajetoorians, J. Fransson, J. Wiebe, and R. Wiesendanger, Spin-Resolved Spectroscopy of the Yu-Shiba-Rusinov States of Individual Atoms, Phys. Rev. Lett. **119**, 197002 (2017).

[123] E. I. Rashba and V. I. Sheka, Symmetry of energy bands in crystals of wurtzite type: II. Symmetry of bands including spin-orbit interaction, Fiz. Tverd. Tela 1, 162 (1959).

[124] K. Yaji, A. Harasawa, K. Kuroda, R. Li, B. Yan, F. Komori, and S. Shin, Rashba spin splitting of L-gap surface states on Ag(111) and Cu(111), Phys. Rev. B **98**, 041404 (2018).

[125] M. Hoesch, M. Muntwiler, V. N. Petrov, M. Hengsberger, L. Patthey, M. Shi, M. Falub, T. Greber, and J. Osterwalder, Spin structure of the Shockley surface state on Au(111), Phys. Rev. B **69**, 241401 (2004).

[126] G. Bihlmayer, P. Noël, D. V. Vyalikh, E. V. Chulkov, and A. Manchon, Rashba-like physics in condensed matter, Nature Reviews Physics **4**, 642–659 (2022).

[127] A. Akhmerov, J. Sau, B. van Heck, S. Rubbert, R. Skolasiński, B. Nijholt, I. Muhammad, and T. O. Rosdahl, Topology in condensed matter: tying quantum knots, topocondmat.org `https://topocondmat.org/`, accessed: Mon. 7 April 2025.

[128] D. J. Thouless, M. Kohmoto, M. P. Nightingale, and M. den Nijs, Quantized Hall Conductance in a Two-Dimensional Periodic Potential, Phys. Rev. Lett. **49**, 405–408 (1982).

[129] X.-G. Wen, Topological orders and edge excitations in fractional quantum hall states, in *Field Theory, Topology and Condensed Matter Physics*, edited by H. B. Geyer (Springer Berlin Heidelberg, Berlin, Heidelberg, 1995) pp. 155–176.

[130] B. I. Halperin, Quantized Hall conductance, current-carrying edge states, and the existence of extended states in a two-dimensional disordered potential, Phys. Rev. B **25**, 2185–2190 (1982).

[131] G. E. Volovik, *The Universe in a Helium Droplet* (Oxford University Press, 2009).

[132] A. Altland and M. R. Zirnbauer, Nonstandard symmetry classes in mesoscopic normal-superconducting hybrid structures, Phys. Rev. B **55**, 1142–1161 (1997).

[133] S. shen Chern, Characteristic Classes of Hermitian Manifolds, Annals of Mathematics **47**, 85–121 (1946).

[134] E. Majorana, Teoria simmetrica dell'elettrone e del positrone, Il Nuovo Cimento (1924-1942) **14**, 171–184 (1937).

[135] E. Majorana and L. Maiani, A symmetric theory of electrons and positrons, in *Ettore Majorana Scientific Papers: On occasion of the centenary of his birth*, edited by G. F. Bassani (Springer Berlin Heidelberg, Berlin, Heidelberg, 2006) pp. 201–233.

[136] Y. Nambu, Generalized Hamiltonian Dynamics, Phys. Rev. D **7**, 2405–2412 (1973).

[137] K. Binder and D. Heermann, *Monte Carlo Simulation in Statistical Physics* (Springer, 2002).

[138] E. Y. Vedmedenko, Feature Article: Influence of the lattice discreteness on magnetic ordering in nanostructures and nanoarrays, Phys Status Solidi B Basic Res **244**, 1127–1127 (2007).

[139] A. R. Akhmerov, J. P. Dahlhaus, F. Hassler, M. Wimmer, and C. W. J. Beenakker, Quantized Conductance at the Majorana Phase Transition in a Disordered Superconducting Wire, Phys. Rev. Lett. **106**, 057001 (2011).

[140] G. Binnig and H. Rohrer, Scanning tunneling microscopy, Surface Science **126**, 236–244 (1983).

[141] G. Binnig, H. Rohrer, C. Gerber, and E. Weibel, Surface Studies by Scanning Tunneling Microscopy, Phys. Rev. Lett. **49**, 57–61 (1982).

[142] The Nobel Prize in Physics 1986, NobelPrize.org Nobel Prize Outreach https://www.nobelprize.org/prizes/physics/1986/summary/, accessed: Wed. 5 Mar 2025.

[143] J. Bardeen, Tunnelling from a Many-Particle Point of View, Phys. Rev. Lett. **6**, 57–59 (1961).

[144] J. Tersoff and D. R. Hamann, Theory of the scanning tunneling microscope, Phys. Rev. B **31**, 805–813 (1985).

[145] D. M. Eigler and E. K. Schweizer, Positioning single atoms with a scanning tunnelling microscope, Nature **344**, 524–526 (1990).

[146] J. A. Stroscio and D. M. Eigler, Atomic and Molecular Manipulation with the Scanning Tunneling Microscope, Science **254**, 1319–1326 (1991).

[147] D. M. Eigler, C. P. Lutz, and W. E. Rudge, An atomic switch realized with the scanning tunnelling microscope, Nature **352**, 600–603 (1991).

[148] J. Hermenau, J. Ibañez-Azpiroz, C. Hübner, A. Sonntag, B. Baxevanis, K. T. Ton, M. Steinbrecher, A. A. Khajetoorians, M. dos Santos Dias, S. Blügel, R. Wiesendanger, S. Lounis, and J. Wiebe, A gateway towards non-collinear spin processing using three-atom magnets with strong substrate coupling, Nature Communications **8**, 642 (2017).

[149] D.-J. Choi, C. G. Fernández, E. Herrera, C. Rubio-Verdú, M. M. Ugeda, I. Guillamón, H. Suderow, J. I. Pascual, and N. Lorente, Influence of Magnetic Ordering between Cr Adatoms on the Yu-Shiba-Rusinov States of the $\beta-Bi_2Pd$ Superconductor, Phys. Rev. Lett. **120**, 167001 (2018).

[150] A. Spinelli, M. Gerrits, R. Toskovic, B. Bryant, M. Ternes, and A. F. Otte, Exploring the phase diagram of the two-impurity Kondo problem, Nature Communications **6**, 10046 (2015).

[151] A. A. Khajetoorians, M. Steinbrecher, M. Ternes, M. Bouhassoune, M. dos Santos Dias, S. Lounis, J. Wiebe, and R. Wiesendanger, Tailoring the chiral magnetic interaction between two individual atoms, Nature Communications **7**, 10620 (2016).

[152] S. Loth, S. Baumann, C. P. Lutz, D. M. Eigler, and A. J. Heinrich, Bistability in Atomic-Scale Antiferromagnets, Science **335**, 196–199 (2012).

[153] H. C. Manoharan, C. P. Lutz, and D. M. Eigler, Quantum mirages formed by coherent projection of electronic structure, Nature **403**, 512–515 (2000).

[154] B. Kiraly, E. J. Knol, W. M. J. van Weerdenburg, H. J. Kappen, and A. A. Khajetoorians, An atomic Boltzmann machine capable of self-adaption, Nature Nanotechnology **16**, 414–420 (2021).

[155] N. Nilius, T. M. Wallis, and W. Ho, Development of One-Dimensional Band Structure in Artificial Gold Chains, Science **297**, 1853–1856 (2002).

[156] N. Nilius, T. M. Wallis, and W. Ho, Tailoring electronic properties of atomic chains assembled by STM, Applied Physics A **80**, 951–956 (2005).

[157] C. F. Hirjibehedin, C. P. Lutz, and A. J. Heinrich, Spin Coupling in Engineered Atomic Structures, Science **312**, 1021–1024 (2006).

[158] R. Drost, T. Ojanen, A. Harju, and P. Liljeroth, Topological states in engineered atomic lattices, Nature Physics **13**, 668–671 (2017).

[159] A. Spinelli, B. Bryant, F. Delgado, J. Fernández-Rossier, and A. F. Otte, Imaging of spin waves in atomically designed nanomagnets, Nature Materials **13**, 782–785 (2014).

[160] A. A. Khajetoorians, J. Wiebe, B. Chilian, S. Lounis, S. Blügel, and R. Wiesendanger, Atom-by-atom engineering and magnetometry of tailored nanomagnets, Nature Physics **8**, 497–503 (2012).

[161] A. Kamlapure, L. Cornils, J. Wiebe, and R. Wiesendanger, Engineering the spin couplings in atomically crafted spin chains on an elemental superconductor, Nature Communications **9**, 3253 (2018).

[162] M. Ruby, F. Pientka, Y. Peng, F. von Oppen, B. W. Heinrich, and K. J. Franke, Tunneling Processes into Localized Subgap States in Superconductors, Phys. Rev. Lett. **115**, 087001 (2015).

[163] M. Ternes, W.-D. Schneider, J.-C. Cuevas, C. P. Lutz, C. F. Hirjibehedin, and A. J. Heinrich, Subgap structure in asymmetric superconducting tunnel junctions, Phys. Rev. B **74**, 132501 (2006).

[164] B. Josephson, Possible new effects in superconductive tunnelling, Physics Letters **1**, 251–253 (1962).

[165] P. W. Anderson and J. M. Rowell, Probable Observation of the Josephson Superconducting Tunneling Effect, Phys. Rev. Lett. **10**, 230–232 (1963).

[166] O. Naaman, W. Teizer, and R. C. Dynes, Fluctuation Dominated Josephson Tunneling with a Scanning Tunneling Microscope, Phys. Rev. Lett. **87**, 097004 (2001).

[167] J. G. Rodrigo, H. Suderow, and S. Vieira, On the use of STM superconducting tips at very low temperatures, The European Physical Journal B - Condensed Matter and Complex Systems **40**, 483–488 (2004).

[168] N. Agraït, J. G. Rodrigo, and S. Vieira, Transition from the tunneling regime to point contact and proximity-induced Josephson effect in lead-normal-metal nanojunctions, Phys. Rev. B **46**, 5814–5817 (1992).

[169] O. Naaman and R. Dynes, Subharmonic gap structure in superconducting scanning tunneling microscope junctions, Solid State Communications **129**, 299–303 (2004).

[170] P. Virtanen, R. Gommers, T. E. Oliphant, M. Haberland, T. Reddy, D. Cournapeau, E. Burovski, P. Peterson, W. Weckesser, J. Bright, S. J. van der Walt, M. Brett, J. Wilson, K. J. Millman, N. Mayorov, A. R. J. Nelson, E. Jones, R. Kern, E. Larson, C. J. Carey, İ. Polat, Y. Feng, E. W. Moore, J. VanderPlas, D. Laxalde, J. Perktold, R. Cimrman, I. Henriksen, E. A. Quintero, C. R. Harris, A. M. Archibald, A. H. Ribeiro, F. Pedregosa, P. van Mulbregt, and SciPy 1.0 Contributors, SciPy 1.0: Fundamental Algorithms for Scientific Computing in Python, Nature Methods **17**, 261–272 (2020).

[171] L. M. S. and, Noncollinear magnetism in itinerant-electron systems: Theory and applications, Advances in Physics **47**, 91–160 (1998).

[172] C. W. Groth, M. Wimmer, A. R. Akhmerov, and X. Waintal, Kwant: a software package for quantum transport, New J. Phys. **16**, 063065 (2014).

[173] E. A. Kearsley and J. T. Fong, Linearly independent sets of isotropic Cartesian tensors of ranks up to eight, J. Res. Natl. Bur. Stand., Sect. B **79B**, 49 (1975).

[174] M. dos Santos Dias, S. Brinker, A. Lászlóffy, B. Nyári, S. Blügel, L. Szunyogh, and S. Lounis, Proper and improper chiral magnetic interactions, Phys. Rev. B **103**, L140408 (2021).

[175] L. Van der Maaten and G. Hinton, Visualizing Data using t-SNE, J. Mach. Learn. Res. **9**, 2579–2605 (2008).

[176] Additional material can be found at: `https://timmatthies.github.io/latentspaceexplorer/`.

[177] K. He, X. Zhang, S. Ren, and J. Sun, Deep residual learning for image recognition, in *Proceedings of the IEEE Conference on Computer Vision and Pattern Recognition* (2016) pp. 770–778.

[178] D. P. Kingma and J. Ba, Adam: A method for stochastic optimization (2014), arXiv:1412.6980 .

[179] A. Kukleva, M. Böhle, B. Schiele, H. Kuehne, and C. Rupprecht, Temperature Schedules for self-supervised contrastive methods on long-tail data, in *The Eleventh International Conference on Learning Representations* (2023).

[180] Y. Zhang, B. Kang, B. Hooi, S. Yan, and J. Feng, Deep long-tailed learning: A survey, IEEE Trans. Pattern Anal. Mach. Intell. **45**, 10795–10816 (2023).

[181] B. Berg and M. Lüscher, Definition and Statistical Distributions of a Topological Number in the Lattice O(3) σ-Model, Nuclear Physics B **190**, 412–424 (1981).

[182] X. Z. Yu, Y. Onose, N. Kanazawa, J. H. Park, J. H. Han, Y. Matsui, N. Nagaosa, and Y. Tokura, Real-space observation of a two-dimensional skyrmion crystal, Nature (London) **465**, 901–904 (2010).

[183] Y. Baum, T. Posske, I. C. Fulga, B. Trauzettel, and A. Stern, Gapless topological superconductors: Model Hamiltonian and realization, Phys. Rev. B **92**, 045128 (2015).

[184] A. Kubetzka, J. M. Bürger, R. Wiesendanger, and K. von Bergmann, Towards skyrmion-superconductor hybrid systems, Phys. Rev. Mater. **4**, 081401(R) (2020).

[185] E. Mascot, J. Bedow, M. Graham, S. Rachel, and D. K. Morr, Topological superconductivity in skyrmion lattices, npj Quantum Mater. **6**, 6 (2021).

[186] J. Alicea, Y. Oreg, G. Refael, F. von Oppen, and M. P. A. Fisher, Non-Abelian statistics and topological quantum information processing in 1D wire networks, Nature Physics **7**, 412–417 (2011).

[187] H. Pan, W. S. Cole, J. D. Sau, and S. Das Sarma, Generic quantized zero-bias conductance peaks in superconductor-semiconductor hybrid structures, Phys. Rev. B **101**, 024506 (2020).

[188] J. Chen, B. D. Woods, P. Yu, M. Hocevar, D. Car, S. R. Plissard, E. P. A. M. Bakkers, T. D. Stanescu, and S. M. Frolov, Ubiquitous Non-Majorana Zero-Bias Conductance Peaks in Nanowire Devices, Phys. Rev. Lett. **123**, 107703 (2019).

[189] S. Das Sarma and H. Pan, Disorder-induced zero-bias peaks in Majorana nanowires, Phys. Rev. B **103**, 195158 (2021).

[190] B. W. Heinrich, J. I. Pascual, and K. J. Franke, Single magnetic adsorbates on s-wave superconductors, Progress in Surface Science **93**, 1–19 (2018).

[191] J. Wiebe, A. Wachowiak, F. Meier, D. Haude, T. Foster, M. Morgenstern, and R. Wiesendanger, A 300 mK ultra-high vacuum scanning tunneling microscope for spin-resolved spectroscopy at high energy resolution, Review of Scientific Instruments **75**, 4871–4879 (2004).

[192] Y. A. Bychkov and E. I. Rashba, Oscillatory effects and the magnetic susceptibility of carriers in inversion layers, Journal of Physics C: Solid State Physics **17**, 6039 (1984).

[193] Y. Peng, F. Pientka, L. I. Glazman, and F. von Oppen, Strong Localization of Majorana End States in Chains of Magnetic Adatoms, Phys. Rev. Lett. **114**, 106801 (2015).

[194] P. Beck, L. Schneider, L. Rózsa, K. Palotás, A. Lászlóffy, L. Szunyogh, J. Wiebe, and R. Wiesendanger, Spin-orbit coupling induced splitting of Yu-Shiba-Rusinov states in antiferromagnetic dimers, Nature Communications **12**, 2040 (2021).

[195] J. C. Y. Teo and C. L. Kane, Topological defects and gapless modes in insulators and superconductors, Phys. Rev. B **82**, 115120 (2010).

[196] M. Kjaergaard, K. Wölms, and K. Flensberg, Majorana fermions in superconducting nanowires without spin-orbit coupling, Phys. Rev. B **85**, 020503 (2012).

[197] M. M. Desjardins, L. C. Contamin, M. R. Delbecq, M. C. Dartiailh, L. E. Bruhat, T. Cubaynes, J. J. Viennot, F. Mallet, S. Rohart, A. Thiaville, A. Cottet, and T. Kontos, Synthetic spin-orbit interaction for Majorana devices, Nature Materials **18**, 1060–1064 (2019).

[198] S. Crampin, H. Jensen, J. Kröger, L. Limot, and R. Berndt, Resonator design for use in scanning tunneling spectroscopy studies of surface electron lifetimes, Phys. Rev. B **72**, 035443 (2005).

[199] S. H. Pan, E. W. Hudson, K. M. Lang, H. Eisaki, S. Uchida, and J. C. Davis, Imaging the effects of individual zinc impurity atoms on superconductivity in $Bi_2Sr_2CaCu_2O_{8+\delta}$, Nature **403**, 746–750 (2000).

[200] A. Yazdani, C. M. Howald, C. P. Lutz, A. Kapitulnik, and D. M. Eigler, Impurity-Induced Bound Excitations on the Surface of $Bi_2Sr_2CaCu_2O_8$, Phys. Rev. Lett. **83**, 176–179 (1999).

[201] I. Ioannidis, C.-K. Chiu, and T. Posske, Time-reversal symmetric topological superconductivity in Machida-Shibata lattices (2025), arXiv:2504.08674 [cond-mat.supr-con] .

[202] K. K. Gomes, W. Mar, W. Ko, F. Guinea, and H. C. Manoharan, Designer Dirac fermions and topological phases in molecular graphene, Nature **483**, 306–310 (2012).

[203] T. S. Gardenier, J. J. van den Broeke, J. R. Moes, I. Swart, C. Delerue, M. R. Slot, C. M. Smith, and D. Vanmaekelbergh, p Orbital Flat Band and Dirac Cone in the Electronic Honeycomb Lattice, ACS Nano **14**, 13638–13644 (2020).

[204] M. R. Slot, T. S. Gardenier, P. H. Jacobse, G. C. P. van Miert, S. N. Kempkes, S. J. M. Zevenhuizen, C. M. Smith, D. Vanmaekelbergh, and I. Swart, Experimental realization and characterization of an electronic Lieb lattice, Nature Physics **13**, 672–676 (2017).

[205] S. N. Kempkes, M. R. Slot, J. J. van den Broeke, P. Capiod, W. A. Benalcazar, D. Vanmaekelbergh, D. Bercioux, I. Swart, and C. Morais Smith, Robust zero-energy modes in an electronic higher-order topological insulator, Nature Materials **18**, 1292–1297 (2019).

[206] S. N. Kempkes, M. R. Slot, S. E. Freeney, S. J. M. Zevenhuizen, D. Vanmaekelbergh, I. Swart, and C. M. Smith, Design and characterization of electrons in a fractal geometry, Nature Physics **15**, 127–131 (2019).

[207] S. E. Freeney, J. J. van den Broeke, A. J. J. Harsveld van der Veen, I. Swart, and C. Morais Smith, Edge-Dependent Topology in Kekulé Lattices, Phys. Rev. Lett. **124**, 236404 (2020).

[208] B. Jäck, Y. Xie, J. Li, S. Jeon, B. A. Bernevig, and A. Yazdani, Observation of a Majorana zero mode in a topologically protected edge channel, Science **364**, 1255–1259 (2019).

[209] F. m. c. Crépin, H. Hettmansperger, P. Recher, and B. Trauzettel, Even-odd effects in NSN scattering problems: Application to graphene nanoribbons, Phys. Rev. B **87**, 195440 (2013).

Acknowledgments

I gratefully acknowledge the financial support from the Cluster of Excellence 'Advanced Imaging of Matter' (EXC 2056 - project ID 390715994) of the Deutsche Forschungsgemeinschaft (DFG), from the European Union via the ERC Advanced Grant ADMIRE (project No. 786020), from the Next Generation Partnership program of the UHH: 'Topological spin & superconducting systems', and from my parents.

I want to thank my supervisors Dr. Elena Vedmedenko and Dr. Thore Posske for the guidance and many discussions. I also want to thank Prof. Dr. Roland Wiesendanger for providing the excellent work environment that made this thesis possible.
Of course, I also want to thank all other co-authors of my publications, namely Dr. Lucas Schneider, Dr. Phillip Beck, Dr. Khai Thât-Tôn, Tim Matthies, Ioannis Ioannidis, Dr. Levente Rózsa and Dr. Jens Wiebe. Working with you and providing theoretical support to such amazing experiments has been a great time.
Talking about my colleagues already, I want to thank all my colleagues over the years with special mentions of:

- Dr. Alexander Schäffer for welcoming me into this group so nicely. Going to the opening of a craft beer pub was truly the best lunch break.
- Tim Matthies, for being a great office and climbing buddy.
- Bianca Schulz, for bringing so much life into this group during the last few months of my thesis.
- Dr. Eva Cortés del Rio, for just being a great person. Rock on!

Talking about colleagues that became friends, this gives me a smooth transition to come to my friends from outside of the group. I want to thank all my amazing friends who supported me through these years but especially:

- Torben von der Hoeden, who has always been in my life since the third grade of elementary school. Thanks to the scarifier. (He will get it.)
- Dr. Simon Kothe, for being a great friend and study buddy since literally the first day of university. At some point we still have to publish a paper together.
- Dr. Frederik Bartelmann, for all the fun we had together and being one of the best human beings that I ever met.
- Kim Härtel, for being a great and reliable friend. The weekends in Bremen have always been like mini holidays.
- Neha Malick, for having an open ear for me when I needed someone to talk.
- Merle Schreiber, for all the relaxing sauna evenings.
- my LARP crews - the *Schiffbrüchige* and the *Tawas* - for the holidays for the brain.

I also want to thank the HRA Promovierendenrat for organizing weekly co-writing sessions and two wonderfully productive writing retreats.

I want to thank my parents for supporting me throughout all these years.

I also want to thank Dr. Frederik Bartelmann and Dr. Simon Kothe for proof-reading my thesis.
Last, but the opposite of least, I want to thank my partner Dr. Fiona Dorothea Elisabeth Prodöhl: I love you and I don't know how I would have done this without you.

Eidesstattliche Versicherung

Hiermit erkläre ich an Eides statt, dass ich die vorliegende Dissertationsschrift selbst verfasst und keine anderen als die angegebenen Quellen und Hilfsmittel benutzt habe.

Sofern im Zuge der Erstellung der vorliegenden Dissertationsschrift generative Künstliche Intelligenz (gKI) basierte elektronische Hilfsmittel verwendet wurden, versichere ich, dass meine eigene Leistung im Vordergrund stand und dass eine vollständige Dokumentation aller verwendeten Hilfsmittel gemäß der guten wissenschaftlichen Praxis vorliegt. Ich trage die Verantwortung für eventuell durch die gKI generierte fehlerhafte oder verzerrte Inhalte, fehlerhafte Referenzen, Verstöße gegen das Datenschutz- und Urheberrecht oder Plagiate.

15.08.2025 J. Neuhaus-Steinmetz

Datum Unterschrift des Doktoranden